DOCTORAL SCHOOL
UNIVERSITA' *MEDITERRANEA* DI REGGIO CALABRIA

DIPARTIMENTO DI INGEGNERIA DELL'INFORMAZIONE, DELLE INFRASTRUTTURE E DELL'ENERGIA SOSTENIBILE (DIIES)

PhD IN
INFORMATION ENGINEERING

S.S.D. ING-INF/02
XXXV CICLO

ELECTROMAGNETIC RECOVERY AND SYNTHESIS PROBLEMS IN MRI: NEW APPROACHES TO EPT AND RF-SHIMMING

CANDIDATE
Sabrina ZUMBO

ADVISOR
Prof. Tommaso ISERNIA

CO-ADVISOR
Prof.ssa Martina T. BEVACQUA

COORDINATOR
Prof. Antonio IERA

REGGIO CALABRIA,
23/01/2023

Finito di stampare nel mese di

Edizione 

Quaderno N.
Collana *Quaderni del Dottorato di Ricerca in Ingegneria dell'Informazione*
Curatore *Prof.*

ISBN

Università degli Studi *Mediterranea* di Reggio Calabria
Via dell'Università, 25 (già Salita Melissari) - Reggio Calabria

SABRINA ZUMBO

ELECTROMAGNETIC RECOVERY AND SYNTHESIS PROBLEMS IN MRI: NEW APPROACHES TO EPT AND RF-SHIMMING

The Teaching Staff of the PhD course in
INFORMATION ENGINEERING
consists of:

Antonio Iera(coordinator)
Pier Luigi Antonucci
Giuseppe Araniti
Francesco Buccafurri
Claudia Campolo
Giuseppe Coppola
Mariantonia Cotronei
Lorenzo Crocco
Dominique Dallet
Claudio De Capua
Francesco Della Corte
Giuliana Faggio
Gioia Failla
Fabio Filianoti
Patrizia Frontera
Sofia Giuffrè
Giorgio Graditi
Voicu Groza
Tommaso Isernia
Gianluca Lax
Aime Lay Ekuakille
Gaetano Licitra
Antonella Molinaro
Andrea Morabito
Carlo Francesco Morabito
Giacomo Morabito
Rosario Morello
Fortunato Pezzimenti
Filippo Pratico'
Domenico Rosaci
Giuseppe Ruggeri
Mariateresa Russo
Antonino Vitetta

"I have made missteps along the way. But I have discovered the secret that after climbing a great hill, one only finds that there are many more hills to climb. I have taken a moment here to rest, to steal a view of the glorious vista that surrounds me, to look back on the distance I have come. But I can rest only for a moment, for with freedom comes responsibilities, and I dare not linger, for my long walk is not yet ended."

Nelson Mandela

Acknowledgment

After many years of hard work, the trip is almost over. There have been hard times, which the COVID-19 pandemic has only made worse, but I've made it to the end anyway.

I look back with different eyes now that I'm older and have a few more white hairs. I've put a lot into this journey, but I've also gotten a lot more out of it. Both in terms of knowledge and human, I have to say thank you.

First of all, I would like to thank my advisor Professor Tommaso Isernia, for giving me the chance to work in his brilliant research group, for the help he has given me over the years, and for being able to get me interested in the subject.

A sincere big thank you also goes to my co-advisor Professor Martina Bevacqua, for her help, the time she spent with me, for always being there for me and for how accurate her advice was for the best.

I will always carry with me the cultural (and not only) background they gave me. My work would not have been the same without their help.

My "classmate" and colleague Dr. Giada Battaglia deserves a special thank you. For all the time we spent together, for how helpful and available she was, and, most of all, for all the hours we spent trying to decide which chocolate bar or chips to buy.

I must also thank all of my Lemma lab colleagues, including, Prof. Andrea Morabito, Prof. Roberta Palmeri, and Dr. Vincenzo Violi for their availability and the time we spent together on this journey.

I am also very thankful to Professor Van den Berg for letting me spend my time abroad (even if it was from home) with his group in Utrecht. My deepest gratitude goes to Dr. Stefano Mandija for his patience, availability, and hours spent helping me during this very helpful collaboration.

Finally, a big thank to my boyfriend Vito, who was always there for me and never got tired of hearing me complain when I was feeling down. Thank you for supporting me and helping me escape in the bad times.

Thanks to all my family for being there for me from day one until the end, for their unconditional love and support. I hope I have made you proud of me.

Last but not least, thanks to my second family, my friends, my colleagues and everyone I've met over the three years who has helped make them special.

I owe you all so much, and I can't thank you enough.

Abstract

This Thesis focuses on the development of advanced solutions for electromagnetic recovery and synthesis problems relevant for Magnetic Resonance Imaging (MRI).

Two open issues in MRI are: 1) the exploitation of this imaging modality to theoretically quantify physical, chemical, or physiological property to be useful for different biomedical application, f.i. therapeutic treatments and diagnosis; 2) the necessity to obtain high resolution images, minimizing any kind of artifacts that may appear due to the high field level employed during an MRI scan. As far as the first issue is concerned, a possibility is the use of the radiofrequency (RF) field collected inside the MRI scanner to non-invasively retrieve the in-vivo electrical properties of biological tissues, that is the so-called MRI-based Electrical Properties Tomography. On the other hand, an essential parameter that can improve to enhance the image quality is the homogeneity of the RF field, referred as RF shimming.

Results presented in this Thesis concern new physics-assisted approaches developed for both MRI-EPT and RF shimming. In this respect, we present novel learning-based methodologies for MRI-EPT, and, on the other hand, a new RF shimming procedure that addresses the underlying issue as a field shaping problem. Unlike most of the learning approaches that adopt neural networks as "black-boxes", the proposed learning-based strategies, take into account the physics of the problem provided by the computation of the gradient. As far as the shimming procedure, it is further optimized with the development of an auxiliary model for the convenient selection of the parameter to be employed in the shaping optimization.

Notably, there is a meaningful relation between the two activities. In fact, if the RF field, measured inside an MRI scanner, leads to acquire quantitative information about the model, the knowledge of the model is an essential factor for the shaping strategy to ensure a field which is as homogeneous as possible.

Both proposed methods have several innovations respect to the state of the art and allow computational advantages compared to standard methods usually employed.

Finally, both activities are validated through numerical experiments, tested against 2D simulated human brain phantom.

Contents

List of Figures

List of Tables

1 A general introduction

In this Chapter a general introduction to biomedical imaging is given. Among the numerous imaging systems, the focus is on magnetic resonance imaging and on the main challenges related to this imaging modality: Quantitative imaging and radio frequency (RF) Shimming.

1.1 Biomedical imaging

Biomedical imaging makes it possible the characterization of the intricate structures and dynamic interacting biological processes that are hidden deep inside the human body.

The basic aim in bioimaging technologies is to obtain biological multidimensional information within two (x, y) or three (x, y, z) morphological dimensions. An additional dimension can be the time (t), that can be introduced for a time-related developmental process or event.

Numerous specialized imaging systems utilising various signals, some of them belongs to the so-called electromagnetic spectrum. Many imaging techniques utilize the entire energy spectrum. Magnetic resonance imaging (MRI), X-ray computed tomography (CT), nuclear medicine like Positron Emission Tomography/Computed (PET/CT), ultrasound, and light-based techniques [endoscopy and optical coherence tomography (OCT)] are examples of clinical modalities [1], [2].

The substantial difference between the techniques is the type of signal that characterizes them and so the physics instrumentation which allows the images to be captured. For instance, X-ray for CT, ultrasound for echography, Gamma-ray for nuclear imaging and radiofrequency field for MRI. The radiations can be ionizing and non-ionizing. Ionizing radiation can penetrate the human body and the radiation energy can be absorbed in tissue. This has the potential to cause harmful effects to people, especially at high levels of exposure. The last one is a form of radiation with less energy than ionizing one. Unlike ionizing radiation, non-ionizing radiation does not cause damages to living tissues.

MRI is one of the most considered bioimaging techniques, as it creates accurate images of the body zone under test without the use of ionizing radiation. Indeed, it is possible to determine morphological characteristics of several regions, such as their volume and form, from a structural MRI scan. These measurements can help identify new imaging biomarkers of illnesses and allow for a better understanding of how the organs or tissues change as a result of various circumstances (such as pathological and environmental).

1.2 Magnetic resonance imaging

MRI is an investigation tool used for image acquisition in a medical setting. This imaging modality, unlike X-ray diagnostics, uses non-ionizing radiation that falls within the radio frequency range and is not harmful [2], [3]. In particular, the frequencies used in the resonance machines range from 64 MHz up to about 300MHz.

An MRI scan follows some fundamental steps, which can be schematized as follows. A static magnetic field B_0, produced by a large electromagnet, acts on the nuclei of the hydrogen atoms, which align their magnetic moment parallel to the line of force of the magnet, as happens to the iron filings when it is subjected to a magnet. Subsequently, a radiofrequency (RF) pulse B_1 modifies the orientation of the nuclei which, when the pulse ceases, reorient themselves according to the axis of the magnetic field. By doing so they resonate, that is, they emit a very weak signal called resonance signal. Captured by radio receivers, converted into digital impulses and processed by the computer, it allows to obtain an image whose gray scale corresponds to the different intensities of the resonance signal.

The images obtained through MRI are different from those captured with other imaging methods because they allow us to discriminate between the various tissues on the basis of their biochemical composition, they allow to have an excellent contrast even of the soft tissues, without exposing the patient to ionizing radiation. In addition, an MRI exam can give us three-dimensional images (x, y, z) on three different planes (axial, sagittal and coronal) with very high resolutions in the order of 1 mm. The disadvantages of this type of imaging lie in having very long acquisition times and high susceptibility to

patient motions inside the scanner [2], [3]. Furthermore, the MRI scanner needs complicated instruments that can be affected by noise, increasing costs, and requiring the presence of a very careful stuff. The reader can refer to Chapter 2 for more details.

1.3 Open issues in MRI: Quantitative imaging and RF Shimming

A full diagnosis may be based upon information from several different imaging modalities, which can be correlative or additive in terms of their information content. Radiological imaging uses non- or minimally invasive techniques to identify, track, and treat human disease. The process of acquiring images, identifying abnormalities by the radiologist, and making a diagnosis or treating the patient hasn't much changed in radiology. Despite technological advancements, the introduction of imaging modalities such as MRI and computed tomography (CT), this same paradigm continues to exist [3]. This qualitative imaging-only strategy, meanwhile, leaves a lot of MRI-accessible data on the table; the dimensions and volumes of an imaged object or region, as well as the separation between structures of interest, are the quantitative parameters most frequently employed in clinical practice. Given that, many scientists think that MRI can be optimally exploited without ruling out quantitative analysis, indeed theoretically it can be used to quantify practically any physical, chemical, or physiological attribute. By using the sensitivity of MRI to these tissue properties, it is possible to generate quantitative maps instead of a qualitative one, in which the intensity of each pixel corresponds to a measurement of one specific physical or physiological property. A pursued possibility is to exploit a magnetic resonance system to non-invasively determine the spatial distribution of the electrical properties of the imaged object, named electrical conductivity and dielectric permittivity, in the practice called MRI-based Electrical Properties Tomography (MRI-EPT) [4], [5]. With this practice, one can non-invasively images the conductivity and permittivity maps (simultaneously) in vivo from the radio frequency field signals obtained with MRI and cannot induce additional external energy other than the inherent RF fields.

Engineering has made considerable progress over the past few decades, which have improved the instrumentation used in all medical imaging techniques. The advancements must be directly related to the factors that a clinician considers crucial for a good diagnosis. The three most crucial factors are the spatial resolution, the signal-to-noise ratio (SNR), and the contrast-to-noise ratio (CNR) [2]. When dealing with an MRI system the main challenge is to obtain high resolution images, minimizing any kind of artifacts that may appear. This issue is more evident the more the frequency increases (frequencies $>= 7T$) because the electromagnetic wavelength in tissue is comparable to the dimensions of the imaged object.

An essential parameter that influences the quality and resolution of MRI is the homogeneity of the amplitude of one of the polarizations of the RF Field B_1. Because of the non-homogeneity of the scenario, and of the several constraints at hand, the field usually obtained is far from the one required. This is especially the case for high and ultra-high field scanners ($B_0 > 7T$), which involve a higher frequency of the RF Field [6] .

In this scenario, the issue of levelling (or “shimming") the B_1 field has received considerable importance. There are two macro categories of shimming techniques: passive shimming and active shimming. The first one commonly uses iron pieces or High-permittivity, low-conductivity materials (HPMs) as shims. On the other side, the active shimming uses small coils (or “shim-coils”). However, many shim-coils are necessary to obtain an accurate shimming with an increased magnet cost.

High-permittivity materials placed between RF coils and the subject have been proposed as a method for varying the spatial distribution of the B_1 field, independently of RF shimming or parallel transmission, to improve field homogeneity or enhance SNR in targeted regions. The use of HPMs in combination with RF coils has also been shown to reduce overall required input RF power in transmission and improve coil sensitivity at a variety of field strengths in reception, both in experiments and numerical simulations [6] .

In the active techniques the B_1 inhomogeneity can be addressed by using transmit arrays and applying RF shimming or parallel transmission techniques [7]. These techniques can be optimized to also reduce global Specific

Absorption Rate (SAR), since constructive interferences between the electric fields from multiple transmit coils can result in amplifications of local SAR difficult to predict (see Section 2.7) [8].

1.4 Aim and content of this thesis

The overall aim of the present Doctoral Thesis is to introduce new methodologies for 1) electromagnetic recovery of dielectric permittivity and electrical conductivity values of biological tissues via MRI and 2) shimming of the radiofrequency field inside a MRI scanner.

Notably, the issue of recovering dielectric permittivity and electrical conductivity values (Electrical Properties, EPs) from given electric or magnetic intensities of an electromagnetic field is crucial in a wide range of applications, from civil engineering [9] to biomedical [10]. For example, in electromagnetic dosimetry and hyperthermia treatment planning, it is very important to quantify the induced specific absorption rate by a radiofrequency field. The problem is of course relevant for diagnosis because they are related to healthy state of the tissues, in particular the value of benign tissues compared to tumoral ones are significantly different [11], [12], [13]. Exploiting the MRI scanner's RF field measurement is one of the possible methods for EPT. Exploiting the MRI scanner's RF field measurement is one of the possible methods for EPT. Some of problem-solving strategies are based on the solution of an inverse scattering problem (ISP) [4].

In order to address this issue, it is important to develop proper inversion strategies, able to tackle in a reliable way the underlying ISP. In this respect, the objective of this thesis is to develop novel inversion methods for the characterization of the dielectric properties of tissues via MRI-EPT, based on learning strategies which take advantage of the physical information to solve the ISP. These strategies have been optimized for the quantitative reconstruction of electromagnetic parameters of realistic brain tissues.

On the other hand, the radio frequency shimming is relevant for the quality and resolution of MRI images. In this Thesis, the RF shimming is

addressed as field shaping and antenna array synthesis. This latter warranted attention in fields that were concerned with human health and safety, also in this case hyperthermia treatment planning as well as cellular telecommunications [16], satellite [17], radar applications [18]. Treating the RF shimming as a synthesis problem, and in particular a field shaping problem, is a recent issue. The reason for this choice lies in the common nature of the two problems. In fact, one of the issues of interest in antenna synthesis problems, is the shaping of the field within a given region (named target region). In this case, one needs to develop a shaping strategy which can keep under control the field intensity outside the target region while ensuring some uniformity (or some given shape) of the field intensity into it. This represents one of the objectives to be achieved also in an MRI shimming. Indeed, there is the need to have a shaped field as homogeneous as possible in the areas of interest, while keeping the SAR value limited elsewhere. The starting point for the shimming procedure is the knowledge of the physical model, in terms morphological and electromagnetic properties. Then, the electromagnetic recovery of dielectric permittivity and electrical conductivity values of biological tissues via MRI (described in the first part of the Thesis) is also propaedeutic for MRI shimming (described in the second part of the Thesis).

In this respect, in this thesis a new field shaping strategy is proposed for active RF shimming, which exploits a recent introduced shaping strategies known as multi target- Focusing via Constrained Optimization (mt-FOCO)[23]. Moreover, this procedure has been further optimized through the development and the application of an auxiliary field model for the smart choice of the more useful fields interferences to be exploited in mt-FOCO. The proposed strategy is particularized and assessed for the case of realistic brain tissues.

Needless to say, that the two objectives of this Thesis are closely linked to each other. Indeed, in first activity the basic idea is to use the RF field, that is collected inside the MRI scanner, to recover the morphological characteristics of the tissues (in a quantitative fashion), i.e. the brain model; in the second one, starting from the knowledge of the brain model, as it has been

recovered, the aim is to exploit a shaping procedure to make the RF field as homogeneous as possible (shimming) in order to improve the image's quality and resolution. The more accurate the model, the more accurate the field shimming will be.

The Thesis is composed by 5 Chapters and tree Appendices, where some basics about inverse scattering problem, further aspects of neural networks and more mathematical details about the auxiliary model in Chapter 4 are deepneed.

In Chapter 2, a brief introduction on the principles and physical mechanisms underlying MRI and its applications is provided. MRI is an imaging modality that is considered safer than many other techniques, as X-Ray for example because exploits non-ionizing radiation. It provides excellent soft tissues contrast map and for this reason it very useful for oncological, neurological imaging and so on. During an MRI scan, the patient is placed in a strong magnetic field. Briefly, the principle of MRI is to display the intensity of the emitted RF signal from nuclear spin relaxation in the tissue after a magnetization of the body and the application of RF pulses.

In the First part (Chapter 3), the problem of retrieving the EPs starting from the measurements of the RF field collected inside a MRI scanner is addressed, in the following referred as MRI-EPT. In the Second part of the thesis (Chapter 4) the synthesis procedure for RF Shimming is presented, and the relative auxiliary model for shaping is detailed and applied to the shimming case.

In the first part, the problem underlying EPT is treated as an inverse scattering problem (ISP)[4]. Generally, ISPs can be addressed using either physics-based recovery techniques or learning-based approaches [19]. Due of their iterative nature, the former models mostly used are typically computationally expensive. On the other hand, learning approaches provide a real-time solution, although incorporating domain knowledge is difficult. How to bridge the gap between physics-based approaches and machine-learning-based techniques is an obvious topic for future research by the entire ISP community. In fact, for a variety of engineering and physical issues, researchers

have collected, over the course of several decades, a wealth of domain knowledge that has been utilised to develop approximative direct inversion models and efficient iterative solvers. To avoid employing learning-based approaches as a merely data-driven black-box solver, it is very important to address the issue of successfully integrating them with existing knowledge on underlying physics and classical recovery techniques[4,] [5], [19]. In this respect, in this thesis two different approaches able to address this issue are presented. Unlike most of the learning approaches that lack physical information provided by the forward model, we proposed and teste two physics-assisted learning techniques. Both techniques aim at making the EPs reconstruction process as reliable as possible, alleviating the problem of 'local minima' as well as by reducing the computational time need for all the process. And this makes the procedure useful in clinical application. The first proposed technique exploits the Supervised Descent Method (SDM) [20], [21], the second one instead is based on a cascade of multi-layer CNNs to perform the model update [21]. Both techniques can be seen under the same hat, and the common idea can be summarized as follows: "*given a set of known ground truth contrast maps in terms of electrical properties of tissues and a known starting guess, the iterative procedures (whose architectures are obviously different) are trained to provide as output at each iteration an updated of the unknown tissues map*".

In Chapter 3, after a brief introduction on the already assessed MRI-EPT procedures with a recall of the main principles underlying direct and integral methods, the two model-based learning strategies are presented and described. Then, the proposed procedures are tested in case of 2D realistic scenario mimicking a human head.

In the Second part, the array antenna synthesis problem for RF Shimming is dealt with. In particular, the shimming problem is addressed as a field amplitude shaping, which consists in determining the optimal set of complex excitations of an arbitrary fixed-geometry arrays generating the desired field distribution. A crucial issue to be addressed in this antenna synthesis problems is that one needs to develop a shaping strategy which is able to keep

under control the field intensity outside the target region while ensuring some uniformity (or some given shape) of the field intensity into it.

The ability to enforce a given behavior to the electromagnetic field distribution is one of the most non-trivial tasks, especially in case of complex heterogeneous medium. Many strategies have been presented in literature aimed at shaping a desired field amplitude. In the relevant paper of Woodward and Lawson [22], the far field shaping problem has been tackled by looking for a superposition of many patterns focused in properly chosen given points located in the region of interest (ROI). However, in [22] one cannot enforce any constraints outside the target area and the single focused patterns are simply added in phase without considering any possible phase shifts.

A very recent paradigm is the convex procedure proposed in [23] named multi target - Focusing via Constrained Optimization (mt-FOCO), by the LEMMA laboratory of the Università Mediterranea di Reggio Calabria. In this last procedure the far field shaping problem has been tackled by properly choosing given *control points* located in the ROI and by assuming the phase shifts between the fields at these point as auxiliary unknown variables of the problem.

By taking advantage from mt-FOCO [23], [24], in the second part of the Thesis, a novel synthesis procedure for active radiofrequency shimming is proposed, able to take contemporaneously into account all constraints regarding polarization, homogeneity and strength of the B_1 Field and to enforce SAR limits into the desired treated region. In particular, we proposed a simple auxiliary and physics inspired model [25], which allows a relatively simple physical understanding of convenient and non-convenient fields interferences to be exploited in the shaping problem, and hence a drastic reduction of the computational burden related to its solution via optimization procedure.

In Chapter 4, after a brief introduction of mt-FOCO procedure, the proposed synthesis strategy and the simple auxiliary and physics inspired model for the field intensity shaping are presented and discussed in the case of RF Shimming. Finally, the proposed synthesis procedure is against a realistic head phantom.

Conclusions and recommendation for further developments are finally given in Chapter 5.

2 Magnetic Resonant Imaging principles

In this Chapter, basic principles of MRI image acquisition are presented. The content is mainly based on the book "Introduction to biomedical imaging" by Nadine Barrie Smith and Andrew Webb (2011) [2] , in which more technical details about MRI physics—that are outside the scope of this doctoral thesis—can be found.

2.1 Introduction to biomedical imaging

Among the four major clinical imaging modalities, MRI is the one developed most recently. The first images were acquired in 1973 by Paul Lauterbur, who shared the Nobel Prize for Medicine in 2003 with Peter Mansfield for their shared contribution to the invention and development of MRI. Over 10 million MRI scans were prescribed ever year during the first decade of the 21st century, number of scans that have quadrupled today [26].

MRI provides a spatial map of the hydrogen nuclei (water and lipid) in different tissues. The image intensity depends upon the number of protons in any spatial location, as well as physical properties of the tissue such as viscosity, stiffness and protein content.

The main advantages of MRI are:

- no ionizing radiation is required;
- the images can be acquired in any two- or three-dimensional plane;
- there is excellent soft-tissue contrast;
- a spatial resolution of the order of 1 mm or less can be readily achieved;
- images are produced with negligible penetration effects.

Pathologies in all parts of the body can be diagnosed, with neurological, cardiological, hepatic, nephrological and musculoskeletal applications all being widely used in the clinic. In addition to anatomical information, MRI images

can be made sensitive to blood flow (angiography) and blood perfusion, water diffusion, and localized functional brain activation.

Obviously, the use of a MRI system has also disadvantages, the main are:

- MRI image acquisition is much slower than CT and ultrasound, and is comparable to PET: a typical clinical protocol might last 30–40 minutes with several different types of scans being run, each having a slightly different contrast, with each scan taking between five and ten minutes;
- a significant percentage of patients are precluded from MRI scans due to metallic implants from previous surgeries;
- systems are much more expensive than CT or ultrasound units.

The imaging technology MRI is based on the physical phenomenon of nuclear magnetic resonance (NMR), which was in 1946 discovered by Bloch [27] and Purcell et al. [28]. The phenomenon discovered by Bloch and Purcell describe the interaction between hydrogen nuclei and an external static magnetic field B_0. In particular, there are three essential phases that allow to create a MRI image. The first *magnetization phase*, involves using a static magnetic field B_0 produced by a large magnet; the second stage, *the resonance phase*, involves using a radiofrequency magnetic field B_1 produced by a special coils configuration; in the third and last stage, *the relaxation phase*, the radiofrequency field B_1 is turning off and the signal is acquired.

Then, the MRI system comprises three major hardware components: a superconducting magnet, a set of three magnetic field gradient coils, and a radiofrequency transmitter and receiver. The patient lies on a patient bed which slides into a very strong magnet, typically has a strength of 3 Tesla, approximately 60 000 times greater than the earth's magnetic field [2].

The effect of placing the body in a strong magnetic field is covered in the following sections.

2.2 Effects of a strong magnetic field on protons in the body

To better understand the mechanisms underlying the magnetic resonance method, it is necessary to consider the physical principles on which it is based. It is possible to produce an image only if at the atomic level, each atom is made up of an odd atomic number, because only these types of atoms can be associated the concept of spin on that the magnetic resonance is based. If the nucleus has this spin property, it is able to rotate around its internal axis of rotation.

So that, this charged particle has a given value of angular momentum (P), it also has a magnetic moment (m), and therefore can be thought of as a very small bar magnet with a north and south pole, as shown in Figure 2.1. The phenomenon of quantization is familiar from basic physics and chemistry and means that certain physical parameters can take on only discrete values, rather than having a continuous range. Examples include electric charge, the energy of a photon, and quantum numbers of electrons[2] .

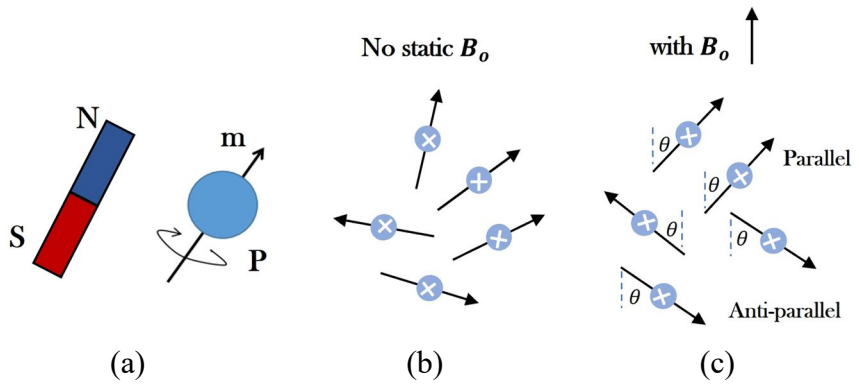

Figure 2.1: The internal rotation of a proton creates a magnetic moment, and so the proton acts as a magnet with north and south pole. (b) Without a magnetic field, the orientations of the magnetic moments are completely random. (c) In presence of a strong magnetic field the magnetic moments must align at an angle $\boldsymbol{\theta \approx 57°}$ with respect to the direction of $\boldsymbol{B_0}$, Zeeman Effect.

Relevant to MRI, the magnitude of the angular momentum of the proton is quantized and has a single, fixed value. The magnitude of the proton's magnetic moment is proportional to the magnitude of the angular momentum:

$$|\underline{m}| = \gamma |\underline{P}| \qquad (2.1)$$

where γ is a constant called the gyromagnetic ratio, which has a value of 267.54 MHz/Tesla for protons.

Not all biological atoms possess the spin property; for instance, oxygen and carbon atoms cannot be used to create an MRI image. Instead, hydrogen, phosphorus, and sodium have this characteristic, making them suitable for use in magnetic resonance imaging. In particular, the water molecules (H2O), which account for 70% of the body mass, are used to capture the hydrogen signal for the MRI scan in the human body. As a result, the hydrogen atom's proton or nucleus plays a key role in producing the signal needed to create an image of the biological tissues [2].

Without the static magnetic field B_0 the net magnetization, i.e. the sum of all the individual magnetic moments in our bodies, is zero because each single spin will have its own orientation (Figure 2.1 (a)). When inside the MRI scanner an external static magnetic field B_0 is applied to the body in the first phase of magnetization, the situation changes. Each magnetic moment, which can be seen as of the magnets with positive and negative poles, tends to follow the orientation of the field, assuming two possible configurations named: parallel and antiparallel configuration, only refer to the z-component of m, generating the so-called Zeeman Effect (see Figure 2.1 (c)).

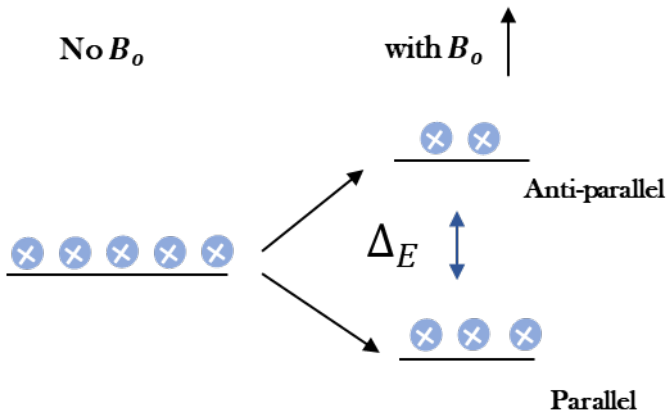

Figure 2.2: The energy difference between the two levels depends upon the value of B_0. More protons stand in the parallel ground energy state than in the higher energy anti-parallel state.

Respect to the energy, these two possible configurations correspond to two different energy levels. In particular, the antiparallel configuration will correspond to an energy level higher than the spins that will assume the parallel configuration. The energy difference between these two levels (see Figure 2.2) will depend on the intensity of the static magnetic field B_0, the Planck constant ($h = 6.63 \cdot 10^{34}\ J\ s$) and the gyromagnetic ratio γ, with the formula:

$$\Delta E = \frac{\gamma h B_o}{2\pi} \qquad (2.2)$$

Furthermore, the number of protons that go in antiparallel configuration is always slightly lower than those oriented in parallel configuration. This is because the antiparallel configuration is the one with the highest energy and therefore the most unstable.

This alignment, however, is never total (see Figure 2.3) and an angle of 54.7°C with respect to the direction of B_0 usually exists. In fact, such kind of interaction consists of a precession of each nuclear magnetic moment around B_0 at an angular frequency ω_0, which is known as the Larmor frequency. If B_0 is applied along the z direction (i.e., the head-feet direction), ω_0 is proportional to the strength of B_0, that is $\omega_0 = \gamma B_0$.

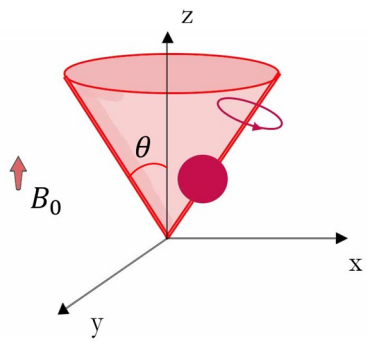

Figure 2.3: A proton in a magnetic field. (a) Using classical mechanics, the torque C acting on the magnetic moment, spinning about an internal axis, causes it to precess about the vertical axis.

This is what happens from the microscopic point of view, considering the single spin. From the macroscopic point of view, it is necessary to introduce

a new quantity called magnetization vector M, given by the sum of all the single magnetic moments:

$$M = \sum_i m_i = M_i i_z \tag{2.3}$$

The net magnetization has only a z-component, since the vector sum of the components on the x- and y axes is zero [2].

2.3 Effects of a radiofrequency pulse on magnetization

After the tissue has been magnetized through the static magnetic field B_0, the second phase of the MRI process occurs. To generate an MRI signal, and therefore an image, it is mandatory to alter the state of equilibrium and rotate the magnetization vector on the x-y plane (Figure 2.4). Therefore, in this phase the balance reached by the spins must change. It is necessary to induce some spins to pass from the parallel configuration, with lower energy, to the antiparallel one, with higher energy. In this regard, an electromagnetic pulse at radiofrequency B_1 is applied perpendicular to the B_0 field which provides the energy necessary for this transition to occur. The introduction of this field produces a torque which causes the net magnetization to rotate towards the x-y plane. The frequency is chosen in such a way as to excite the spin transitions

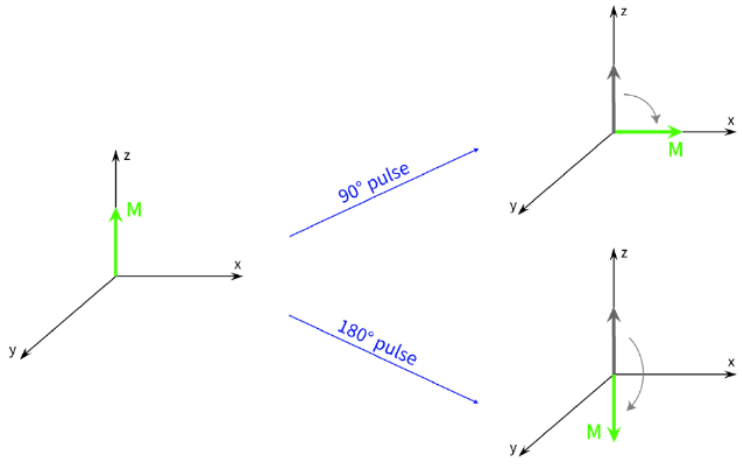

Figure 2.4: Application of an RF pulse about the x-axis rotates the magnetization from the z-direction towards the y-axis. When the RF pulse is switched off, the magnetization precesses around the z-axis at the Larmor frequency.

and misalign their rotation. The B_1 field can exchange the energy of the system

if and only if it has a frequency that is equal to the Larmor frequency (resonance phenomena). The spins are no longer aligned with the B_0 field but rotate changing their position. As a result of B_1, the z component of the magnetization vector decreases in favor of the growing component along x-y. This is also due to the fact that the the nuclei precess coherently because all of the single magnetic moment vectors are pointing in the same direction [2].

The RF signal is very short, in the order of milliseconds. Let B_1 be the pulse width (in Tesla) and t_1 the duration (m-seconds), it is shown that the value of the rotation angle θ known as "tip angle", is given by the relationship:

$$\theta = \gamma B_1 t_1 \tag{2.4}$$

and ranging from 90° to 180°.

Note that if B_1 field is applied along the x-axis, the magnetic moment vector is rotated towards the y-axis and viceversa. Furthermore, if an applied pulse is able to give e 90°C torque ("90° pulse") then the vector lies on the y direction, having the maximum for M_y.

2.4 T1 and T2 relaxation times

When the RF pulse is switched off, the spins tend to return to their equilibrium condition, i.e. they will tend to return to their initial state of alignment along the direction of the B_0 field assumed during the magnetization phase. This rotation generates an electric signal oscillating at the Larmor frequency identified by a pair of conductive loops usually positioned on x-y plane, with an angle of 90°, close to the patient. Detection systems often eliminate these oscillations, leaving only the free induction decay (FID) signal, which decays exponentially to zero.

During the first phase of magnetization, M_z, the z-component, equals M_0, and M_x and M_y, the transverse components, are both equal to zero. Through the addition of energy to the system, the RF pulse produces a non-equilibrium condition after which the system return to thermal equilibrium

when the pulse has been turned off, the last phase of relaxation. While the amplitude of the FID depends essentially on B_0 (which explains why higher field MRI systems are so much desired), the duration depends on two relaxation times: T_1-relaxation affects only z-magnetization, describes the speed at which the z component of the magnetization is recovered after the RF pulse and it is also named spin-lattice relaxation time constant; T_2-relaxation affects only x- and y-magnetization, describes the return to equilibrium of the x and y components of M and is also called spin-spin relaxation time constant.

The MR relaxation can be described mathematically by the following two pair of equations [2]:

$$M_z(t) = M_0 cos\alpha + (M_0 - M_0 \cos\alpha)\left(1 - e^{-\frac{1}{T_1}}\right) \quad (2.5)$$

$$M_y(t) = M_0 \, sin\alpha \, e^{-\frac{t}{T_2}} \quad (2.6)$$

Different tissues have different values of T_1, and anomaly tissues often change T1 relaxation time compared to healthy tissue. These differences can be also enhanced by introducing contrast into the MRI image. Value of T_1 depends on tissues but also on the strength of the magnetic field B_0. The same happens for T_2. There is no direct correlation between these two times, a long T_1 does not necessarily mean a long T_2, but T_1 is always greater than T_2.

Up to now, the mechanism that gives rise to T_2 relaxation assume that all protons precess at exactly the same frequency, but in practice molecular dynamics means that there is a small spread in the precessional frequencies. The inhomogeneities of B_0 that cause a dephasing of the proton magnetic moments in the x-y plane after the pulse. The effects of local B_0 field inhomogeneity is characterized by a relaxation time T_2^+. The combined relaxation time is designated by T_2^*, the value of which is given by:

$$\frac{1}{T_2^*} = \frac{1}{T_2^+} + \frac{1}{T_2} \quad (2.7)$$

This dephasing can be reduced using a particular MRI sequence (i.e., a set of subsequent RF pulses) called Spin Echo sequence, that consists in

applying a 90° pulse, followed by a variable delay τ, a 180° pulse, followed by a variable delay an identical delay τ, and then signal acquisition. The 90° pulse tips the magnetization onto the y-axis, where it decays with a time constant r. The effect of the 180° pulse is to "refocus" the magnetization such that at time r after the 180° pulse, the individual vectors add constructively and the signal reaches a peak [2].

As far as the relation time T_1 is concerned, the value is measured using an inversion recovery sequence, which consists of a 180°pulse, a variable delay τ, and a 90° pulse followed immediately by data acquisition. This sequence is repeated n-times, each time with a different value of the variable delay. The detected signal is:

$$S(\tau_n) = M_0\left(1 - 2e^{-\frac{\tau_n}{T_1}}\right) \tag{2.8}$$

Measuring the value of T_2 requires the use of as pin-echo experiment where e a 90° pulse is applied, followed by a variable delay τ, a 180° pulse, an identical delay τ, and then signal acquisition. Only the effect of pure T_2 relaxation is left. This sequence is repeated n-times, each time with a different value of the variable delay. The detected signal is:

$$S(\tau_n) = M_0 e^{-\frac{2\tau_n}{T_2}} \tag{2.9}$$

Therefore, measuring the relaxation times allows us to characterize each material and discover abnormalities in tissues. For example, in the brain, it is possible to distinguish WM and GM from their different relaxation times. In [29] by applying a magnetic field of 3.0 T (common values are from 1.5 T to 3.0 T), average T_1 values of 1331 and 832 ms from GM and WM and average T_2 of 80 and 110 ms, were obtained respectively. The simple proton density variations between tissues are usually within a few percent. Therefore, the difference in relaxation times is more often employed to reconstruct detailed brain MRI images [29].

2.5 Imaging acquisition

The FID signal introduced in section 2.3 precesses freely after the RF pulse has been turned off. It is detected via electromagnetic induction and decays to a zero-equilibrium value. In this signal there is no spatial information, i.e. there is no way to distinguish between signals coming from protons located at different spatial positions within the body. Hence there is the need to introduce a spatial variation in the magnetic field across a sample, which results in a range of proton resonant frequencies, each dependent upon the position of the particular proton within the body. This is done by incorporating three separate 'gradient coils' in the MRI scanner design. These gradient coils are designed in such a way the spatial variation in magnetic field is linear with respect to spatial location, so that:

$$\frac{\partial B_z}{\partial z} = G_z, \frac{\partial B_z}{\partial x} = G_x, \frac{\partial B_z}{\partial y} = G_y \qquad (2.10)$$

where G represents the gradient measured in T/m.

Then, the magnetic field on the z direction can be rewrite as follow:

$$B_z = B_0 + zG_z \qquad (2.11)$$

and the precession frequencies (ω_z) of the protons,as a function of their position in z, are given by:

$$\omega_z 0 = \gamma B_z = \gamma(B_0 + zG_z) \qquad (2.12)$$

The process of image formation based on the use of gradients to identify the spatial position of a measured MR signal was introduced in 1973 for the first time by Lauterbur. This technique consists of three separate steps named slice selection, phase-encoding and frequency-encoding [2]:

1. **Slice selection:** the choice of the slice orientation is the initial step of an MRI scanning planning. MRI can acquire the image in three different orientations (see figure 2.5): coronal, axial or sagittal images, corresponding to slice-selection in the y-, z-, or x-directions. For example, if the magnetic field gradient G_z is applied along the z direction with a specific frequency $\omega_s \pm \Delta w_s$ such that the Larmor frequency is different in every axial slice, only protons within the axial

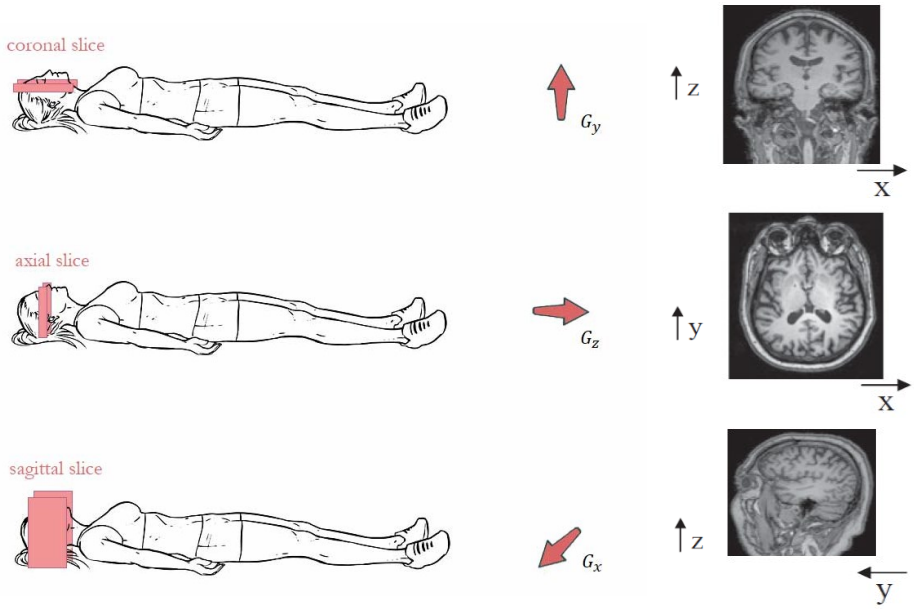

Figure 2.5: Image acquisition. Coronal (top), axial (middle) or sagittal (bottom) slices can be produced by turning on the y, z, or x gradients, respectively, while the RF pulse is being applied [2].

slice (with a precession frequency in that range) are enforced by the RF pulse, and so give a measurable MR signal.

2. **Phase encoding:** chosen the direction of the slice selection, the remaining two directions are identified through phase encoding and frequency encoding. Assuming the z direction, then a gradient G_y is applied along the y direction and the magnetic resonance moments at the same y position rotate with a frequency $\omega_y = \omega_0 + \gamma G_y y$. After an interval t_y , the moments at the same y position shown a spatially dependent phase shift given by $\phi_y = (\omega_0 + \gamma G_y y) \cdot t_y$.
3. **Frequency encoding:** The x-dimension is encoded by applying a frequency-encoding gradient (G_x) while the receiver is gated on and data are being acquired. During this time *t*, protons precess at a frequency given by $\omega_x = \omega_0 + \gamma G_x x$ determined only by their x location.

In order to form a $N \times N$ image, the sequence must be repeated N times, each time with a different value of the phase encoding gradient.

2.6 Imaging characteristics

As mentioned in the introduction to MRI, in all imaging modalities, there are trade-offs between image SNR, spatial resolution and CNR[2] .

1. **Signal to noise ratio:** the SNR is an important quantity used to describe the performance of a MRI system, and is frequently used for image evaluation, measurement of contrast enhancement, pulse sequence and radiofrequency (RF) coil comparison, and quality assurance. Several methods to determine the SNR of MR images have been described. The most commonly used technique is based on the signal statistics in two separate ROIs from a single image: one in the tissue of interest to determine the signal intensity, and one in the image background to measure the noise intensity. The signal is proportional to the net magnetization, M_0, which is directly proportional to the value of B_0. the higher the B_0, the larger the T_1 value and the smaller the image intensity for a given value of T_R.

   The SNR is inversely proportional to the slice thickness, since the number of protons is decreased using a thinner slice. In order to increase the SNR of an image, while maintaining the same spatial resolution, the imaging sequence can be repeated a number of times and the images added together. The MRI signal is coherent, but the noise is incoherent, and so the overall SNR increases by the square-root of the number of images: however, the data acquisition time is lengthened by a factor equal to the number of images.

2. **Spatial resolution:** resolution is the ability of human eyes to distinguish one structure from other. In MRI the resolution is determined by the number of voxels in a specified Field Of View (FOW). The higher the image resolution, the better the small pathologies can be diagnosed. The spatial resolution in the three dimensions for most imaging sequences is simply defined by: (i) the slice thickness, (ii) the field-of-view in the phase-encoded dimension divided by the number of phase-encoding steps, and (iii) the field-of-view in the frequency-encoded dimension divided by the number of acquired data points in that dimension. In this respect, there are two

resolution parameters used in MRI for the production of a 2D image i.e. basic resolution & phase resolution. SNR is inversely proportional to the basic resolution. In other words SNR is directly proportional to the voxel size, increasing the base resolution will reduce the voxel size therefore the SNR of the image will be reduce at the same time increasing the basic resolution will increase the image quality. Increasing the resolution more than the acceptable range will produce noisy or grainy image due to low SNR.

3. **Contrast to Noise Ratio:** Factors which affect the SNR also contribute to the image CNR. Noise sources such as clutter and speckle reduce the image CNR, especially for small pathologies within tissue.

2.7 SAR and safety considerations

Any RF magnetic field has a corresponding RF electrical field that causes currents to flow through conductive tissues. The power deposition in tissue, can be calculated by the local and average specific absorption rate (SAR), expressed in Watts per kilogram. The SAR is a crucial safety factor in MRI. For both local and worldwide regions of interest, there are rigorous regulatory limitations on these values in terms of peak instantaneous and time-averaged values, setting according to the guidelines of the International Commission on Non-Ionizing Radiation Protection (ICNIRP) [30].

The SAR can be calculated in term of electric field E distributions by means of the following formula:

$$SAR = \frac{\sigma\,|E|^2}{2\rho} \tag{2.13}$$

where ρ is the tissue mass density and σ the tissue conductivity [S/m]. The SAR is proportional to the square of the E field multiplied by the time for which the RF field is applied. Therefore, very long sequences can result in considerable power deposition within the patient. However, every commercial MRI scanner has built-in software and hardware to estimate the SAR for each sequence run, and to adjust the imaging parameters in order to remain within regulatory safety limits.

Due to the complex dielectric interaction between the electrical field and the human anatomy, the SAR distribution is typically highly heterogeneous with the occurrences of possible hotspots[31] . SAR hotspots, or amplifications of the electric field, can form at transitions between tissues with a strong dielectric contrast. SAR is directly related to RF-induced heating. The consequences have increased concern about RF safety at high-field (HF), and RF safety is now a significant barrier to the use of high field MRI (HF-MRI) imaging, due to the need for lower flip angles and longer scan periods brought on by lower RF duty cycles, poorer multi-slice efficiency, and diminished contrast [32]. Furthermore, the absence of quantification of local SAR values on a subject-specific Eps imaging, may compromise the underlying improved SNR and image contrast associated with HF-MRI. A correct estimate of local SAR hot spots requires the knowledge of local tissue EPs values at the operating radiofrequency. Conductivity and permittivity distributions play a fundamental and crucial part in the SAR calculation that is performed during HF-MRI. Therefore, real-time and subject-specific EPs imaging is particularly desirable for SAR measurement and for the purpose of constraining tissue heating in the design of HF-MRI pulse sequences [31]. This is because of how important it is to avoid overheating the tissue.

Most studies investigate the possibility to mitigate the deposition of SAR as well as B_1 inhomogeneity [6], [32]. Results in [32], has shown that B_1 shimming (both at 3T and 7T) can be used not only to improve the homogeneity of the RF field, but also to simultaneously push down the SAR levels. A similar procedure is presented in [6] where, the B_1 inhomogeneity is addressed exploiting a convex optimization procedure, also able to ensure limits on SAR. More detailes will be given in the Chapter 4.

3 Physics-assisted learning approaches for MRI-EPT

This Chapter aims at outlining, discussing, and assessing new physics-based learning approaches to retrieve the EPs of a realistic biological scenario. The techniques take advantage of fundamentals results. Differently from the common gradient-based approaches (i.e. CSI-EPT), the proposed techniques can reach the "best" solution in less time, exploiting all the advantages that learning approaches bring with them (i.e. speed, noise robustness and so on). Furthermore, the outcomes of both approaches are tied to the physical nature of the problem, which overcomes the black-box idea commonly used in learning strategies. Numerical examples concerning the two procedures against a realist 2D head phantom are detailed in the Section 3.9 of this Chapter[1].

3.1 Introduction

Electrical conductivity and dielectric permittivity are electromagnetic properties which depend on the tissue structure and composition. Indeed, the electrical properties (EPs) of benign tissue compared to tumors are significantly different [33]. As a consequence, the EPs have the potential to become crucial biomarkers in diagnostic applications, e.g. characterization of brain tumors, pelvic tumors, breast cancer and ischemic stroke [11], [33], [34]. Additionally, the knowledge of the EPs allows for the calculation of the electromagnetic (EM) fields inside tissues and this is very useful in all those medical applications wherein it is crucial to determine the specific absorption rate induced by EM waves, e.g. radio frequency (RF) ablation and hyperthermia for cancer treatment [12], [13].

In order to map the electrical characteristics of tissue in vivo, several different EP mapping methodologies are being investigated [4]. For instance, in electrical impedance tomography (EIT) [35], electrode mounting is used in order to detect currents that have been injected into the sample. Due to the ill-

[1] Some contents of this Chapter have been published in references and [8] [10] [11] [12] [13] [14] of the Publications List of Sabrina Zumbo reported at the end of the Thesis

posed character of the inverse problem, this method has a low spatial resolution. However, it is cost-effective and produces a high resolution of time. In magnetic induced tomography (MIT) [36], an oscillating magnetic field is applied to an object in order to produce eddy currents within the object, and then the perturbed magnetic fields that result from the eddy currents are detected outside of the object. Nevertheless, it is plagued by the identical problems as EIT. MRI is used in magnetic resonance electrical impedance tomography [37] also known as MR-EIT, in order to detect the magnetic field that is created by the probing current. Although this results in a higher spatial resolution, the signal-to-noise ratio is low because there are restrictions placed on the amount of current injection. Hall effect imaging (HEI) [38] is a technique that reconstructs electrophysiological patterns by inducing currents through surface electrodes and detecting the acoustic wave that is emitted. This also has the potential to achieve high resolution images; however, all of the existing injection-based approaches might be susceptible to shielding artefacts caused by non-conductivity tissue. Magneto-acoustic tomography with magnetic induction (MAT-MI) [39] is able to get around the issue of shielding by generating acoustic signals with time-varying magnetic fields, and then detecting those signals using ultrasound measurements. However, techniques that use acoustic measurements are typically restricted to the area of the item that is accessible from the surface.

Another possibility is the Magnetic resonance imaging based electrical properties tomography (MRI-EPT), that is a non-invasive imaging modality that allows to retrieve the spatial distribution of the conductivity and permittivity of living biological tissues exploiting a MRI scanner [4]. This technique can reach a spatial resolution of the order of a few millimeters, does not require electrode mounting, does not induce additional external energy other than the inherent RF fields. Furthermore, the RF fields can easily penetrate into most biological tissue.

The possibility of extracting in MRI-EPT the electrical properties of tissues from measured field maps has been demonstrated in many studies. Firstly, Haacke in 1991 [40], suggested a non-invasive method for extracting the tissue electric characteristics from MRI data. However, the true application

of the method dates to 2003 with a work published by H. Wen [41] in which the EPs are reconstructed using local equations, through the knowledge of the transmitted B_1^+ field. However, such kind of methods have several limitations. First, a second order derivative using finite difference kernels is applied on the measured B_1^+ fields and causes inaccurate boundary reconstructions which make the method sensitive to noise. The B_1^+ mapping can be performed only at the resonance frequency, as a consequence, a dispersion relation to extrapolate information at the frequency of interest is required. In addition, the method requires the knowledge of the absolute transmit phase, which is not directly available, for this reason the so-called "transeive phase assumption" (TPA) is often introduced [42] .

To circumvent the sensitivity to noise of derivative (local) approaches, integral approaches have been proposed [43], [44], [45]. Integral techniques may easily consider heterogeneous electrical property maps, such as tissue boundaries. However, these advantages come at the cost of a higher computing cost. Indeed, these methods involve the solution of a non-linear an ill-posed inverse scattering problem, which represents a non-trivial task [46], [47] and most of them are based on iterative techniques [46], [47]. Indeed, the minimization of the cost function underlying these latter methods is usually achieved by gradient descent method, where the first- or second-order derivatives of the cost function are computed at each iteration. Hence, for high dimensional inverse problems this procedure is significantly time and memory consuming. Moreover, iterative techniques can also suffer from the problem of 'local minima' [48].

To overcome the limits of both local and global methods, a possible solution can be found into the learning-based techniques [19]. In the last years, learning techniques have shown outstanding results on inverse issues, including ill-posed linear (and non-linear) inverse problems, thanks to the rapid progress in the field of artificial intelligence. These techniques aim at making the reconstruction process as reliable as possible, alleviating the problem of 'local minima' as well as by reducing the process elaboration [14]. They are very popular and widely used in several fields including biomedical imaging and diagnosis because they allow to overcome most of the issues related to the

clinical applicability. Indeed, training requires long time, but the inference is rather fast. However, most of learning-based approaches lack physical information from the forward model and require a large amount of training data to achieve accurate results.

Recently, some learning approaches have been proposed to deal with the inverse problem underlying MRI-EPT. The most popular approaches for image processing and reconstruction are based on convolutional neural networks (CNN)[49] For instance, in [50] a feedforward approach employing convolutional neural networks is used demonstrated that deep learning EPT (DL-EPT) is able to reconstruct EPs with a less level of noise respect to direct approaches. Another possible strategy is to consider a hybrid procedure applying DL-EPT to generate good initial guesses for existing ISP inversion models. In [51] a two-step approach is proposed, where Helmholtz-based reconstructions and DL-EPT are used as data-driven initializations for 3D CSI-EPT, which imposes data consistency.

In most previously mentioned approaches the net is considered as a merely "black-box", lacking physical information provided by the forward model. For this reason, researchers in this field try to bridge the gap between learning approaches and the physics of the problem.

In this framework, in this chapter, two different physics-assisted learning methods to face the ISP underlying the MRI-EPT are proposed and compared. The first procedure is based on supervised descent method (SDM) [20], [21] which updates the inverted models using the descent directions collected from the training stage and the physical information provided by forward modelling. The second one is an iterative data-driven procedure based on a cascade of convolutional neural networks (CNNs), wherein each CNN has as input both the current predicted solution and the physical information provided by the gradient calculation to return the next updated solution. Both methods are tested using 2D simulated data of a human head model.

3.2 Direct (local) methods for MRI-EPT

The differential approaches are derived from the local form of Maxwell's equations, by assuming a homogeneous medium and the absence of sources. In the MRI, since the sources generating the EM fields are located outside the body and since the permeability of biological tissue is assumed to be constant and equal to that of vacuum, the Maxwell's equations n be rewrite in frequency domain as [54]

$$-\nabla \times \underline{H}(\underline{r}) + \eta(\underline{r})\underline{E}(\underline{r}) = 0 \tag{3.1}$$

$$\nabla \times \underline{E}(\underline{r}) + \zeta(\underline{r})\underline{H}(\underline{r}) = 0 \tag{3.2}$$

Wherein $\underline{E}$ and $\underline{H}$ are respectively the complex electric and the magnetic field, $\underline{r}$ the location of the field and:

$$\zeta(\underline{r},\omega) = j\omega\mu(\underline{r},\omega) \tag{3.3}$$

$$\eta(\underline{r},\omega) = \sigma(\underline{r},\omega) + j\omega\varepsilon(\underline{r},\omega) \tag{3.4}$$

are respectively the impedance and the per-unit-length admittance of the medium.

By omitting the spatial dependence and applying the divergence to the E-field equation:

$$\nabla \cdot \nabla \times \underline{E} + \zeta \nabla \cdot \underline{H} = 0 \tag{3.5}$$

Then, as the divergence of a curl is equal to zero, by substituting $\underline{E} = \frac{1}{\eta}(\nabla \times \underline{H})$, in the E-field equation, the equation becomes:

$$\frac{1}{\eta}\nabla \times (\nabla \times \underline{H}) + \zeta \underline{H} = 0 \tag{3.6}$$

As $\underline{H}$ is divergence free, the curl can be write as follow:

$$-\frac{1}{\eta}\nabla^2 \underline{H} + \zeta \underline{H} = 0 \tag{3.7}$$

Exploiting the constitutive relations [54] and multiplying both members by $-\frac{\mu\eta\zeta}{\zeta} = \frac{\mu k^2}{\zeta}$, we finally obtain:

$$\nabla^2 \underline{B} + k^2 \underline{B} = 0 \tag{3.8}$$

where $k^2 = \mu\varepsilon\omega^2 - j\mu\sigma\omega$ is related to the object properties, and $\underline{B} = \mu_0 \underline{H}$ the complex magnetic induction.

Taking the inner product of the vector $\boldsymbol{i}^+ = \frac{1}{2}(\boldsymbol{i_x} + \boldsymbol{j i_y})$ and Equation (3.8) gives the Helmholtz equation for the B_1^+ field:

$$\nabla^2 \underline{B_1^+} + k^2 \underline{B_1^+} = 0 \tag{3.9}$$

Assuming B_1^+ is known, then the tissues properties can be derived from the following equation:

$$\frac{\nabla^2 \underline{B_1^+}}{\underline{B_1^+}} = -k^2 \tag{3.10}$$

More in detail, the permittivity and the conductivity will be respectively retrieved by means of [4]

$$\varepsilon = -Re\left\{\frac{\nabla^2 \underline{B_1^+}}{\underline{B_1^+}}\right\}\frac{1}{\mu\omega^2}, \quad e \quad \sigma = Im\left\{\frac{\nabla^2 \underline{B_1^+}}{\underline{B_1^+}}\right\}\frac{1}{\mu\omega} \tag{3.11}$$

These methods have three fundamental limitations: first, the fact of assuming that the medium is homogeneous, but it is well known that this is not the case in an MRI system; second, the presence of second order derivatives, which make the method susceptible to noise; third, these method requires as input the *complex* scattered $B_{1,s}^+$, hence the knowledge of the absolute transmit phase which is not directly available [4].

An alternative to these methods, is the so-called First-order-differentiation inversion [55], but even if this last method has a first order derivate and does not assume homogeneous the medium, it results more complex than the Helmholtz one. Another possibility is represented by the integral methods.

Transeive phase assumption

The complex $B_{1,s}^{+}$ necessitates the measurement of the $B_{1,s}^{+}$ field's magnitude and phase. Exploiting a variety of MRI pulse sequences [42], [56] the magnitude can be assessed. The B_1^+ phase, however, cannot be directly detected with MRI since the superposition of the transmit B_1^+ and receive B_1^- phase is intrinsically measured[42]. The combination of the two is referred to as the transceive phase $\phi^{+/-}$. To extract the B_1^+ phase from the transceive phase, the Transceive Phase Assumption (in the following TPA) is used. This assumption states that the quadrature B_1^+ phase and the reverse quadrature B_1^- phase are equal; consequently, the needed transmit phase is obtained by dividing the MRI measured transceive phase by a factor of two. The transceive phase consists of:

$$\phi^{+/-} = \phi^{+} + \phi^{-} \tag{3.12}$$

Then, the complex field can be rewritten as:

$$B_1^+ = |B_1^+|e^{\phi^+} = |B_1^+|e^{j\phi^{+/-}}\, e^{-j\phi^+} \tag{3.13}$$

3.3 Integral (global) Methods for MRI-EPT

The integral methods are based on the solution of an inverse scattering problem. From the scattering formalism in 2D scalar problem, as detailed in Appendix A, the scattered *E-field* can be written as function of the contrast source W, as follows:

$$E_s = k_b^2 \int_{r' \in D} G(\underline{r}, \underline{r}', \omega)\, \chi(\underline{r}, \omega) E_{tot}(\underline{r}')dV \tag{3.14}$$

In this equation χ is the contrast function which encodes the tissues properties. The total *E-field* can be written as the superposition of the background field (i.e. the incident field $E_{inc}(\underline{r})$ measured in absence of the scattered object) plus the scattered field (Eq. 3.21):

$$E_{tot}(\underline{r},\omega) = E_{inc}(\underline{r}) + k_b^2 \int_{\underline{r}'\in D} G(\underline{r},\underline{r}')W(\underline{r}',\omega)\, dV \quad (3.15)$$

As far as the magnetic field is concerned, the scattered *B-field* can be derived starting from the Maxwell's equations, by considering a coil setup along the z axis and an electric current being run through the coil along this axis, that is [4] [57] :

$$\begin{pmatrix} H_x^s \\ H_y^s \end{pmatrix} + -\frac{1}{\zeta_b}\begin{pmatrix} \partial_y \\ -\partial_x \end{pmatrix} E_s = -\begin{pmatrix} K_x^{ext} \\ K_y^{ext} \end{pmatrix} \quad (3.16)$$

Wherein, ζ_b is the impedance of the background medium and K_{ext} is the external magnetic current flowing through the resonance coil.

In absence of external magnetic sources, the equation becomes:

$$\begin{pmatrix} H_x^s \\ H_y^s \end{pmatrix} = -\frac{1}{\zeta_b}\begin{pmatrix} \partial_y \\ -\partial_x \end{pmatrix} E_s \quad (3.17)$$

Knowing that the measured field in an MRI scanner is usually denoted as B_1 and is a circular polarized field with the following form:

$$B_{1,s}^{+} = \frac{\mu_b}{2}(H_x^s(\underline{r}) + jH_y^s(\underline{r}) \quad (3.18)$$

By substituting in Eq. 3.18 the Eq. 3.17 and 3.14, the integral equation for the scattered magnetic field is given by:

$$B_{1,s}^{+} = -\frac{\mu_b k_b^2}{2\zeta_b}(\partial_y - j\partial_x)\int_{\underline{r}'\in\Sigma} G(\underline{r},\underline{r}')W(\underline{r}',\omega)\, dV \quad (3.19)$$

The domain Σ is the domain in which the field is measured and in this particular case is equal to the contrast domain $\mathcal{D}$.

Eq. 3.14 and Eq. 3.19 define a problem that falls into the category of inverse scattering problems that are difficult to solve because for definition they are ill-posed and non-linear, as both the contrast source w and the contrast function χ are unknowns of the problem[46] [47] , [48]

From a mathematical point of view, starting from the Eq. 3.15 for the total *E-field ,* multiplying both members by the contrast χ the *state equation* can be written in a compact fashion through the contrast function W as follows:

$$W(\underline{r},\omega) = \chi(\underline{r})E_{,inc}(\underline{r}) + \chi(\underline{r})G_D\{\mathrm{W}(\underline{r'},\omega)\},\ \ \underline{r} \in D \quad (3.20)$$

where $G_D\{\cdot\}$ is the Green function operator (or object operator), and can be expressed by the following equation:

$$G_D \equiv k^2 \int_{\underline{r}'\in D} G(\underline{r},\underline{r}')W(\underline{r}',\omega)\, dV \quad (3.21)$$

The same can be done for the *data equation*, that can be written as:

$$B_{1,s}^{+}(\underline{r}) = G_S\{W(\underline{r}',\omega)\}, \qquad \underline{r} \in \Sigma \quad (3.22)$$

Where the operator is:

$$G_S \equiv -\frac{\mu_b k_b^2}{2\zeta_b}(\partial_y - j\partial_x)\int_{\underline{r}'\in\Sigma} G(\underline{r},\underline{r}')W(\underline{r}',\omega)\, dV \quad (3.23)$$

Generally, such kind of methods search the global minimum of a suitable functional which defines the discrepancy between the measured data and the predicted scattered field, that is:

$$\psi(\chi) = \left\| B_{1,s}^{+} - S(\chi, E_{inc}) \right\|^2 \quad (3.24)$$

wherein S is the nonlinear inverse scattering operator. Gradient-based deterministic approaches are commonly used (such as steepest descent, conjugate gradient, Gauss–Newton methods [4]), to iteratively minimize the objective function in. In particular, in every iteration, the update contrast process is performed according to:

$$\chi_{k+1} = \chi_k + \alpha_k \nabla_k \quad (3.25)$$

where k and $k+1$ denote the k[th] and the $(k+1)^{th}$ iteration, respectively, ∇_k is the descent direction of the iterative procedure and α_k is a scalar factor to be evaluated at each iteration that guarantees the maximum decrease of the functional along the considered direction. A critical disadvantage of these local methods is that they may cause the optimization to become trapped in local minima[48] Moreover, they involve the computation

at each iterative of the descent direction, which is both time and memory consuming.

One of the most used iterative methods is the Contrast Source Inversion (CSI) method. More details about this procedure will be given in the following section.

3.4 MRI-EPT via Contrast Sorce Inversion

Contrast source inversion (CSI)-EPT is a reconstruction technique that uses a global integral approach rather than a local differential approach to get beyond the assumption of locally homogenous media. Because the integrals have a smoothing effect, the approach is more consistent close to tissue boundaries and is less noise-sensitive as a result [43], [44], [45].

From a mathematical point of view, recalling results presented in the previous Section, EPs mapping via MRI data can be described, in a compact fashion, by the pair of equations 3.20 and 3.22.

Starting from this assumption, let us define relative residual r of the *state equation* as:

$$r(w,\chi) = \chi E_{inc} - W + \chi G_D\{W\} \tag{3.26}$$

The same can be done for the *data equation*, where if W approximates the contrast source, then the residual will be:

$$\rho(w,\chi) = B_{1,s}^{+}(\underline{r}) - G_S\{W\} \tag{3.27}$$

the $B_{1,s}^{+}$ is the scattered field obtained via measurements and $G_S\{W\}$ is the estimated modeled data. In practice, $B_{1,s}^{+}$ is obtained by subtracting the background field from the total B_1^{+} field.

To solve this set of nonlinear equations, the CSI method o minimise the following cost functional F uses an algorithm based on gradient descent.

$$F(w,\chi) = \frac{||r||^2}{||\chi E_{inc}||^2} + \frac{\left||\rho|\right|^2}{||B_{1,s}^{+}||^2} \tag{3.28}$$

Briefly, let w_{n-1} and χ_{n-1} be the known initial guess, then the CSI procedure updates the contrast source by the Eq. 3.29 as follow:

$$W_n = W_{n-1} + \alpha_n \nabla \mathrm{W}_n \tag{3.29}$$

Where α_n is the step length and $\nabla \mathrm{W}_n$ is the descent direction, the gradient which has to be computed at each iteration.

Like other EPT reconstruction methods[42] [58] , also CSI-EPT requires as input the *complex* scattered $B_{1,s}^{+}$ and the incident electric and magnetic fields, i.e. the RF fields of the transmit coil when there is no load inside, i.e., when the transmit coil is empty (see Section 3.3).

Substituting the Eq. 3.13 in 3.28 we can obtain the new cost functional to minimize in CSI-EPT routine.

3.5 Learning-based techniques for ISP

Nowadays, learning-based methods are becoming an increasingly important tool for solving inverse problems because they allow to speed up the iterative procedure [19] . According to paper [19], all these methods can be enclosed in three macro categories:

1. *Direct Learning Approach:* These methods, also known as *Single Feedforward Approaches*, essentially work as a "black box" [50], [51]. The CNNs are directly applied to retrieve the unknown parameters.
2. *Learning-Assisted Objective-Function Approach:* These methods can be seen as a good trade-off between the *objective-function*[2] and *learning-based* approaches [51], [52]. Indeed, the traditional objective function approach is used to solves ISPs but neural networks are introduced to learn some parameters of the iterative procedure. *The supervised descent method (SDM)* is an example. Another example is the two step

[2] The *objective-function* approaches, also known as *model-based* approaches, fully exploit the forward model *f* and recovers an estimate of *x* from *y* by solving a minimization problem; the *learning-based* approaches also known as data-driven approach, solves inverse problems by processing large datasets, without considering the forward model

approaches proposed in [51] wherein the retrieved EPs map, in output from a black-box CNN, is fed to a CSI algorithm in order to impose data consistency.

3. *Physics-Assisted Learning Approach:* The third category of approaches uses neural networks to solve inverse problem by incorporating domain physical knowledge and its mathematical formulation as input or in the net internal architecture. The most used is the U-net architecture [59] [60] [61].

Beyond the aforementioned classification, in recent years various techniques for solving ISPs have been proposed, each of which is characterized by a specific network architecture. To mention a few, multilayer perceptron (MLP), convolutional neural network (CNN), recurrent neural network (RNN), generative adversarial network (GAN), long-short term memory network (LSTM) and many other variants [60], [61].

The most popular for image processing and reconstruction are CNN or in less measure the MLP. While they are the most common, these network architectures are not the only ones. In fact, the recursive process underlying the integral methods can be emulated through particular (RNN). In [62] , a "Recurrent Inference Machines" (RIM) model is proposed, in which an inverse transformation is learned by means a recurrent networks. When the architecture of a neural network is defined, be it a CNN or an RNN or whatever, it does not possess any kind of knowledge. Any procedure based on neural networks consists of two separated phases: *training phase* and *testing phase*. Training a neural network means finding the best configuration of weights that maximize the accuracy of the learning model. Once the best training solution is found, then the trained network is tested on unseen input data that was not directly included in the training data to check if the network has actually learned its task. Another possible classification can be made taking into account the type of approach used to train the neural network. The two main approaches are [61].

- *Supervised training:* The idea is to produce a dataset composed by the ground truth images X and the corresponding measurements Y, which

can be achieved by simulating the forward solver on data. Thus, it is possible to train a network to learn an inverse mapping, i.e., a network which exploits the measurements Y as input to reconstruct the image X. However, they are susceptible to changes in or uncertainty surrounding the forward operator. Such supervised algorithms often yield excellent results.

- *Unsupervised training:* unlike the previous case, here there is no dataset with a correspondence between X and Y. During the learning phase, an unsupervised network tries to mimic the data it's given and uses the error in its mimicked output to correct itself (i.e. correct its weights & biases). Without the need for human intervention, these algorithms reveal hidden patterns or data clusters. It is ideal for exploratory data analysis, cross-selling strategies, consumer segmentation, and picture identification due to its capacity to identify similarities and differences in information but they are more computational expensive, requiring a large dataset for training and long time to converge. Conversely supervised approaches, require initial human interaction to accurately classify the data. However, these labelled datasets enable supervised algorithms to avoid computational complexity since they do not require a huge training set to generate the desired results, and the results are much more reliable.

The machine learning process uses different data sets in creating algorithms. Training data is the dataset used to train the model. It teaches an algorithm to extract relevant aspects of the outcome. Frequently, this is the first dataset used to teach an algorithm how to employ various attributes, aspects, and technological advancements to get the desired result.

In the following the performance of two physics-assisted learning methods are proposed and compared. The common idea behind the proposed approaches (see paragraphs 3.6 and 3.7) is the following:

"Given a set of known ground truth EPs maps and a known starting guess, the iterative procedure is trained to provide at each iteration as output an updated unknown χ_{k+1} *in such a way to minimize the distance from the initial updated guess and the known ground truth EPs maps"*. In summary, the training procedure can be schematized as in Figure 3.1.

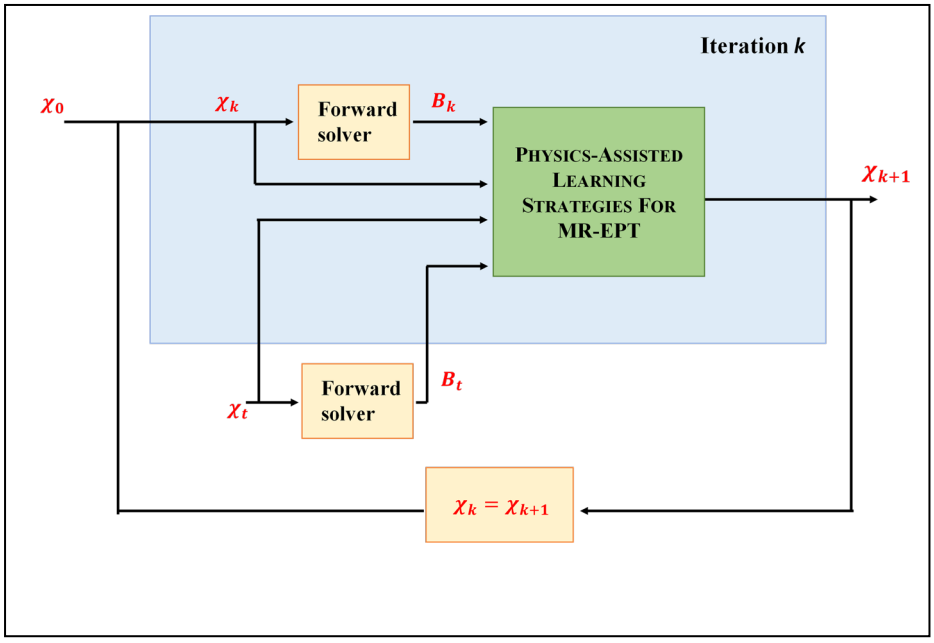

Figure 3.1: Block scheme reporting the basic idea underlying the proposed physics-assisted learning procedures.

The former is based on SDM. it learns the descent directions of the cost function in an offline training process from a variety of samples and then applies these latter to on-line update the reconstructed solution. On the other hand, the latter method involves at each iteration a CNN which updates the reconstructed solution and whose inputs are the current predicted solution and the physical information provided by the gradient direction. Note that, unlike most of the learning techniques proposed in literature, the above learning strategies take into account the physics of the problem in order to improve the generalization ability of the estimation procedure. Both procedures can also be classified as supervised procedures.

3.6 MRI-EPT via Supervised Descent Method

In this section the learning approach based on the supervised descent, to retrieve the EPs of the biological tissues from simulated MRI data, introduced and described. The approach is able to circumvent the computation of the descent directions by learning during an offline procedure a common descent direction by different training models. Then, the learning strategy updates (online) the inverted models by using the descent directions learned both from the training phase and the physical information provided by forward model [51], [53].

More in details, in SDM based MR-EPT, the inputs of the training procedure are X_t, which is a N-row matrix containing the N training models (i.e. the ground truth EPs maps), and B_t, which is the N-row matrix containing the corresponding simulated data. The common descent direction D_k is obtained by minimizing the following cost functional at each iteration [51], [53]:

$$\|\Delta X_k - \Delta B_k D_k\|_F^2 \tag{3.30}$$

wherein $\|\cdot\|_F^2$ denotes the Frobenius norm, and

$$\Delta X_k = X_t - X_k \tag{3.31}$$

$$\Delta B_k = B_k - B_t \tag{3.32}$$

X_t is a N-row matrix containing N ground truth EPs maps, and B_t, is the corresponding simulated complex data matrix. X_k and B_k are the N-row matrices whose elements are respectively the EPs maps retrieved at the kth iteration and the corresponding simulated magnetic field data. Note that, in order to address the ill-posedness of the problem at hand, a Tikhonov regularization is considered wherein the regularization parameter is chosen as the maximum singular value of the matrix ΔB_k. Then, the descent direction D_k can be compute with the following:

$$D_k = V_k \left(\Lambda^2 + \alpha^2 \mathrm{I}\right)^{-1} \Lambda_k^T U_k^T \Delta X_k \tag{3.33}$$

Where $\Delta B_k = U_k^T \Lambda_k^T V_k^T$ and α is damping factor applied to increase the stability of the solving procedure.

Once, the common descent direction is computed, the EPs maps at the $(k+1)^{th}$ iteration are upda ted by means the following equation:

$$X_{k+1} = X_k + \Delta B_k D_k \tag{3.34}$$

The training process stops when both model and data misfit is lower than 10^{-3} [51] [53]

After the training stage, a set of matrices $D_{1,} \ldots, D_n$, where *n* is the number of iterations, are saved for online imaging. They can be considered as known descent directions. In the prediction stage, the updating process of the unknown parameters can be done according to Eq. 3.34.

The initial guess X_0 , should be the same in the training and testing phases. The online process stops when the data misfit is lower than a threshold, set equal to 10^{-3}.

In summary, the main steps involved in the training procedure are reported in Figure 3.2. Note that, in the online prediction stage, the set of D_k are used at each iteration for updating the model through evaluation (Eq. 3.34). It is important to note that this second stage involves all the above steps, except for step 3, which is the most time and memory consuming.

Furthermore, since there is no information on the contrast profiles in the testing phase, the stopping rule will obviously only relate to the data misfit.

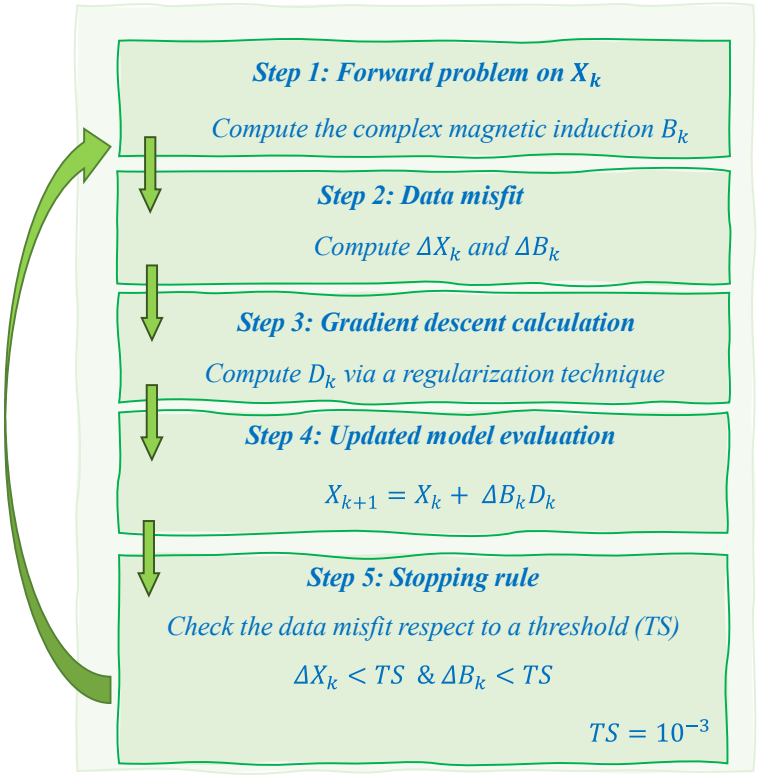

Figure 3.2: Main steps involved for the training of the SDM procedure.

The considered training dataset and the obtained results will be present in the Section 3.8.

3.7 Unrolled optimization via physics-assisted CNN for MRI-EPT

In this paragraph a novel physics-assisted DL method to solve the inverse scattering problem underlying the EPT (starting from data acquired by a MRI scanner) is presented and discussed. We will refer later as 3,CNNs-EPT.

As the standard gradient-based methods, the proposed 3,CNNs-EPT computes at each iteration k the gradient descent direction ∇_k, and then updates the contrast profile by using a CNN (see Figure 3.3(a)).

The gradient descent direction can be defined as:

$$\nabla_k = \frac{E_{z,k}^{*} G_s^{+}\left[G_s\left[E_{z,k}\chi_k\right] - \left(B_1^{+} - B_{1,inc}^{+}\right)\right]}{\left\|B_1^{+} - B_{1,inc}^{+}\right\|^2} \tag{3.35}$$

Wherein $(\cdot)^*$ denotes the conjugate operator, $(\cdot)^+$denotes the adjoint operator, $E_{z,k}$ is the total electric field, B_1^+ is the total magnetic field (i.e. in the training stage, the field simulated in a two-dimensional forward simulation, starting from the knowledge of the ground truth, χ_{true}), G_s is the magnetic radiation operator, defined as in section 3.2-3.3.

From a mathematical point of view, rather than using the Eq. (3.34) the update χ_{k+1} is performed by combining physical information delivered through the gradient ∇_k with an image processing step, according to the following relation [59] :

$$\chi_{k+1} = N_{\theta k}(\nabla_k, \chi_k) \tag{3.36}$$

wherein the functions $N_{\theta k}$ identifies at each iteration the kth CNN, that maps measurements ∇_k to the contrast χ_k and the learned parameters θ_k (e.g., neural network weights).

Note that, the network architecture is the same among different iterations, while the network parameters are learned and therefore different in testing phase for each iteration. In particular, the CNN learns an update of the contrast χ_{k+1} by minimizing a loss function function (half-mean-squared-error) between the predicted updated contrast χ_{k+1} and the ground-truth χ_t.

The architecture of the proposed 3,CNNs-EPT is described in Figure 3.3(b). As the logic underlying the so-called U-net, it is characterized by two inputs on two different pipelines and one output. In fact, the network, starting from the complex contrast χ_k and the complex gradient ∇_k (i.e. the inputs), can be able to retrieve the unknown contrast χ_{k+1}. The inputs and output complexity is managed ny menas of two channels. The contracting path, in the left side, is a down-sampling process, consisting of repeated applications of convolutions, batch normalization (BN), and activation function (ReLU). In this phase, to maximize the features extracted in the layer before, the number of channels between layers is increased. The expansive path is an up-sampling process, where a transpose convolution replaces the process in contracting path

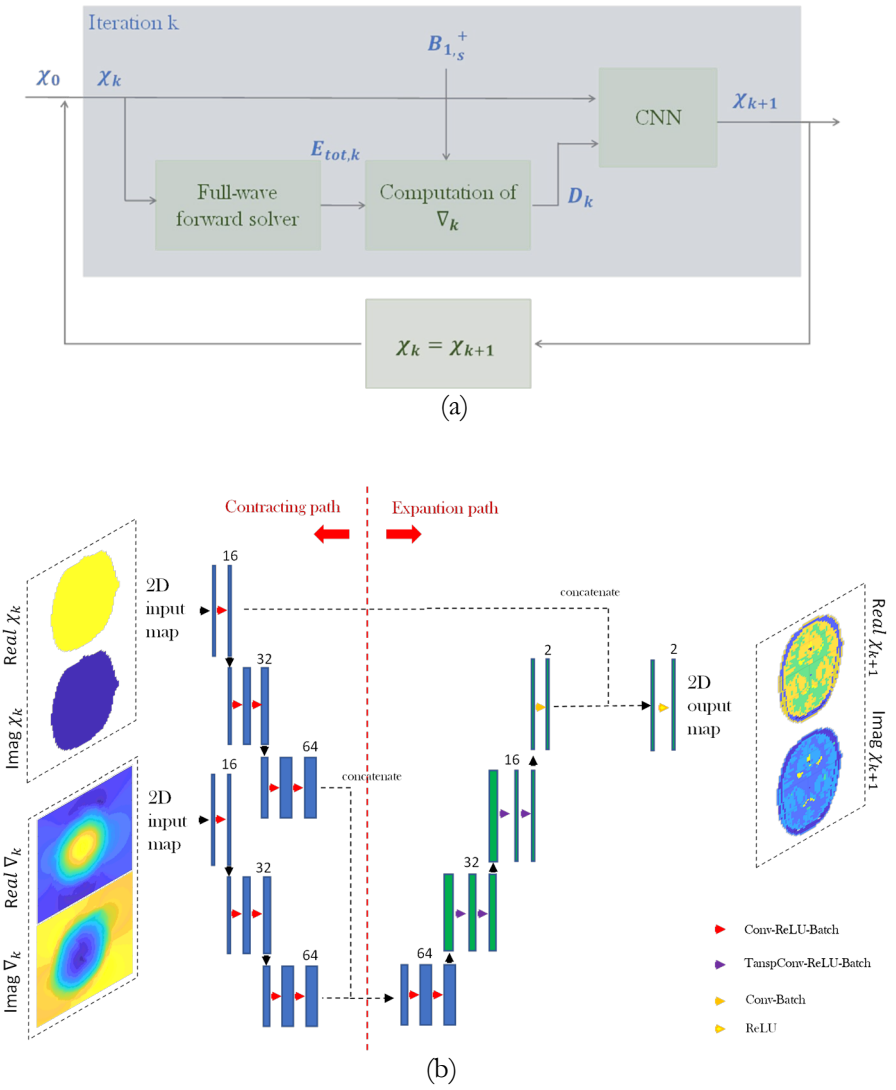

Figure 3.3: Block scheme reporting the main steps for training/testing the physics-assisted CNN procedure (a); CNN architecture (b).

to restore the original dimension. Contrary to the previous phase, the number of channels is reduced since the collected features must be combined to create an output image.

As for the other traditional neural networks, there is not a guideline for the choice of hyperparameters, not even for the choice of the sequence to be adopted in the definition of the layers (see Appendix B for additional information). However, there are some reasonable considerations that can be made in order to best address the issue at hand. The size of the filters is related to the spatial dimension of the input that a particular layer receives, while the number of filters used (therefore of feature maps generated) can be seen as a

degree of freedom that the user can exploit to steal more information. Another factor to consider is the concept of "deep", that means the depth of the network, i.e. the number of layers that compose it. Usually, in case of complex scenario and hard inverse problem, a single convolutional layer is not able to provide good performance, even by greatly increasing the number of filters. To cope with this issue the design of the proposed CNN architecture involves three convolutional (and corresponding transpose convolutional) layers. While the network architecture is the same through the iterations, the filters size becomes smaller and smaller (an 8x8 filter is considered for the first iteration, a 6x6 filter for the second and a 4x4 filter for the last one). This choice allows to obtain at the first iteration a 'coarse' image of the investigated scenario and then to go into detail by increasing the number of details collected in the following iterations.

Needless to say, all the hyperparameters of the implemented network that have been discussed so far and which will be detailed even later, are the outcome of several experiments and relative evaluations that influenced their selection (e.g. varying the learning rate, the number of epochs, the batch size, the number and the size of filters and so on). For the sake of brevity, therefore, only the best results are reported in this Thesis. Furthermore, the structure of the network, as described above, is not the only one of the conceivable configurations. Indeed, the major goal of the Thesis is to present the idea underlying the method, not the network itself.

Specifically, the network structure is kept relatively small because a compact structure is required to reduce the amount of memory required. Moreover, due to memory restrictions, we were only able to train one pair of samples at a time, for this reason in training we have chosen batch size BS=2.

The training is performed with Adam for 10, 20 and 30 epochs for the first, second and third iteration respectively. As far as the learning rate, we have considered a starting value of $5 \cdot 10^{-2}$ for the first iteration and then, decreasing by an order of magnitude with iterations. The results for the simulated data will be discussed in Section 3.9.

3.8 Numerical Experiments

Simulated data

In this paragraph the employed datasets and the idea behind the implementation of the two proposed methods are presented. Note that, for both the procedures, all computations, training and evaluation, have been trained using a home-made code developed in MATLAB environment, on a workstation equipped with two Intel(R) Xeon(R) CPU E5-2687W v3(3.10 GHz) processors.

Methods described in paragraphs 3.8 and 3.9 have been tested to retrieve EPs of a realistic human brain, starting from the corresponding scattered field $B_{1,s}^{+}$. We chose to train the algorithms with a supervised learning using simulated data, hence a meaningful data set is crucial for a successful training. The head phantoms adopted for the simulations have been obtained by exploiting the 3D morphological information gathered from a high-resolution voxel-based anthropomorphic phantom[63] , and by defining the EPs according to measurements collected from IT'IS foundation dataset [64].

A total of 120 brain models have been created by changing conductivity and permittivity values of the original 3D brain model and by including

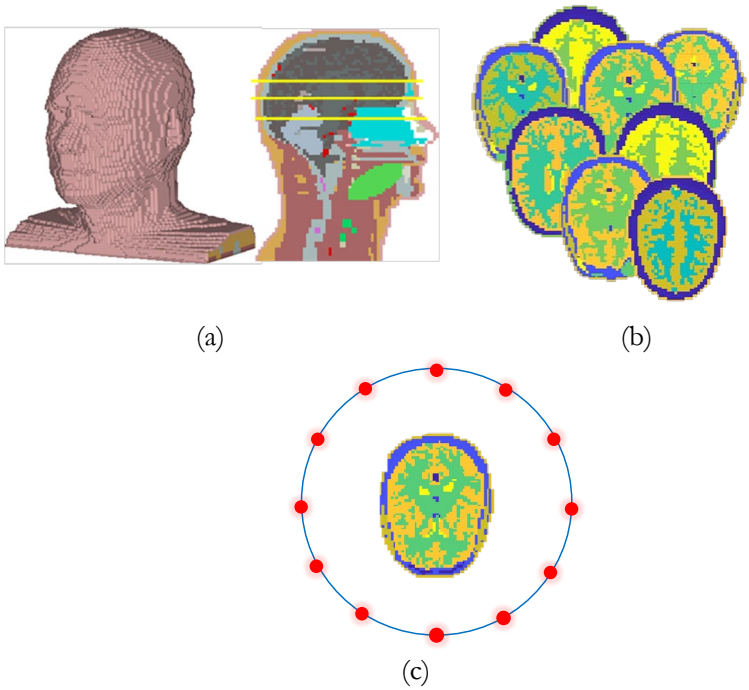

Figure 3.4: Initial 3D head model (a); different 2D slices obtained from the 3D model belonging to the training/testing dataset (b); The birdcage structure, schematized as a circular antenna array located around the head (c)

geometrical transformations, such as rotation [see figure 3.4(b)]. In particular, the conductivity and permittivity of the white and gray matter and CSF (Cerebrospinal Fluid) were changed in a range between 5% and 20%, with respect to the ones in [64] Starting from the above 3D models, 2700 2D training models, discretized with 120x120 number of cells, have been built by considering 27 slices for each brain model.

Two different training and testing datasets were considered for the 3,CNNs-EPT. The first training dataset includes 100 healthy head models (with the properties previously detailed, for a total of 2700 different slices); the second one includes the same healthy models but with additional 10 models with tumor-like anomalies. These additional head models are different from each other, also for both positions and EPs of the tumor. Hereafter we call these two training datasets $DS_{train,h}$ and $DS_{train,noh}$ respectively (where h stands for *healthy* and noh for *not-only healthy* profiles).

The 3,CNNs-EPT was tested considering an healthy dataset (including 20 head models) and a not-healthy dataset having the same head models but with a superimposed anomaly. Again, hereafter we call these two testing datasets $DS_{test,h}$ and $DS_{test,nh}$. Furthermore, other tests were then conducted considering different cases of tumors.

Simulation setup

As the current work is a theoretical evaluation of the performance of the proposed method, in the following a 2D configuration has been considered without RF shield. For SDM-based procedure a known distribution of the phase of $B_{1,s}^{+}$ has been assumed. Instead, for the CNN-based procedure tests have been performed with two different phase assumptions:

- Case (A), a known distribution of the phase of B_1^+ has been assumed;
- Case (B), an approximated distribution of the phase of B_1^+, has been assumed for a more realistic case to be considered (see

paragraph 3.2). This last case to see the impact of the transceive phase assumption on permittivity/conductivity reconstructions.

The data have been simulated by using a full wave forward simulator based on the method of moments. The birdcage structure has been schematized as a circular antenna array located around the head (see Figure 3.4(c)), with radius $r = 0.37\,m$, in accordance with the realistic size of common birdcage coil adopted in clinic[51]. The number of antennas has been set equal to 16 and modelled as line sources evenly spaced on the circumference of radius r.

The training phase for SDM stops when the desired threshold is reached (see paragraph 3.6). In the following, 9 iterations have been needed for SDM. As far as the CNN-based iterative procedure, 3 iterations have been considered because no further improvement was observed in the reconstructed conductivity/permittivity maps (see paragraph 3.7).

The initial model X_o for the iterative reconstruction procedure, both for the training and testing stage, has been modeled as a homogeneous head with EPs set equal to average value of the ones of the brain tissues, i.e. $\sigma \approx 0.56$ S/m and $\varepsilon \approx 45$.

The accuracy of the retrieved EPs has been appraised through the normalized mean square error (NMSE):

$$NMSE = \frac{\|\chi - \tilde{\chi}\|^2}{\|\chi\|^2} \tag{3.37}$$

where χ is the actual complex permittivity/conductivity of the profile and $\tilde{\chi}$ is the estimated one.

Furthermore, the accuracy of the most relevant tissues in a brain (i.e. WM, GM, CSF and tumor-like anomaly, when it is present) has been assessed through the mean absolute percentage error (MAPE):

$$MAPE = \frac{1}{\mathrm{n}} \sum \frac{|\chi_t - \tilde{\chi}_t|}{|\chi_t|} \tag{3.38}$$

where χ_t is the actual complex permittivity/conductivity of the tissue and $\tilde{\chi}$ is the estimated one. This parameter provides a global estimate of the tissues reconstruction quality across all head models.

Moreover, in both cases to estimate in a systematic and quantitative way the retrieved EP maps, an extensive numerical analysis was carried out and reported in Subsections 3.9.1-3.9.3.

3.9 Results and discussion

In this Section, we report some numerical examples concerning the two procedures described in Section 3.6-3.7. In particular, at first, we provide a comparison between the two procedures, then a comprehensive analysis of several case studies obtained by 3,CNNs-EPT is next presented.

3.9.1 Physics-assisted learning approaches: A comparison

Figures 3.5 and 3.6 show some preliminary testing results in case of noiseless data for both procedures. The case of a contrast profile (conductivity/permittivity) belonging to the training dataset is depicted in Figure 3.5 (a), with the retrieved EP maps in Figure 3.5 (b),(c). Instead, Figure 3.6 (a) shows the same EP profiles (conductivity/permittivity) but with inside an anomaly that the network has never seen during the training. The retrieved conductivity/permittivity maps are depicted in Figure 3.6 (b),(c). The chosen slice (and the relative profile whose it belongs) has similar anatomical structure (without anatomical deformations) but different electromagnetic properties with respect to the training samples. Note that these results have been obtained training procedures only with healthy profiles.

To give a qualitative impression of the reconstructions, the errors of the different reconstruction methods, the absolute error maps for EP reconstructions is also reported in figures.

These results show that in some cases the proposed approaches are able to estimate the EPs of the tissues with high accuracy, especially in case of known profiles or known anatomical structures. On the other hand, when the profiles have different anatomical structure or are very different from the training samples (i.e with some anomalies inside), the NMSE increases,

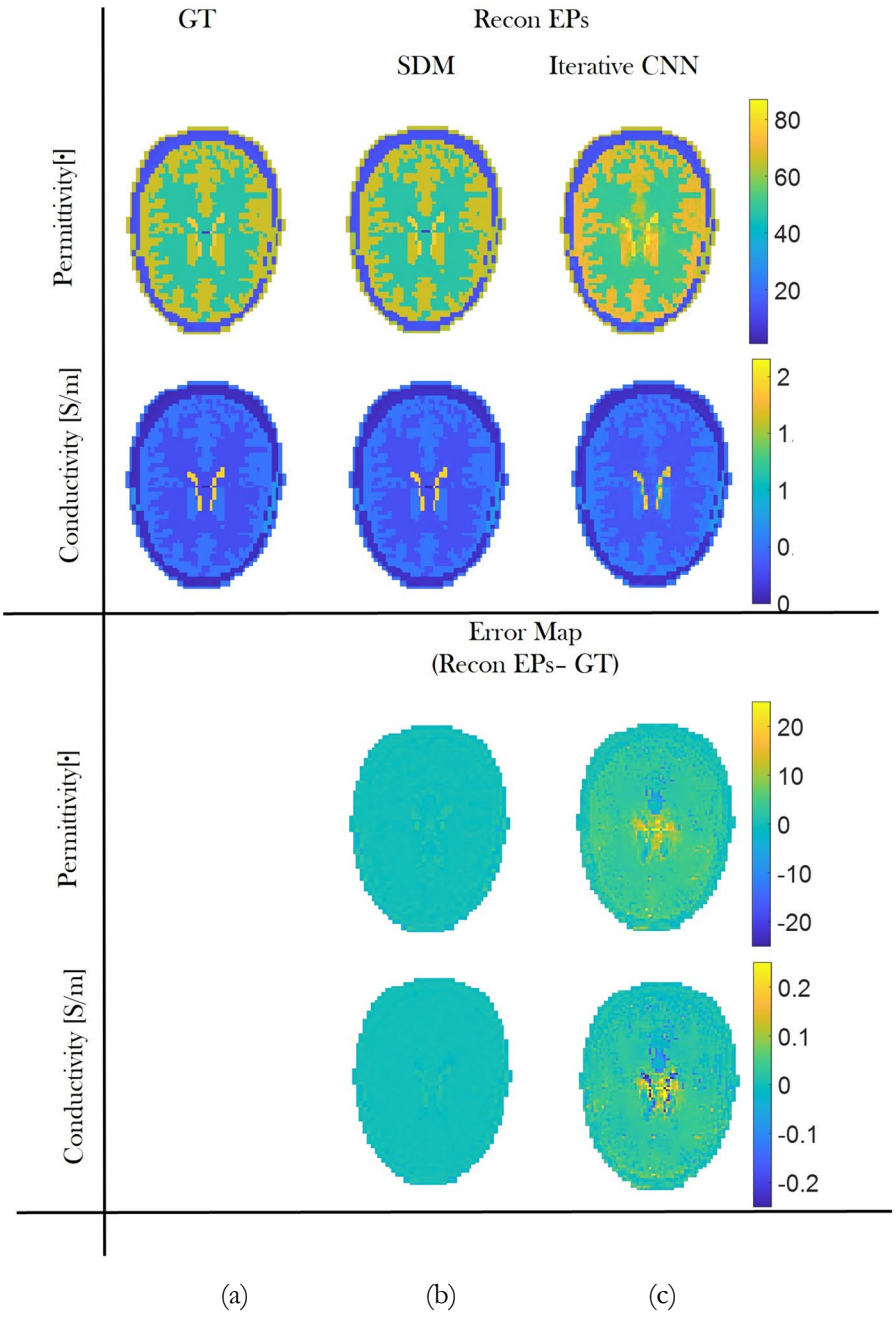

Figure 3.5: Reconstructed EP maps (conductivity and permittivity) of a healthy brain model, top. Ground-truth (a). Retrieved profiles by means the procedures in Section 3.8 – 3.9; with SDM (NMSE=0.0002) (b), with iterative CNN (0.037) (c). The absolute error maps for EP reconstructions (b),(c) on the bottom.

especially with the SDM-based approach. Yet, this is anyway low and the retrieved EPs maps in both cases can be used as convenient starting guess for

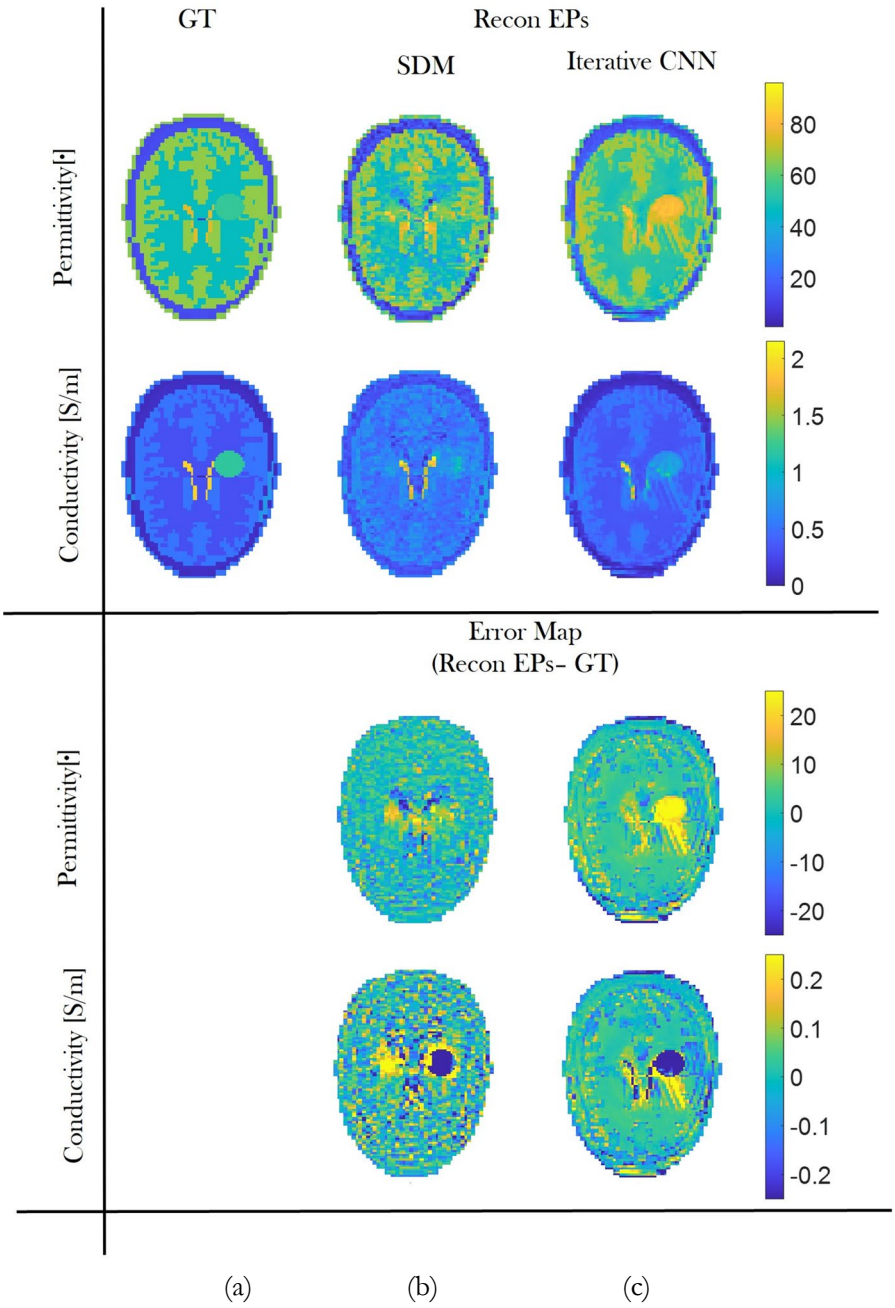

Figure 3.6: Reconstructed EP maps (conductivity and permittivity) of a brain model with a tumor-like anomaly, top. Ground-truth (a). Retrieved profiles by means the procedures in Section 3.8 – 3.9; with SDM (NMSE=0.0002) (b), with iterative CNN (0.037) (c). The absolute error maps for EP reconstructions (b),(c) in the bottom.

a standard iterative inversion procedure (for instance CSI-EPT) thus reducing the related computational time[51].

As a final comment, the computational time required for the reported numerical results is approximately 39 minutes for the training stage (that is

performed only once, for a total of 17 iterations) and 6 minutes for the single slice of the testing stage, in case of the SDM procedure. For what concerns the 3,CNNs-EPT the training takes about 2 hours per iteration, while the single slice is retrieved in about ten seconds.

Evident from this comparison is one of the issues experienced when applying such a kind of procedures. Learning methods, indeed, are a great way to improve the retrieval process underlying MRI-EPT. However, the biggest issue is the generalization ability, as shown in the following results. Indeed, when the test sample differs significantly from to the training set, the reconstruction may be less accurate. In order to improve the ability of the SDM-based approach in Section 3.6, as a future work a larger and more heterogeneous datasets are planned to be adopted in the training stage. However, this can imply the disadvantage of increasing the computation cost and time required in the training stage. Moreover, improved results can be also reached by adopting a regularization technique to solve problem 3.33 different from Tikhonov one.

3.9.2 3,CNNs-EPT: Case study (A): A known distribution of the phase of $\boldsymbol{B_1^+}$

Figures 3.7-3.8 show EPs reconstructions for each iteration at 3 T, both for noiseless and noisy simulated $B_{1,t}^+$ data of a healthy slice belonging to $DS_{test,h}$ (i.e. a testing dataset with only healthy head models). Results have been obtained training the 3,CNNs-EPT with $DS_{train,h}$ (i.e. the training dataset with only healthy head models). In particular, in case of noisy data, a white Gaussian noise with a SNR=18 dB has been superimposed on the real and imaginary part of the total field. Results with and without noise, show good conductivity and permittivity reconstructions, also at tissues boundaries. However, adding noise results in a blurred effect as it is visible from the conductivity as well as permittivity maps.

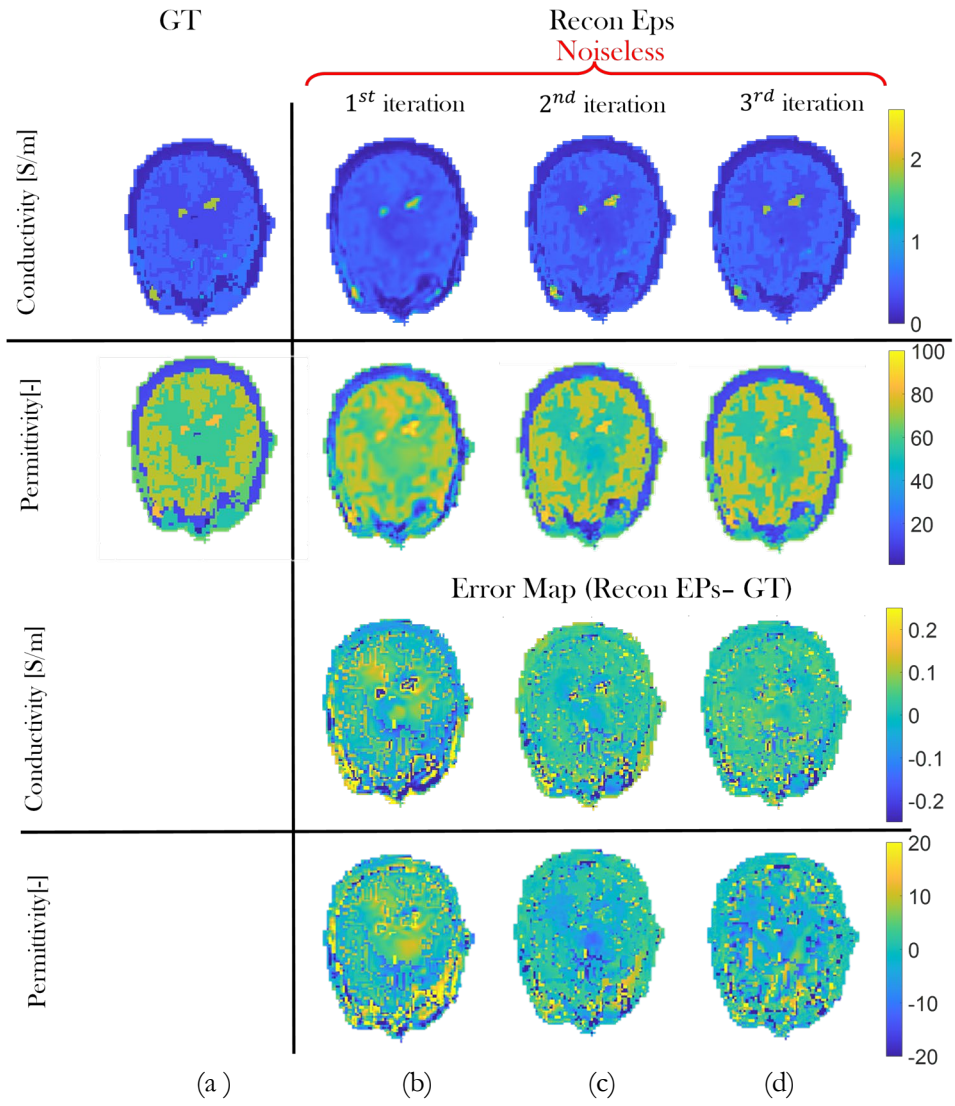

Figure 3.7 Reconstructions (of conductivity and permittivity) in case of known $\boldsymbol{B_{1,t}^{+}}$ phase noiseless. Ground-truth (a), Retrieved EPs maps for each iteration for a slice of a healthy brain model (b)-(d) top; error maps (Reconstructed – Ground-truth) (b)-(d) bottom

Figures 3.9-3.10 show EPs reconstructions for each iteration at 3 T, both for noiseless and noisy (SNR=18 dB) simulated $B_{1,t}^{+}$ data of the same slice in Figures 3.7-3.8, but with a tumor-like anomaly in the upper part of the brain (belonging to $DS_{test,nh}$.). Interestingly, the network is able to infer the presence of the anomaly, even if the networks has processed only healthy profiles. The good performances are also confirmed from a quantitative point of view. Indeed, the NMSEs are equal to 0.07 and 0.09 at the first iteration and 0.04 and 0.07 at the third iterations respectively for the cases shown in Figures 3.7-3.8.

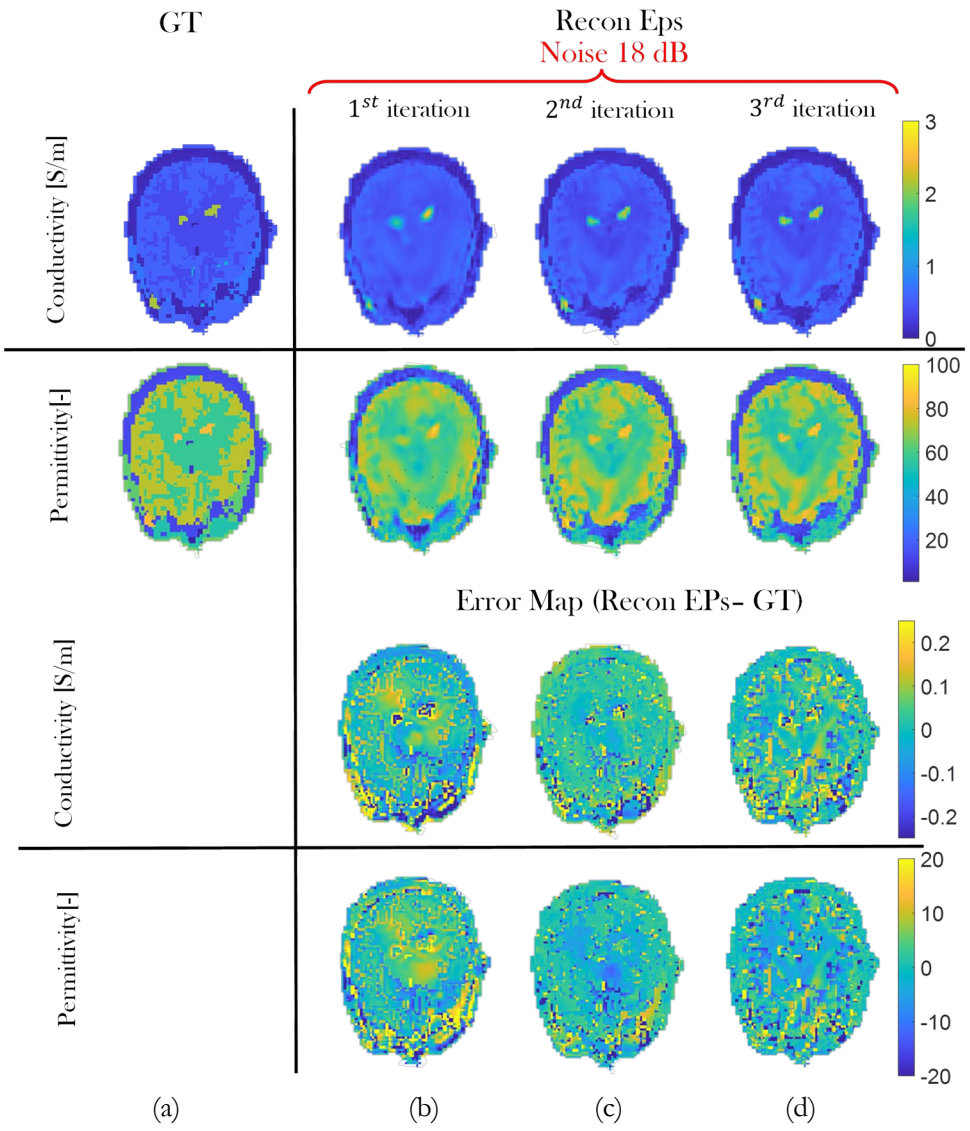

Figure 3.8 Reconstructions (of conductivity and permittivity) in case of known $\boldsymbol{B}_{\mathbf{1},t}^{+}$ phase and noisy data. Ground-truth (a), Retrieved EPs maps for each iteration for a slice of a brain model with tumor-like anomaly (b)-(d) top; error maps (Reconstructed – Ground-truth) bottom (b)-(d).

Instead as regards the cases shown in Figures 3.9-3.10, the NMSEs are equal to 0.09 and 0.11 at the first iteration and 0.06 and 0.1 at the third iterations respectively.

However, the reconstruction accuracy of the lesion is lower compared to the other tissues. Indeed, the conductivity is underestimated. Conversely the permittivity map shows overestimated permittivity values

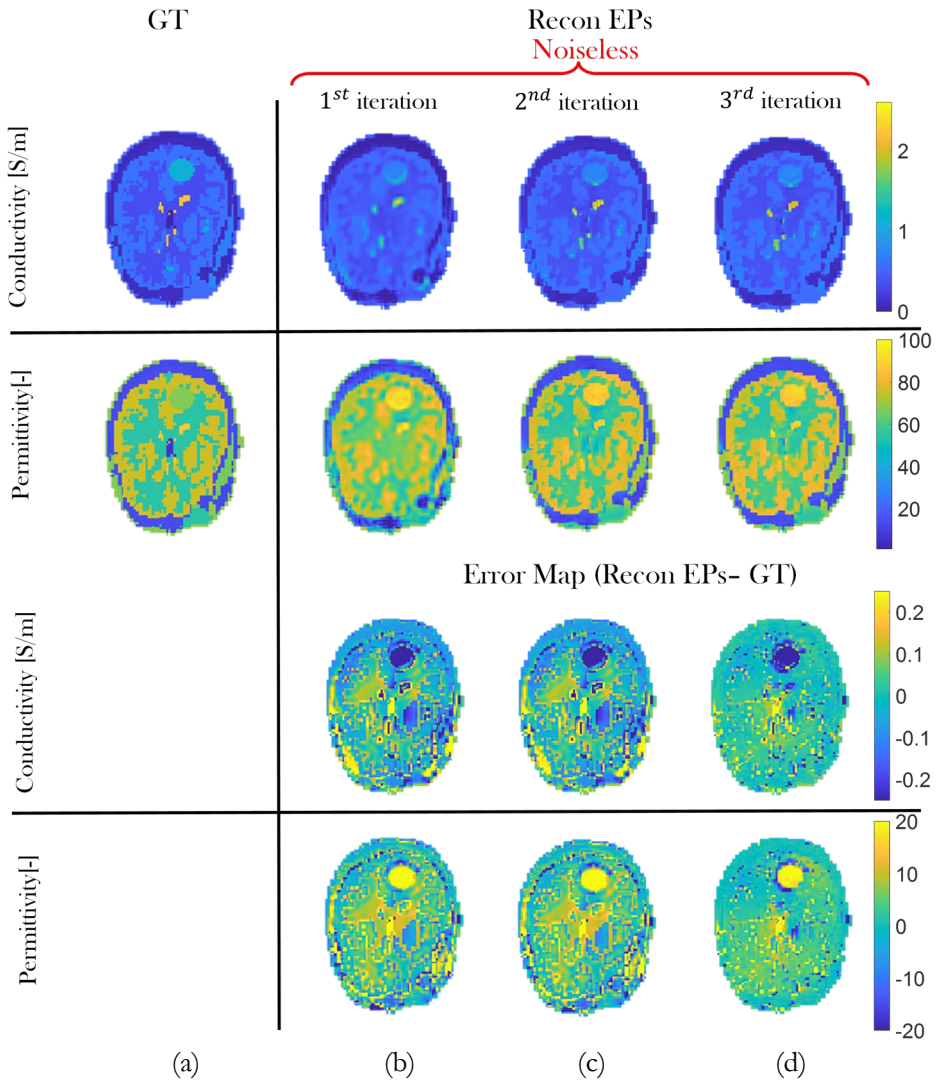

Figure 3.9: Reconstructions (of conductivity and permittivity) in case of known $\boldsymbol{B}_{1,t}^{+}$ phase noiseless. Ground-truth (a), Retrieved EPs maps for each iteration for a slice of a brain model with tumor-like anomaly (b)-(d) top; error maps (Reconstructed – Ground-truth) (b)-(d) bottom.

Reconstructions with noisy data confirm the network's ability to detect an anomaly but some details are lost within the brain. Therefore, as the previous cases, adding noise results in a blurred effect as it is visible from both the conductivity and permittivity maps. These sentences are also confirmed by the quantitative analysis conducted on the reconstructed EPs maps reported in Table 1.

The quantitative analysis was carried out on the single tissues, revealing the mean and standard deviation (std) respect to the true reference values (GT). Table 1 reports, indeed, the mean and std values for the slices in Figure 3.7-3.8 (a) and in Figure 3.9-3.10 (b). Even with some variations, it becomes evident that the reconstructed values are near to the real ones (GT, marked in red in Table 1). In particular, these results show that, as the iterations increase, the reconstructed values are closer to the GT, and also the standard deviation tends

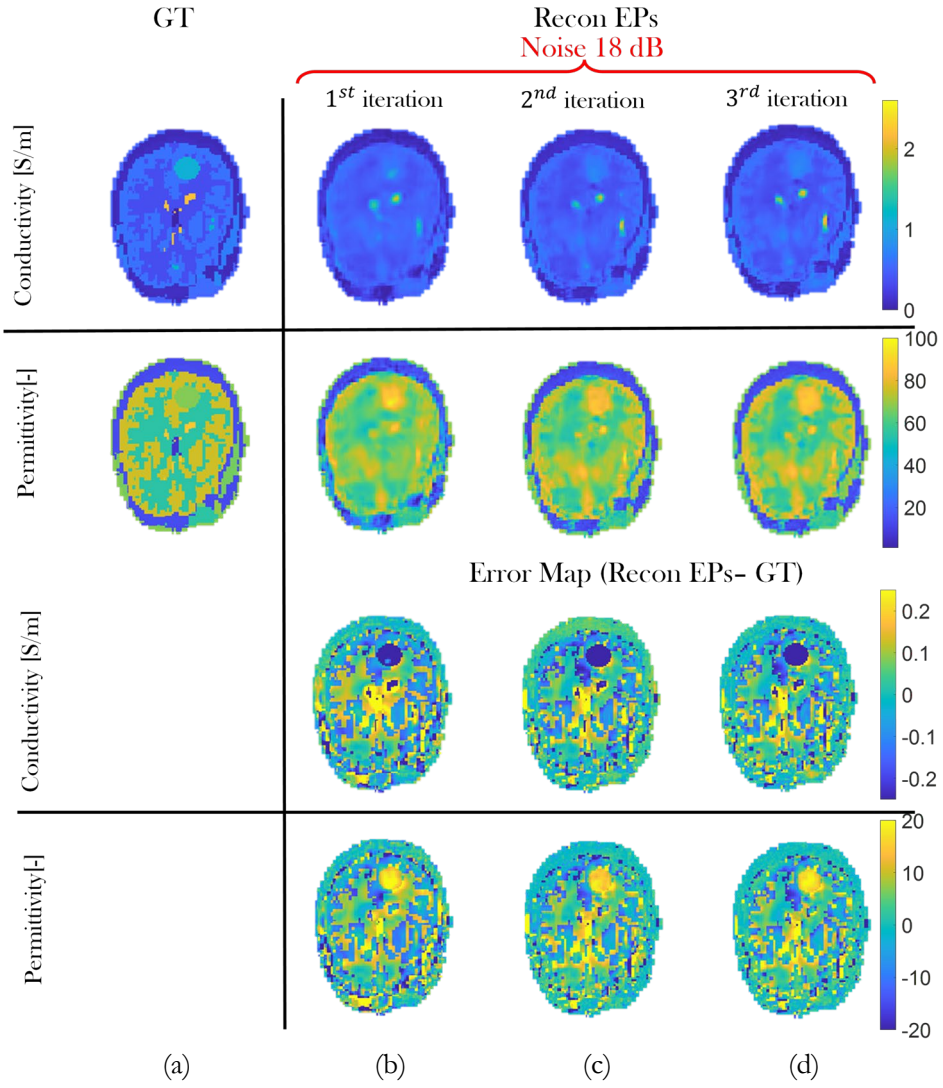

Figure 3.10: Reconstructions (of conductivity and permittivity) in case of known $\boldsymbol{B_{1,t}^{+}}$ phase with noise 18 dB. Ground-truth (a), Retrieved EPs maps for each iteration for a slice of a brain model with tumor-like anomaly (b)-(d) top; error maps (Reconstructed – Ground-truth) (b)-(d) bottom.

to decrease.

KNOWN $B_{1,t}^{+}$ PHASE		WM				GM				CSF			
		GT	RECONSTRUCTED			GT	RECONSTRUCTED			GT	RECONSTRUCTED		
			Iter 1	Iter 2	Iter 3		Iter 1	Iter 2	Iter 3		Iter 1	Iter 2	Iter 3
			MEAN ± STD				MEAN ± STD				MEAN ± STD		
Permittivity [-]	Noiseless	52.5	61.5 ±5.9	56.4 ±6.4	57.7 ±6	73.5	72.2 ±7.6	73.2 ±6.9	74.3 ±6.8	84.04	82.9 ±8.7	82.6 ±9.6	83.8 ±9.4
	Noise 18 dB		60 ±5.3	60 ±6.68	59 ±6.9		66.3 ±8.1	67.7 ±10.1	68 ±10.21		71 ±8.8	72 ±11.8	73 ±11.4
Conductivity [S/m]	Noiseless	0.38	0.44 ±0.01	0.42 ±0.1	0.4 ±0.1	0.64	0.57 ±0.1	0.61 ±0.01	0.63 ±0.01	2.35	1.47 ±0.6	2.02 ±0.64	1.96 ±0.55
	Noise 18 dB		0.49 ±0.12	0.45 ±0.11	0.46 ±0.13		0.55 ±0.09	0.55 ±0.13	0.56 ±0.14		1.3 ±0.6	1.17 ±0.6	1.31 ±0.67

(a)

KNOWN $B_{1,t}^{+}$ PHASE		WM				GM				CSF				TUMOR			
		GT	RECONSTRUCTED			GT	RECONSTRUCTED			GT	RECONSTRUCTED			GT	RECONSTRUCTED		
			Iter 1	Iter 2	Iter 3		Iter 1	Iter 2	Iter 3		Iter 1	Iter 2	Iter 3		Iter 1	Iter 2	Iter 3
			MEAN ± STD				MEAN ± STD				MEAN ± STD				MEAN ± STD		
Permittivity [-]	Noiseless	52.5	61.5 ±5.9	57 ±6.4	58.2 ±6	73.5	71.5 ±7.6	72.7 ±6.9	73.7 ±6.8	84.04	82.7 ±8.7	81.7 ±9.6	82.1 ±9.4	65	87 ±8.7	83.8 ±9.6	84.2 ±9.4
	Noise 18 dB		60.9 ±5.4	61.2 ±6.9	60.7 ±7		69 ±8.4	67.4 ±10.6	67.6 ±10.7		72.2 ±8.2	72.1 ±10.5	72.2 ±10		81 ±5.3	79 ±3.5	80 ±3.9
Conductivity [S/m]	Noiseless	0.38	0.44 ±0.01	0.42 ±0.1	0.43 ±0.1	0.64	0.57 ±0.1	0.60 ±0.01	0.62 ±0.01	2.35	1.44 ±0.6	1.94 ±0.64	1.86 ±0.55	1.2	0.81 ±0.6	0.8 ±0.64	0.81 ±0.55
	Noise 18 dB		0.5 ±0.12	0.46 ±0.11	0.47 ±0.12		0.55 ±0.09	0.54 ±0.13	0.56 ±0.15		1.18 ±0.5	1.07 ±0.52	1.20 ±0.61		0.68 ±0.12	0.69 ±0.06	0.72 ±0.05

(b)

Table 1: Mean and standard deviation of retrieved EPs maps, for a slice of a healthy brain model (a) with tumor-like anomaly (b). The values have been retrieved for all the iterations, considering the cases with and without noise on $\boldsymbol{B1_t^+}$ data.

The loss of some details, more evident in the case with noise, emerges in the figures through the blur effect and translates into a slight deviation from the true reference values in terms of the parameters collected in Table 1.

Obviously, since the reconstructed profiles are completely unknown to the network, this is something expected.

Table 1, confirms that he reconstruction accuracy of the tumor is lower compared to the other tissues. In absence of noise on data, a possibility to improve the reconstructions is to consider the output of the 3,CNNs-EPT as initial guess for a standard resolution method, f.i. CSI-EPT. The example is reported in Figure 3.11. As it is clear from the figure, the combination of the

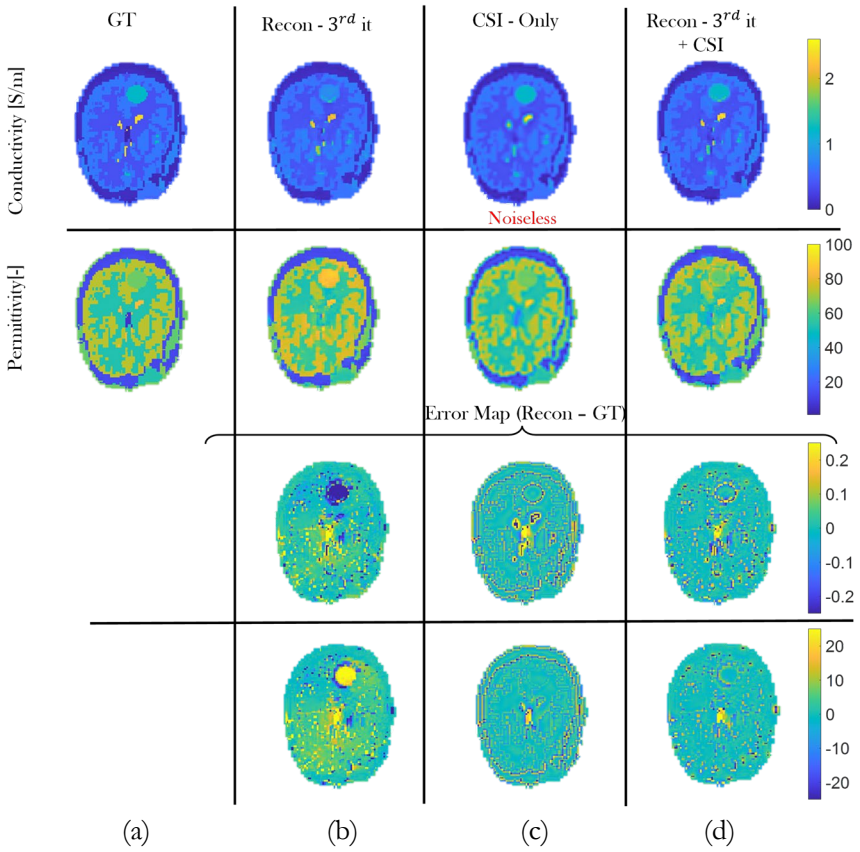

Figure 3.11 Reconstructions (of conductivity and permittivity) in case of known $\boldsymbol{B_{1,t}^{+}}$ phase noiseless, for a slice of a brain model with tumor-like anomaly. Ground-truth (a), Retrieved EPs maps with 3,CNNs-EPT (b), with CSI-EPT only (c) and combining 3,CNNs-EPT with CSI-EPT, top; error maps (Reconstructed – Ground-truth) (b)-(d) bottom.

two methods improves considerably the reconstruction accuracy of the tumor, as it is confirmed from values in Table 2. Reconstructions obtained with CSI-EPT depend on the map provided as initialization guess. If a homogeneous initial guess is provided (Figure 3.11 (c)), smooth tissues reconstructions are obtained for a noiseless situation in about two hours (hundreds of iterations).

	GT	1^{th} iter	2^{th} iter	3^{rd} iter	3^{rd} iter + DL	CSI only
Noiseless		MEAN ± STD	MEAN ± STD	MEAN ±STD	MEAN ±STD	MEAN ±STD
Permittivity [-]	65	87±8.7	83.8±9.6	84.2±9.4	66 ± 6.9	65 ± 2.53
Conductivity[S/m]	1.2	0.81±0.6	0.8±0.64	0.81±0.55	1.1 ±0.24	1.17 ±0.08
Reconstruction time		**≈ 0.06s**	**≈ 0.06s**	**≈ 0.06s**	**≈ 94s**	**≈ 1.78h**

Table 2: Mean and standard deviation of tumor for a slice of a brain model with tumor-like anomaly, in three cases: only the 3,CNNs-EPT, only CSI-EPT and combining 3,CNNs-EPT with CSI-EPT. The values have been retrieved considering the cases without noise on $\boldsymbol{B1_t^+}$ data.

The combined conductivity and permittivity values of the tumor are closer to the GT than in the case of 3,CNNs-EPT only (Figure 3.11 (b)), showing an advantage in using the output from the 3,CNNs-EPT as the initialization guess for CSI-EPT. Furthermore, by using the proposed method to provide an optimal initial guess for CSI-EPT, less iterations are needed, thus considerably reducing the CSI-EPT reconstruction time (about minutes for a single slice).

However, in cases with noise, CSI-EPT does not give excellent results without proper a regularization. In such a case, a possible solution is reported in the next Subsection.

In Figure 3.12 the boxplots, with the average error trends evaluated through MAPE indicator, for the reconstruction of the main brain tissues are shown. Results have been obtained considering all the head models belonging to $DS_{test,nh}$ (i.e. 20 head models for 27 slices each one) and they are related to the permittivity values, but a similar trend is also obtained in terms of conductivity. The figure shows the cases of noiseless and noisy data.

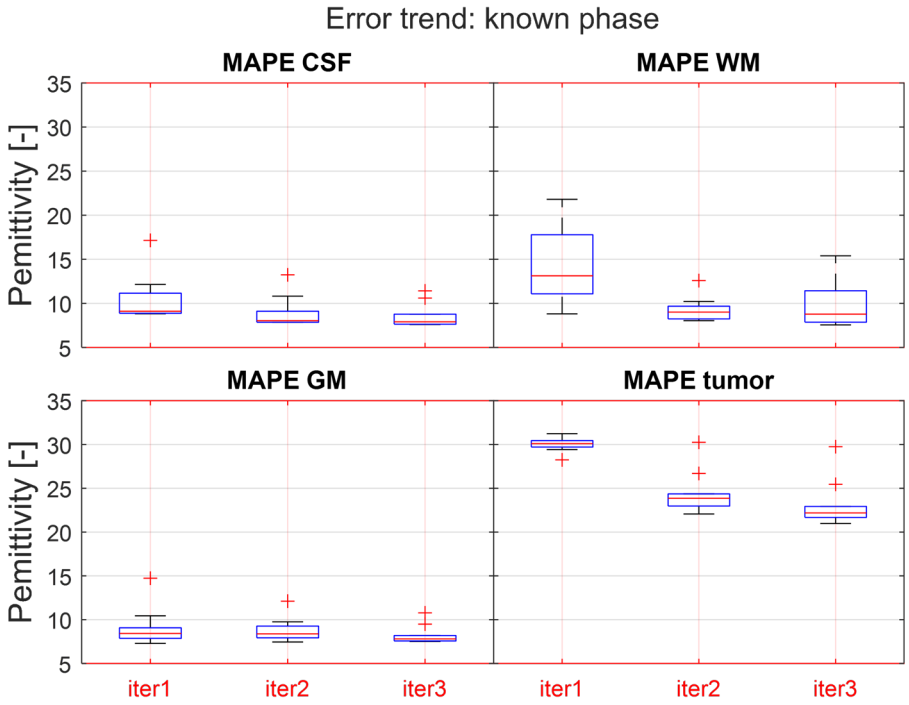

(a)

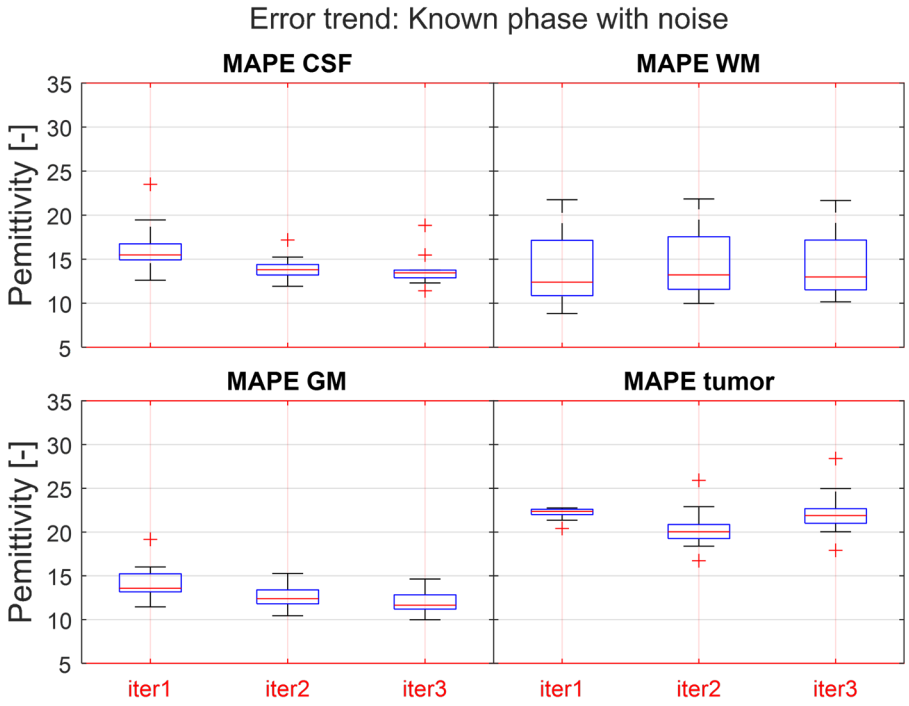

(b)

Figure 3.12: The boxplots showing the median MAPE (with the 25th-bottom edge and 75th -top edge percentiles), for WM, GM, CSF and tumor-like anomaly permittivity reconstructions across the head models in $\boldsymbol{DS_{test,nh}}$., without noise (a) and with noisy $\boldsymbol{B^{+}_{1,t}}$ data (SNR=18 dB) (b).

The red line in the box represents the median MAPE. The two segments

that start from the box and extend upwards and downwards are called "whiskers" and define the expected range of values. The outliers (values different from the median one) are represented in the boxplot as isolated red crosses positioned above the whiskers of the distribution.

As the boxplots show, the median at the third iteration is almost always kept around 10% for GM, WM and CSF in case (a), while the median MAPE of tumor permittivity ≈ 25%; with the addition of noise, case (b), there is a slight general increase. Moreover, the median values tend to decrease from one iteration to the other, for all the tissues, which confirms the effectiveness of the iterative procedure.

3.9.3 3,CNNs-EPT: Case study (B): Approximated distribution of the phase of B_1^+

The same considerations of the previous shown cases can be extended in this section. Figures 3.13-14 show EPs reconstructions for each iteration at 3T, both for noiseless and noisy approximated $B_{1,t}^+$ data of the pathological slice (belonging to $DS_{test,nh}$), also analysed in Section 3.9.2, but in case of TPA (see section 3.2). Results have been obtained training the 3,CNNs-EPT with the $DS_{train,h}$.

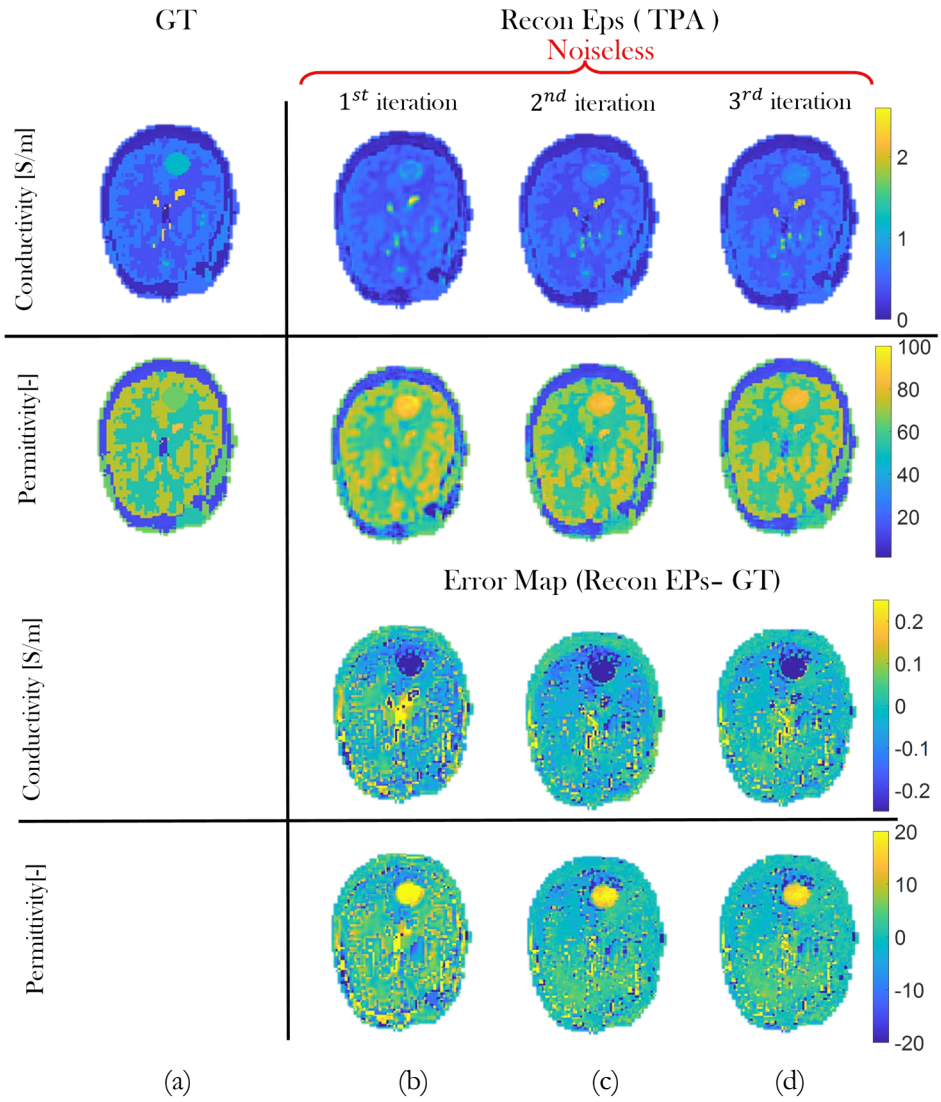

Figure 3.13: Reconstructions (of conductivity and permittivity) in case of TPA for $\boldsymbol{B}_{1,t}^{+}$ noiseless. Ground-truth (a), Retrieved EPs maps for each iteration for a slice of a brain model with tumor-like anomaly (b)-(d) top; error maps (Reconstructed – Ground-truth) on the bottom (b)-(d).

The results show the 3,CNNs-EPT is able to accurately retrieve the EPs maps. Indeed, the NMSE are equal to 0.08 and 0.14 at the first iteration and 0.06 and 0.1 at the third iteration, respectively.

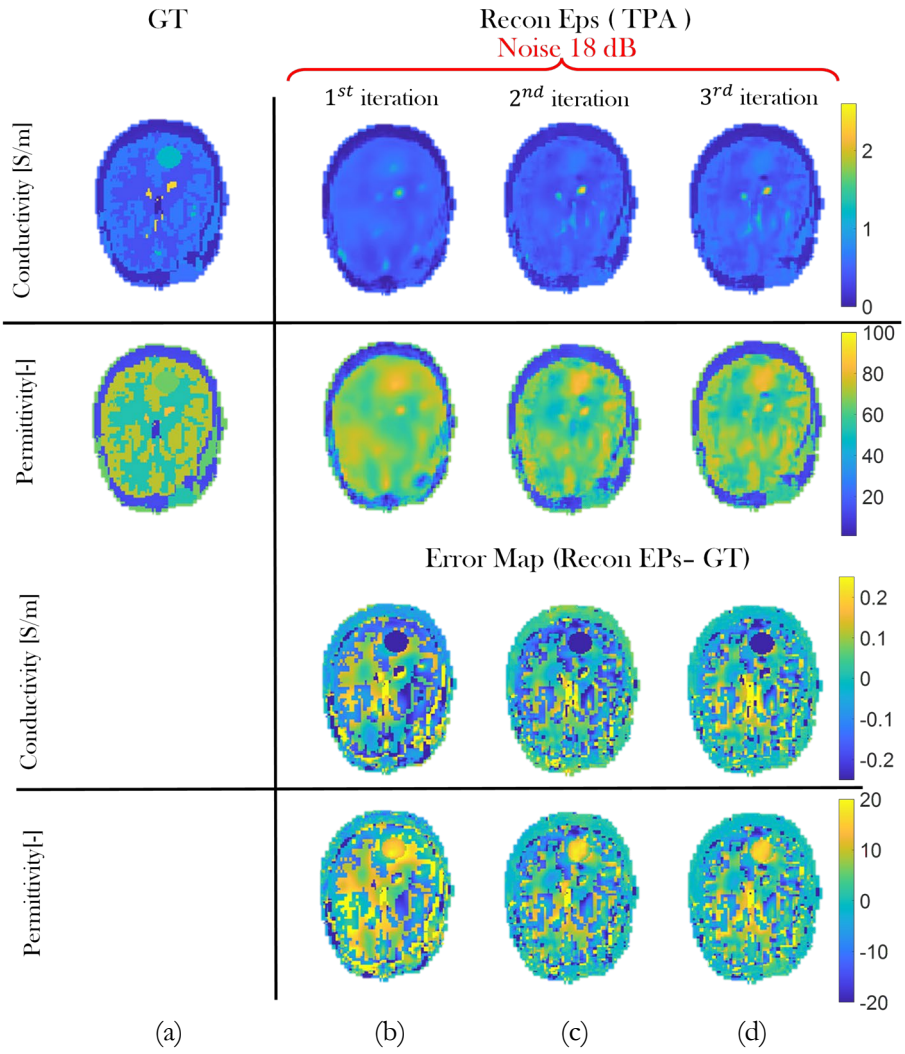

Figure 3.14: Reconstructions (of conductivity and permittivity) in case of TPA for $\boldsymbol{B}_{1,t}^{+}$ with noise 18 dB. Ground-truth (a), Retrieved EPs maps for each iteration for a slice of a brain model with anomaly (b)-(d) top; error maps (Reconstructed – Ground-truth) (b)-(d) bottom.

An additional analysis on the single tissues was carried out also in case of TPA assumption. Table 2(a) reports the mean and std values of the retrieved EPs maps for the slices in Figures 3.13-3.14. Even with some variations, the reconstructed values are near to the real ones (i.e. the GTs, whose values are marked in red in Table). These values remain close to GT even for noisy cases. The network is able to discriminate between the different tissues, but among all, the CSF is the one that is reconstructed worst.

APPROXIMATED $B^+_{1,t}$ PHASE		WM				GM				CSF				TUMOR			
		GT	RECONSTRUCTED			GT	RECONSTRUCTED			GT	RECONSTRUCTED			GT	RECONSTRUCTED		
			Iter 1	Iter 2	Iter 3		Iter 1	Iter 2	Iter 3		Iter 1	Iter 2	Iter 3		Iter 1	Iter 2	Iter 3
			MEAN ± STD				MEAN ± STD				MEAN ± STD				MEAN ± STD		
Permittivity [-]	Noiseless	52.5	58.7 ±6.27	55.5 ±6	55.8 ±6	73.5	71 ±7	70 ±8	71 ±7.5	84.04	78 ±6.5	78 ±12	75 ±11	65	86 ±5.7	80 ±4.7	80 ±4
	Noise 18 dB		64.9 ±5.3	58.7 ±6.68	59.84 ±6.9		67.5 ±8.1	65.1 ±10.1	67 ±10.2		69.4 ±8.8	69.7 ±11.8	70.8 ±11.4		79 ±5.3	78.5 ±3.5	78.2 ±3.9
Conductivity [S/m]	Noiseless	0.38	0.43 ±0.1	0.38 ±0.09	0.41 ±0.1	0.64	0.57 ±0.09	0.55 ±0.1	0.59± 0.1	2.35	1.62 ±0.5	1.73 ±0.57	1.75 ±0.54	1.2	0.77 ±0.13	0.68 ±0.08	0.72 ±0.08
	Noise 18 dB		0.46 ±0.12	0.43 ±0.11	0.46 ±0.13		0.51 ±0.09	0.50 ±0.13	0.55 ±0.14		0.79 ±0.6	1.07 ±0.6	1.08 ±0.67		0.63 ±0.12	0.59 ±0.06	0.66 ±0.05

(a)

APPROXIMATED $B^+_{1,t}$ PHASE			WM			GM			CSF			TUMOR			
			GT	RECONSTRUCTED			RECONSTRUCTED			RECONSTRUCTED			RECONSTRUCTED		
				Iter 1	Iter 2	Iter 3	Iter 1	Iter 2	Iter 3	Iter 1	Iter 2	Iter 3	Iter 1	Iter 2	Iter 3
				MEAN ± STD			MEAN ± STD			MEAN ± STD			MEAN ± STD		
Permittivity [-]	Noise 18 dB	$DS_{train_{noh}}$	52.5	63 ±4.7	63 ±6.4	62 ±7	73.5	66 ±8.1	70 ±10.1	69 ±11	84.04	71.5 ±7	74.4 ±7	72.2 ±8	65	**75 ±3.1**	**57 ±7.7**	**48 ±5.1**
		DS_{train_h}		64.9 ±5.3	58.7 ±6.68	59.84 ±6.9		67.5 ±8.1	65.1 ±10.1	67 ±10.2		69.4 ±8.8	69.7 ±11.8	70.8 ±11.4		79 ±5.3	78.5 ±3.5	78.2 ±3.9
Conductivity [S/m]		$DS_{train_{noh}}$	0.38	0.5 ±0.09	0.46 ±0.13	0.44 ±0.11	0.64	0.51 ±0.09	0.52 ±0.1	0.53 ±0.1	2.35	0.98 ±0.44	1.17 ±0.58	1.12 ±0.58	1.2	**0.69 ±0.1**	**0.87 ±0.2**	**0.97 ±0.1**
		$DS_{train_{noh}}$		0.46 ±0.12	0.43 ±0.11	0.46 ±0.13		0.51 ±0.09	0.50 ±0.13	0.55 ±0.14		0.79 ±0.6	1.07 ±0.6	1.08 ±0.67		0.63 ±0.12	0.59 ±0.06	0.66 ±0.05

(b)

Table 3. Mean and standard deviation of retrieved EPs maps, for a slice of a brain model with tumor-like anomaly, in TPA assumption. Retrieved values with and without noise on $\boldsymbol{B1^+_t}$ data (a). A comparison between the retrieved values obtained by training the network with $\boldsymbol{DS_{train_{noh}}}$ and $\boldsymbol{DS_{train_h}}$ (b) and considering noise on $\boldsymbol{B1^+_t}$ data.

In Figure 3.15, the permittivity and conductivity reconstructions of different brain models, again in case of noisy $B^+_{1,t}$ data and TPA assumption, are shown demonstrating for all cases good reconstruction quality. These cases have been considered to test the procedure capability to detect also anomalies located in different region of the brain and characterized by different EPs (in the shown cases, $\varepsilon_r = 54\ or\ 74$) respect to previews shown cases. which is successful, but at most the variable EPs influence the overestimation of the tumor. Note that, the results shown so far have been obtained by training the 3,CNNs-EPT with the healthy dataset. As it can be seen from the figure, the position and the Eps of the pathology do not affect the detection.

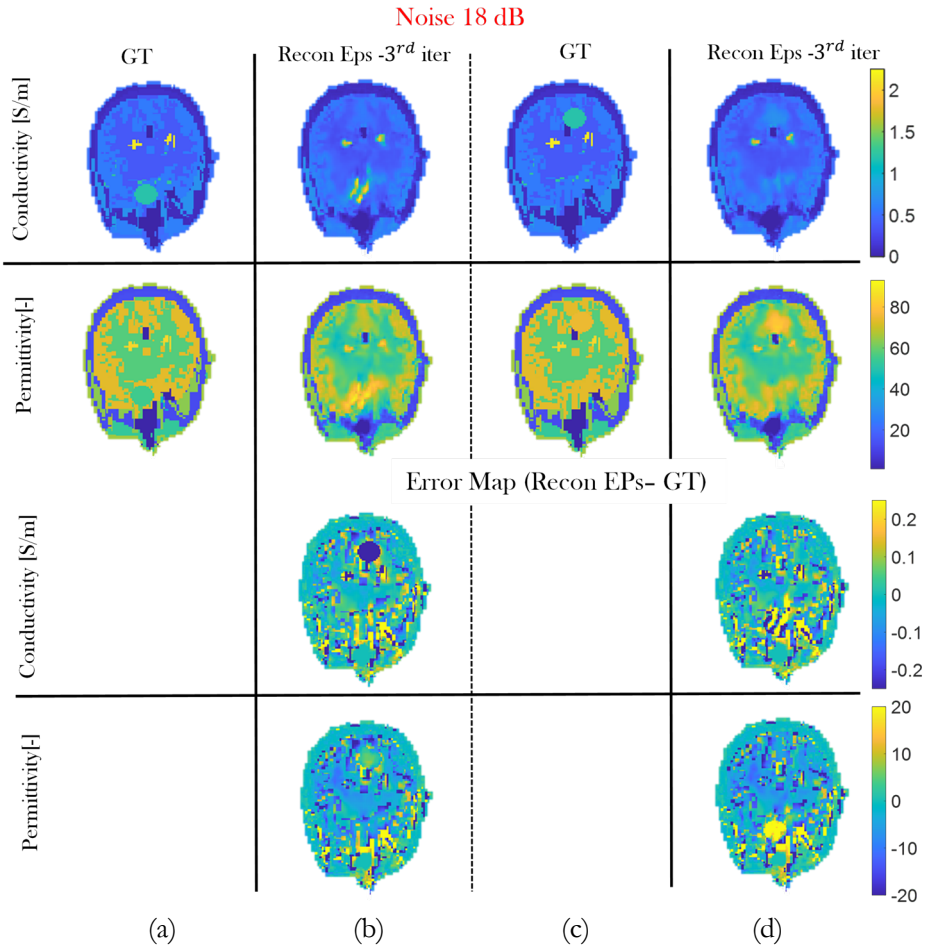

Figure 3.15: Reconstructions (of conductivity and permittivity) in case of TPA for $\boldsymbol{B}_{1,t}^{+}$ data with noise 18 dB. Ground-truth with tumor-like anomaly with the same EPs but in different position inside the brain(a-c), Retrieved EPs maps for each iteration for a slice of a brain model with anomaly (b)-(d) top; error maps (Reconstructed – Ground-truth) (b)-(d) bottom.

Therefore, the common trend in results shows that, in cases of slices with anomaly, if there is noise on the data, the permittivity and conductivity of the tumor are in some cases over- and underestimated, respectively. One possibility to circumvent such an occurrence is to consider a different dataset to train the network (see section 3.8), which also includes head models with pathology. This allows the network to generalise these cases more effectively, as it is confirmed by the following results.

In this respect, an example is reported in Figure 3.16. In noiseless cases, even when a healthy data set is used, the tumor is well estimated, Figure 3.16(b).

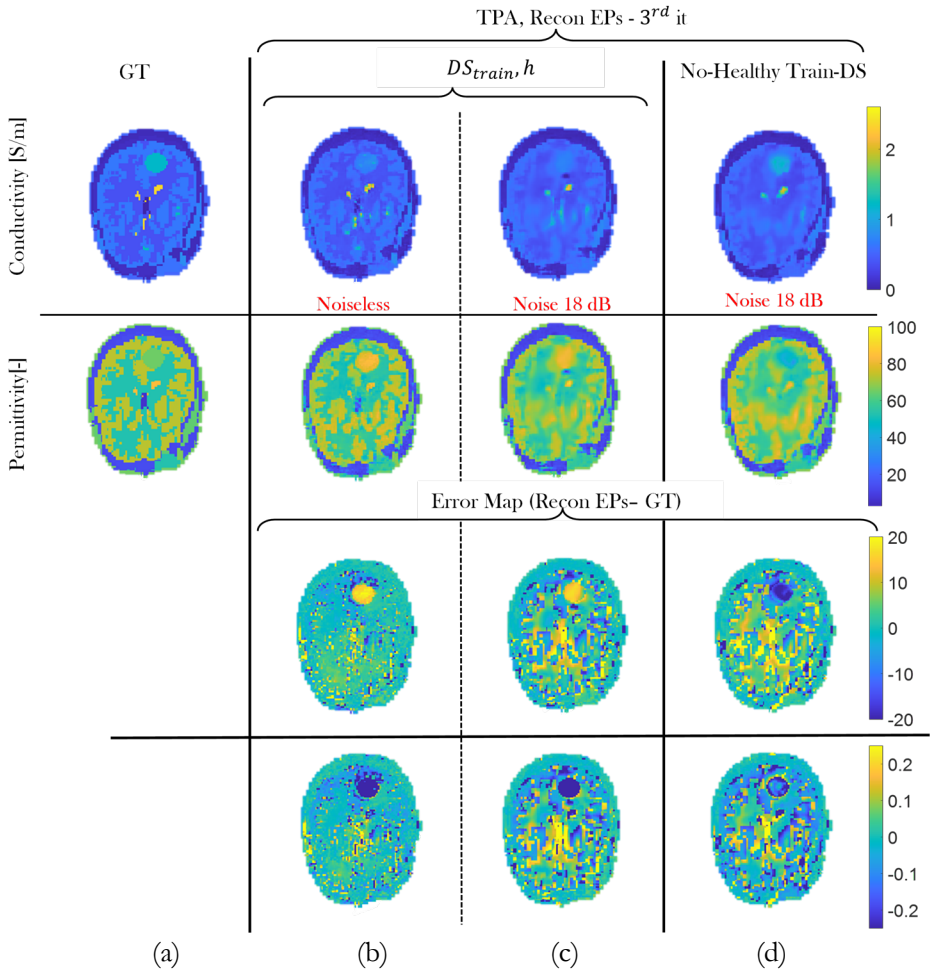

Figure 3.16: Reconstructions (of conductivity and permittivity) in case of TPA for $\mathbf{B}^{+}_{1,t}$ data without and with noise (18 dB). Ground-truth with tumor-like anomaly (a); Retrieved EPs maps with $\boldsymbol{DS_{train,h}}$ without (b) and with noise(c); Retrieved EPs maps with $\boldsymbol{DS_{train,nh}}$ with noise (d) on top; error maps (Reconstructed – Ground-truth) (b)-(c)-(d), bottom.

However, the situation worsens with noise, Figure 3.16 (c). a better situation is in Figure 3.16(d), which depicts the reconstruction generated by training the 3,CNNs-EPT with the $DS_{train,noh}$. Evidently, the trend has been reversed; both conductivity and permittivity of tumor are no longer under- and overestimated, respectively. Note that, like all the other presented cases, the selected slice to be retrieved has different geometric and morphological features than the ones in training, this is also true for the tumor values. This trend is also confimed from values in Table 2(b), which show how the permittivity and conductivity values of the reconstructed tumor considering

$DS_{train,noh}$ are more in line with the reference ones (GT), compared to the same case obtained considering $DS_{train,h}$.

The quantitative analysis has been carried out also with the TPA. In Figure 3.17 the boxplots, with the average trends evaluated through MAPE indicator, for the reconstruction of the main brain tissues are shown. Results has been obtained considering the head models in $DS_{test,noh}$ and they are related to permittivity values (similar trends are also obtained in terms of conductivity). The figure shows the worst case (b), i.e. considering corrupted data with 18 dB of noise. Better results are obviously obtained otherwise (a). The average error trends are also here confirmed, median MAPE decreases from one iteration to the other and the more challenging cases are the reconstructions with noise. In general, the introduction of a model error, i.e. a field phase approximation, does not affect the reconstructions.

In summary, in this Chapter two physic-assisted learning strategies for MRI-EPT have been proposed and compered. The first based on a SDM methods, the second on a cascade of CNNS. These methods were tested on 2D simulated human brain data. The presented results demonstrate the feasibility of this methodology to reconstruct conductivity and permittivity maps at 128MHz. In particular, best results have been obtained with the proposed 3,CNNs-EPT. It allows good quality permittivity and conductivity reconstructions for both noiseless and noisy cases in few seconds. Ultimately, this method allows computational advantages compared to standard contrast source inversion electrical properties tomography (CSI-EPT), i.e. faster reconstructions, which will be extremely relevant when moving to 3D reconstructions.

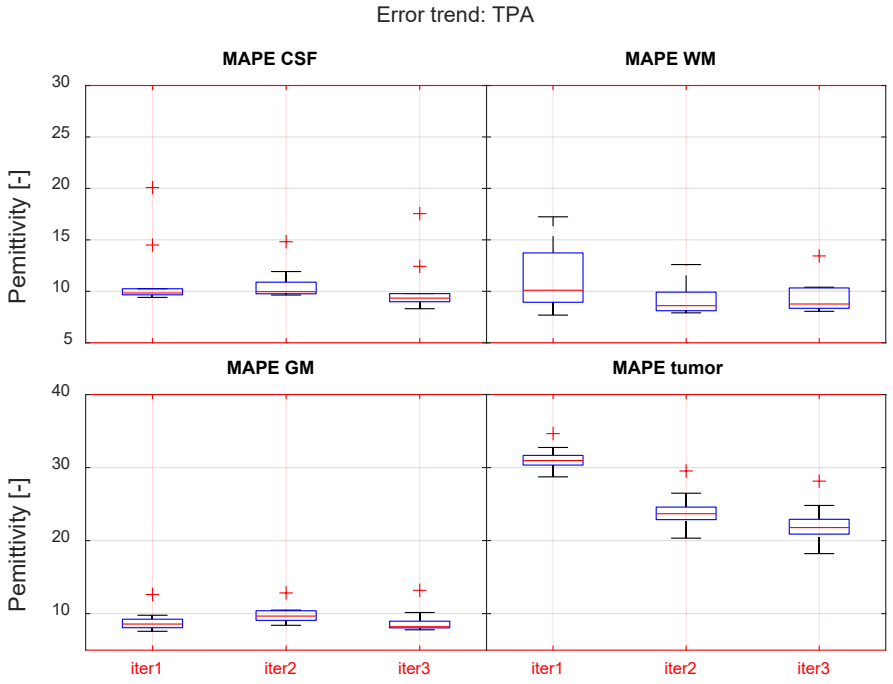

(a)

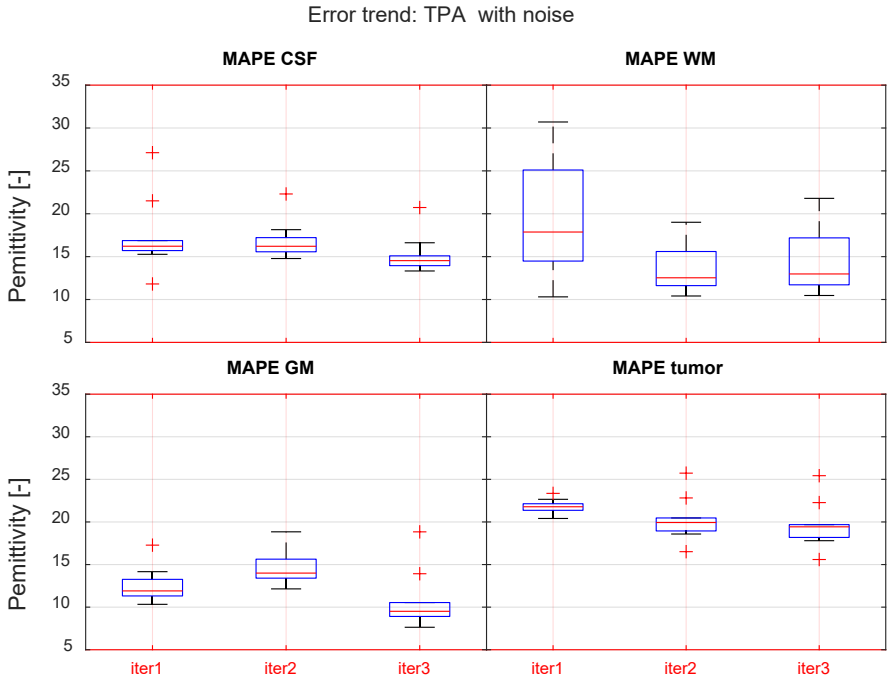

(b)

Figure 3.17: The boxplots showing the median MAPE (with the 25th-bottom edge and 75th -top edge percentiles), for WM, GM, CSF and tumor-like anomaly permittivity reconstructions across $\boldsymbol{DS_{test,nh}}$, without noise (a) and with nosy $\boldsymbol{B^{+}_{1,t}}$ data (SNR=18 dB) (b).

4 Optimized MRI RF-Shimming via field amplitude shaping

This Chapter aims at outlining, discussing, and assessing a new physics-based procedure for RF Shimming via field intensity shaping. The general concept that led to the writing of these findings was the development of a multi control points-based shaping procedure for the specific case of RF shimming in an MRI system. Initially, we addressed the problem applying and extended a shaping approach already published in [23]. Unfortunately, this proved to be computationally expensive in several circumstances, therefore an physic based model to optimize it was investigated. As a result, the developed auxiliary model drastically reduces the recurring possibilities in the enumeration procedure. The analysis of the auxiliary model and numerical results in the challenging case of RF shimming against different 2D head phantoms are detailed in the Section 4.3[3].

4.1 Introduction

One of the main challenges to be address in MRI is the RF shimming, which consists in ensuring a significant homogeneity of the transmit magnetic field in the anatomical region to be imaged, while ensuring the SAR limits in the other body regions [71]. This need arises especially in HF-MRI (especially at high and ultra-high fields) because the high field frequency causes fluctuations in the magnetic field and an increase in SAR, which lead to image degradation (i.e image artifacts [73]). Therefore, the more homogeneous the field, the better the quality and resolution.

Several strategies have been developed in order to simultaneously improve B_1^+ homogeneity and also to reduce the SAR level. However, most of them do not consider the complex excitation currents related to the RF coil [7]. Generally, these techniques fall in two macro categories: passive and active shimming techniques.

[3] Some contents of this Chapter have been published in references [3] [5] [6] [9] and [15] of the Publications List of Sabrina Zumbo reported at the end of the Thesis.

The first category commonly uses specific materials as shims, such as iron pieces or high-permittivity, low-conductivity materials. Indeed, High-permittivity materials (HPMs) placed between RF coils and the subject have been proposed as a method for varying the spatial distribution of the B_1^+ field, independent of RF shimming or parallel transmission, to improve field homogeneity or enhance SNR in targeted regions [74], [77], [78].

For instance, in [74] a method to evaluate the effect of integrated high-permittivity materials (HPMs) on the B_1^+ homogeneity and global SAR is proposed. Furthermore, the use of HPMs in combination with RF coils has also been shown to reduce overall required input RF power in transmission and improve coil sensitivity at a variety of field strengths in reception, both in experiments and numerical simulations [74]. In [79] the dielectric shimming is formulated as an electromagnetic scattering problem using integral equations.

On the other side, the active shimming uses small coils (or shim-coils). However, many shim-coils are necessary to obtain an accurate shimming with an increased magnet cost. In the active shimming techniques, the B_1^+ inhomogeneity can be addressed by using transmit arrays and applying RF shimming or parallel transmission techniques [7]. These techniques can be optimized to also reduce global Specific Absorption Rate (SAR), since constructive interferences between the electric fields from multiple transmit coils can result in undesired hot-spots.

In this Thesis, a novel active RF shimming approach is introduced by employing a completely new perspective. Specifically, the proposed approach relies on the paradigm of field intensity shaping. Indeed, this paradigm can be employed to ensure a uniform radiofrequency (RF) field B_1^+ and, thus, adequate image resolution and accuracy. Indeed, field intensity shaping consists in generating a field intensity distribution with some desired characteristics in a specific ROI, such as f.i. intensity, uniformity, sidelobes levels. This problem, , is relevant not only in MRI shimming but also in a wide range of applications, including antenna synthesis for radar and communications [65], [66] energy replenishment [67], [68] through-the-wall imaging [69] and biomedical

applications [70], [71] . As far as these latter are concerned, field intensity shaping plays a key role in hyperthermia treatment planning, wherein one aims to increase the temperature inside a tumor by means of a proper antenna array applicator, while keeping under control the heating in the surrounding healthy tissues [70].

In this respect, in this Thesis, by tacking advantage from the procedures in [6] and inspired to mt-FOCO [23,] the proposed strategy for RF shimming via field intensity shaping, exploits different control points located in the ROI and is able to take contemporaneously into account all constraints regarding polarization, strength of the B_1^+ Field and SAR. The convexity of the proposed procedure, closely linked to the phase shift between the various field patterns, ensures to achieve the global minimum of the problem and, hence, an accurate, repeatable, and optimal solution of the shimming problem. In this respect, the phase shifts between the fields at specific control points are assumed as auxiliary unknown variables of the problem. However, since the optimal phase shifts are not a priori known, one has to determine it by exploring the set of possible phase shifts using enumerative or global optimizations. As a consequence, the computational burden grows rapidly if the number of control points increases, and this circumstance may prevent the use of this paradigm in a number of actual applications.

To cope with issue, a simple auxiliary and physics inspired model for the induced total field is proposed for shaping the field intensity. The model allows a relatively simple physical understanding of convenient and non-convenient fields interferences to be exploited in the shaping problem, and hence a drastic reduction of the computational burden related to its solution via optimization procedure. In particular, it allows to obtain in an easy fashion convenient field distributions within the ROI that one can fit to address the shaping problem. Also, in those cases where stringent shaping constraints are present, the use of the auxiliary model allows a significant resize of the set of possible phase shifts to be considered with respect to [23], [24].

In the following sections, the findings will be provided. First, we briefly summarize the basic underlying mt-FOCO. Then, the new active shimming procedure based on mt-FOCO is introduced. Moreover, the proposed auxiliary model for the induced total field is described and analyzed in a homogeneous medium. Finally, the overall proposed procedure is tested against a 2D realistic head phantom.

4.2 Multi target-Focusing via Constrained Optimization

In order to provide a basis for the approach proposed in this Chapter, it is useful to recall rationale underlying mt-FOCO [23].

Let us assume known the geometry as well as the electromagnetic properties of the bidimensional scenario under test D (i.e. relative permittivity $\epsilon_r(\underline{r})$ and electric conductivity $\sigma(\underline{r})$), wherein the ROI is embedded. Moreover, let us consider N elementary monochromatic electric sources surrounding D.

With reference to scheme in Figure 4.1 and indicating with $\underline{r}$ a generic point of D, the overall electric and magnetic field can be expressed as[48]

$$\underline{B}(\underline{r}, I_n) = \sum_{1}^{N} I_n \, \underline{b}_n(\underline{r}) \qquad (4.1\ a)$$

$$\underline{E}(\underline{r}, I_n) = \sum_{1}^{N} I_n \, \underline{e}_n(\underline{r}) \qquad (4.1\ b)$$

wherein ($\underline{e}_n$, $\underline{b}_n$) are the total electric and magnetic fields induced by the unitary excited n-th antenna when all the other antennas are off, while I_n are the complex excitation coefficients of the signals feeding the antenna array.

Without loss of generality, let us assume that one of the electromagnetic field components is dominant above the other ones or the optimal/desired polarization of the electromagnetic field distribution is a priori known.

Then, the optimization shaping problem can be formulated as follows:

"Determine the optimal set of complex excitations coefficients I_n *such to produce the desired behavior of the amplitude of the dominant field component in the ROI, while enforcing some constraints in other regions of D".*

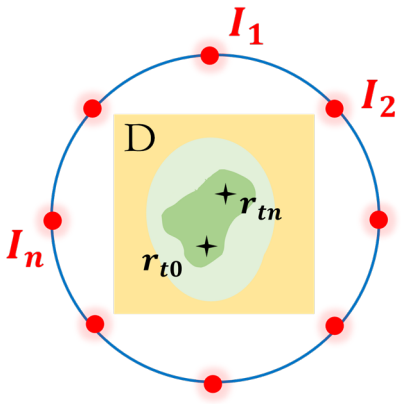

Figure 4.1: Sketch of the scenario under test. The ROI, enlighten by a green background, contains the control points indicated by the black stars. N elementary monochromatic electric sources indicated by grey circles surround the investigation domain D.

To be more specific, one usually aims at maximizing the amplitude of the field as well as ensuring its uniformity in the ROI. This is the case of microwave hyperthermia or MRI shimming. Instead, SAR limits or other kind of upper bounds are usually enforced in the whole D or in $D \backslash ROI$. Unfortunately, these requirements usually involve the solution of a non-convex problem. As such, by using local as well as global optimization procedures (because of the involved computation burden for large N) the global optimality of the solution cannot be ensured.

In order to circumvent such a problem, according to *multi control points*-based approaches [23], [24] the problem can be formulated as follows:

$$\max_{I_n} \sum_{k=0}^{L} \left[Re\{F(\underline{r}_{t_k}, I_n)\}^2 + Im\{F(\underline{r}_{t_k}, I_n)\}^2 \right] \qquad (4.2)$$

subject to:

$$\left|F(\underline{r}_{t_i}, I_n)\right| = |F|_i \qquad with\ i = 1, \dots, L \quad (4.2\ a)$$

$$\left|F\left(\underline{r}, I_n\right)\right|^2 \leq UB\left(\underline{r}\right) \qquad (4.2\ b)$$

wherein $\underline{r} \notin ROI$ or $\underline{r} \in D$ depending on the application at hand; r_{t_i} $(\mathrm{i} = 1, \ldots, \mathrm{L})$ are L controls points belonging to the ROI; F is the dominant/desired polarization of the electric or magnetic field depending on the application at hand; while $|F|_i$ is the desired value for the field amplitude at the i-th control point. In case of uniformity requirement, $|F|_i = \left|F\left(\underline{r}_{t_0}\right)\right|$, being $\underline{r}_{t_0}$ the reference point. Finally, Re and Im are the real and the imaginary parts of the corresponding argument, respectively.

The objective function (4.2) ensures the maximization of the field amplitude in the ROI, while constraints (4.2 a) and (4.2 b) are able to ensure the uniformity in the ROI and keep under control its amplitude in other regions, respectively. In this respect, $UB(\underline{r})$ refers to the field upper bound, which takes on different values depending on the problem to be solved. Note that, depending on the application at hand, the cost function can be eventually replaced by other functions, for instance the minimum ripple of the square amplitude of F [81].

According to *multi control points*-based approaches, in order to circumvent its non-convexity, the problem (4.2) can be simplified as follows [23] :

$$\max_{I_n} Re\left\{F\left(\underline{r}_{t_0}, I_n\right)\right\} \qquad (4.3)$$

subject to:

$$Im\left\{F\left(\underline{r}_{t_0}, I_n\right)\right\} = 0 \qquad (4.3\ a)$$

$$Re\left\{F\left(\underline{r}_{t_i}, I_n\right)\right\} = |F|_i cos\Delta\phi_i \qquad (4.3\ b)$$

$$Im\left\{F\left(\underline{r}_{t_i}, I_n\right)\right\} = |F|_i \sin\Delta\phi_i \qquad (4.3\ c)$$

$$\left|F\left(\underline{r}, I_n\right)\right|^2 \leq UB\left(\underline{r}\right) \qquad (4.3\ d)$$

wherein $\Delta\phi_i \in [0,2\pi[$ are the auxiliary variables indicating the phase shifts between the field in $\underline{r}_{t_0}$ and $\underline{r}_{t_i}$. In the above problem, the field in $\underline{r}_{t_0}$ is assumed real by simply changing the overall phase reference. Then, the objective function becomes linear. Moreover, the constraints (4.2 a) have been conveniently turned into (4.3 b) and (4.3 c).

For any fixed instance of $\Delta\phi_i$ values, problem (4.3) recasts the shaping problem as the maximization of a linear function in a convex set, which corresponds to a convex programming (CP) problem [23] . Then, the globally optimal solution of the overall optimization problem can be a posteriori determined by looking into the values of the cost function or other suitable performance indicators depending on the application at hand. Notably, when all the different possible combinations for $\Delta\phi_i$ are explored, one is able to guarantee the global optimality of the final array excitations[23], [24].

In the following section, the *multi control points* paradigm for field intensity shaping is tailored for the more challenging case of MRI shimming. In particular, the RF shimming is set up for the first time by exploiting one or more control points located in the ROI and by taking contemporaneously into account the constraints regarding SAR levels and polarization purity.

4.3 RF shimming via mt-FOCO

Let us consider a birdcage coil made up of N conductors, each of which is fed by a different current I_n (with $n = 1,\dots,N$), then the optimization problem can be formulated as follows:

"Determine the optimal set of complex excitations coefficients I_n such to produce the uniform and maximum B_1^+ field in the ROI, while ensuring polarization purity and SAR limits in the overall D".

From a mathematical point of view, by exploiting the rationale of problem (4.3), reformulating the whole problem in terms of the magnetic field, the RF shimming problem can be cast as follows:

$$\max_{I_n} Re\{B_1^+(\underline{r}_{t_o}, I_n)\} \tag{4.4}$$

subject to

$$Im\{B_1^+(\underline{r}_{t_0}, I_n)\} = 0 \tag{4.4 a}$$

$$Re\{B_1^+(\underline{r}_{t_i}, I_n)\} = Re\{B_1^+(\underline{r}_{t_0}, I_n)\} * cos\Delta\phi_i \tag{4.4 b}$$

$$Im\{B_1^+(\underline{r}_{t_i}, I_n)\} = Re\{B_1^+(\underline{r}_{t_0}, I_n)\} * sin\Delta\phi_i \tag{4.4 c}$$

$$SAR(\underline{r}, I_n) \leq 3.2\frac{W}{kg} \quad \underline{r} \in D \tag{4.4 d}$$

$$\left|B_1^-(\underline{r}, I_n)\right|^2 \leq \frac{1}{3}\left|B_{1,initial}^+(\underline{r}, I_n)\right|^2 \quad \underline{r} \in D \tag{4.4 e}$$

$$\left|B_1^+(\underline{r}, I_n)\right|^2 \leq \left|B_{1\,des}^+\right|^2 \quad \underline{r} \in \Sigma \tag{4.4 f}$$

wherein $SAR = \frac{\sigma(\underline{r})}{\rho(\underline{r})}\left|E(\underline{r})\right|^2$, ρ is the mass density of tissues, B_1^+ is the right hand circular polarization of the magnetic field, B_1^- is the undesired left hand polarization of the magnetic field, $B_{1,initial}^+(\underline{r}, I_n)$ is the initial spatial distribution of B_1^+ and Σ is a certain region in D which does not contain the ROI.

In problem 4.4, constraint (4.4 d) limits the SAR levels everywhere, according to the guideline dictated by international commission on non-ionizing radiation protection [30]. Constraint (4.4 e) regards the field polarization, which is enforced to remain close enough to the desired right hand one. Finally, by means of constraint (4.4 f), the square amplitude of B_1^+ must be under a specific upper bound $B_{1\,des}^+$, outside the chosen ROI. Note that in the following numerical examples, $B_{1\,des}^+$ is set equal to 1/3 of the infinite norm of the amplitude of the initial B_1^+ in the ROI [6] Finally, $\Delta\phi_i \in [0, 2\pi[$ are auxiliary variables indicating the phase shifts between the field in $\underline{r}_{t_0}$ and

$\underline{r}_{t_i}$. Note that whatever the values of the auxiliary variables $\Delta\phi_i$, constraints (4.4 a) and (4.4 b) allow to enforce equality of the field amplitude at the control points.

For any fixed frequency and $\Delta\phi_i$ value, the MRI shimming problem (4.4) is recast as the maximization of a linear function in a convex set, which corresponds to a convex programming (CP) problem. Then, the globally optimal solution of the overall optimization problem can be a posteriori determined by exploring all the different possible combinations for $\Delta\phi_i$, solving then the corresponding CP problem and finally looking into the values of the cost function or other suitable performance indicators depending on the application at hand [23], [24], [81], [82]. Alternatively, in a more convenient fashion, a nested optimization procedure where the external global optimization acts on the field phase shifts whereas the internal convex optimization acts instead on excitations can be also exploited [81].

If the optimal phase shifts were a priori known, just a single CP problem would have to be solved. Unfortunately, such an information is not generally available; hence, the computational complexity of the problem grows as the number control points increases.

To cope with this issue, a simple and physics inspired model is proposed for the total induced field in order to understand convenient and non-convenient fields interferences to be exploited in the shaping problem, thus avoiding the computational burden related to both global and enumerative optimization. In the following section, the concept underlying the proposed model method and the related mathematical formulation are described.

4.4 An auxiliary model for field amplitude shaping

In the convex procedure proposed in [22], the far field shaping problem has been tackled by looking for a superposition of many patterns focused in properly chosen given points located in the ROI. However, this procedure does

not provide any constraints outside the target area and the single focused patterns are simply added in phase without considering any possible phase shifts.

Starting from the above, a possible solution for the shaping problem is considering an auxiliary field model wherein the shaping is tackled as the superposition of single patterns focused on a number control point $\underline{r}_{t_i}$, inside the ROI. Interestingly, the combinations of these single focused bricks involve additional degrees of freedom, which are missing in [22], i.e, the phases of the field in $\underline{r}_{t_i}$. These latter, and a proper choice of the control points, will allow to control to some extent the field intensity in the ROI.

Let us consider a 2D homogeneous region of space. The field of interest in the neighborhood of the control point $\underline{r}_{t_i}$, denoted as $F_i(\underline{r})$, can be expressed in a reference system centered on $\underline{r}_{t_i}$ as a superposition of basic solutions as [46] :

$$F_i(\underline{r}) = \sum_{\ell=-\infty}^{+\infty} a_\ell J_\ell\left(k_m|\underline{r} - \underline{r}_{t_i}|\right) e^{j\ell\angle(\underline{r}-\underline{r}_{t_i})} \tag{4.5}$$

where a_ℓ is an amplitude coefficient, $J_\ell(\cdot)$ is the Bessel function of order ℓ, k_m is the wave number in the ROI and $\angle(\underline{r} - \underline{r}_{t_i})$ is the angle in polar coordinates with respect to $\underline{r}_{t_i}$, in a bidimensional system.

Whenever such a field is focused in $\underline{r}_{t_i}$, the only term which survives is the one for $\ell = 0$. As a consequence, in such a case $F_i(\underline{r})$ can be approximated, apart from the constant a_0, by means of the zero order Bessel function J_0, which is centered in the control point $\underline{r}_{t_i}$.

Then, considering the desired shaped field as a superposition of fields focused in the different control points, and assuming that, the different focused

components have all the same amplitude $a_0 = 1$[4]. Then, the overall field can be approximated as:

$$F_{aux}(\underline{r}) = J_0(k_m|\underline{r} - \underline{r}_{t_0}|) + \sum_{i=1}^{L} J_0(k_m|\underline{r} - \underline{r}_{t_i}|)e^{j\phi_i} \qquad (4.6)$$

This is true apart from a single unessential constant. In this equation the $\phi_i \in [0,2\pi[$ are auxiliary variables indicating the phase of the different Bessel functions addenda in the auxiliary model (4.5).

Note that, in problem (4.4) the magnetic field ${B_1}^+$ in $\underline{r}_{t_0}$ is assumed real by simply changing the overall phase reference. Furthermore, the variables $\Delta\phi_i$ are different from the variables ϕ_i in the auxiliary model (4.6). In fact, in model (4.6) the phase of $F_{aux}(\underline{r}_{t_0})$ can be different from zero, while in problem (4.4) the actual field ${B_1}^+$ is enforced to be real in $\underline{r}_{t_0}$. Second, and more important, variables $\Delta\phi_i$ are the phase shifts amongst the total fields ${B_1}^+$ at the control points, while variables ϕ_i are the phase shifts amongst the different Bessel functions contributions. One can determine $\Delta\phi_i$ as $\phi_i - \angle F_{aux}(\underline{r}_{t_0}, \{\phi_i\})$.

The analysis of model (4.6) can allow a relatively simple physical understanding of convenient and non-convenient Bessel-field interferences determined from $\{\phi_i\}$ values. For example, in case of just two control points, a π value of ϕ_1 would imply a null of the field $F_{aux}(\underline{r})$ at midway, so that such a value and the neighbouring ones can be discarded if a uniform amplitude field is required within the ROI. This is of course true even if in expression (4.6) no other constraints are taken into account outside the 'flat-top' zone. In fact, values of ϕ_1 implying a null of the field $F_{aux}(\underline{r})$ at midway certainly are not of interest and can be discarded in the solution of the relevant shaping problem. Interestingly, in the same two control points case and uniformity requirement, one can also analytically determine a value of ϕ_1 such that the auxiliary fields have the same amplitude at the external points and at midway. In case of

[4] By the sake of simplicity, we are herein reasoning on a 'flat top' kind of shaping. Differently weighted superpositions can be considered in other cases.

lossless media, such an optimal value is readily found as discussed in the Appendix C.

Then, although the cases with three or more control points are more and more difficult to be analysed, model (4.6) can give very useful insights about possible field interferences when varying $\{\phi_i\}$ values, and hence useful guidelines for an optimal solution of the shaping problem, as discussed below.

In fact, the auxiliary problem of determining the more convenient set of values for $\{\phi_i\}$ has a series of convenient characteristics as follow:

1. Because of the simple analytical form (4.6), one can indagate in a very fast fashion many $\{\phi_i\}$ values combinations, without solving any optimization problem or other additional procedures.

2. For the same reason, its repeated analysis also can possibly give suggestions on the selection of the control points $\underline{r}_{t_i}$;

3. Results arising from extensive investigation of model (4.6) by varying $\{\phi_i\}$ values (and eventually also the distances $|\underline{r} - \underline{r}_{t_i}|$) can be arranged into a Pareto like performance plot, giving back the more convenient ranges of the phase shifts combinations;

4. These results have a wide range of validity and can be adopted to a large series of cases, sharing the same electrical distances amongst the control points, even when k_m is an average value of the wavenumber in a non-homogeneous scenario (see *Results and Discussion* Section).

In summary, the auxiliary model (4.6) can be profitably exploited to identify convenient and non-convenient $\{\phi_i\}$ values. Once L control points are set in the ROI (step 1 in Figure 4.2), the performance parameters ($PP_1, PP_2, \ldots PP_n$) are defined depending on the application at hand (step 2 in Figure 4.2). Possible choices are the ripple and the average value in the ROI,

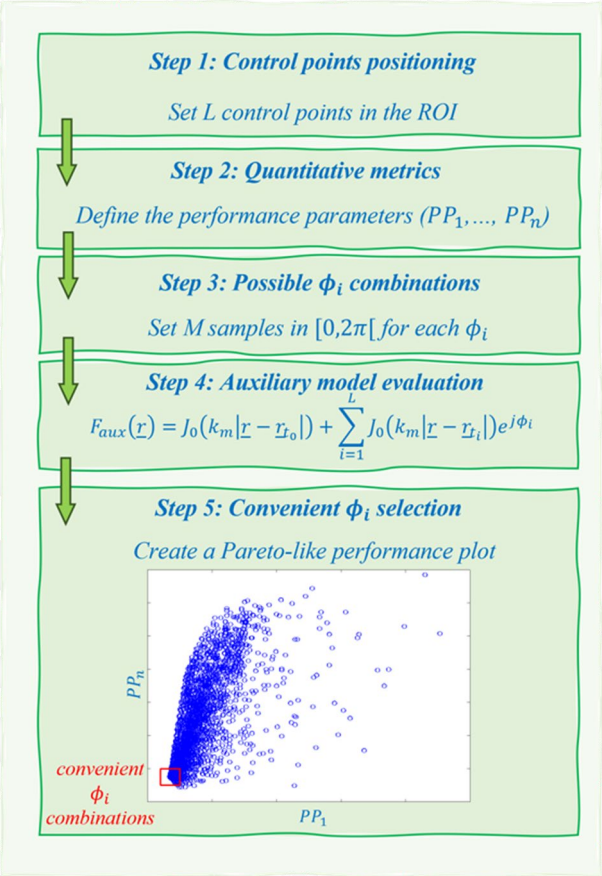

Figure 4.2 Schematic flowchart of the analysis procedure of the auxiliary model (4.6).

but different choices are indeed possible. In order to explore all possible ϕ_i values, M samples in $[0,2\pi[$ are set for each ϕ_i and $\mathrm{M}^{\mathrm{L}-1}$ combinations are considered (step 3 in Figure 4.2). Then, $F_{aux}(\underline{r})$ is evaluated by Equation (4.6) for each $\{\phi_i\}$ combination (step 4 in Figure 4.2) and, hence, those combinations corresponding to the worse performance are discarded. Also, the $\{\phi_i\}$ combinations which corresponds to the optimal values of the performance indicators PP_n are selected. To this end, it comes out to be convenient to report the indicators PP_n in a Pareto like performance plot (step 5 in Figure 4.2).

A scheme of the analysis procedure is resumed in the flowchart of Figure 4.2. At the end of the procedure, the analysis of the Pareto-like performance

plot allows to easily identify the $\{\phi_i\}$ combinations to be discarded as well as the more convenient ones. For example, if performance parameters PP_n are defined in such a way that better performance are obtained when they assume low values, the low-left corner points correspond to the more convenient $\{\phi_i\}$ combinations (see f.i. the red box in Figure 4.2).

As far as step 1 is concerned, it is important to note that the overall strategy amounts to find some appropriate interferences amongst different elementary bricks, herein given by Bessel functions. Hence, in order to have eventually significant interferences, the distance amongst two control points has to be such that the elementary bricks are not too small in the ROI, or at least along the line joining the two points. On the other hand, very small distances among the control points also do not have sense, as the control points would be redundant and this circumstance would just increase the computational burden, without adding useful information. As a rule of thumb deriving from an extensive numerical analysis, distances belonging to the interval $[0.25,0.5]\lambda_b$ are suggested. As a second possibly useful comment, note that within this interval, the simplicity of the proposed auxiliary model allows one also to understand what is the best location distance. In fact, one could select the distance implying a minimum RSD and a maximum field amplitude, according to the analysis resumed in Figure 4.2. Finally, an additional criterion for choosing the position of the control points is the need of covering in a possibly uniform fashion the region of interest.

The analysis shown in the Figure 4.2, allows two effective possibilities for the solution of the relevant shaping problem. First, understanding the optimal field interferences also implies achieving convenient field distributions within the ROI. Then, in order to solve the actual problem of determining the complex excitations of the primary sources, one can simply minimize the misfit between the actual field distribution (4.1) and the reference target distribution(s) as determined from the above analysis. Notably, this is indeed a field synthesis problem which can be easily solved by the minimization of a quadratic functional.

Second, once one has gained awareness of convenient and non-convenient interferences, one can take advantage of such a knowledge within a constrained power optimization framework. In particular, as it will be discussed in detail in the numerical analysis in Subsection 4.5, the outcomes of model (4.6) can play a pivotal role in *multi control points*-based approaches, as it allows time and memory saving in the overall optimization, without affecting the final performance.

4.5 Analysis of the auxiliary field model

In order to give a better insight into the auxiliary model (4.6), in this section a numerical analysis is reported in the simple case of homogeneous medium. In particular, the analysis procedure in Figure 4.2 is performed. As far as the check of the usefulness of this analysis in a relevant actual shaping problem is concerned, the reader is deferred to Section 4.6, wherein application to the challenging MRI shimming case is considered.

In the following two subsections, a square domain of side $L = 0.76\lambda_b$ is considered, discretized into $N_x \times N_y$ small cells, with $N_x = N_y = 80$, where λ_b is the wavelength in a homogenous medium with relative permittivity of 53 and electrical conductivity 0.15. The working frequency is 128MHz.

As expected, expression (4.6) tuns out to be exact for the case of a single control point, i.e. for the focusing problem. More interestingly, the Bessel function of zero order comes out to be quite accurate to approximate the spatial distribution of the focused field in a neighborhood of the control point even in the case of a non-homogeneous scenario.

In the two subsections which follow the analysis of model (4.6) for the cases of two and four control points is discussed.

Case study 1: two control points

The scenario under test is depicted in Figure 4.3(a). The control points are located at a distance $d = 0.27\lambda_b$. The midpoint is at (0,0) m. The ROI is represented by the yellow ellipse in Figure 4.3(a).

According to step 3 in Figure 4.2, M=20 values of ϕ_1 have been uniformly sampled in $[0,2\pi[$. The spatial distributions of the auxiliary field intensity obtained by considering 11 values of ϕ_1 evenly spaced in $[0,\pi]$ are shown in Figure 4.3. The same results are obtained in case of $\phi_1 \in]\pi,2\pi[$. Note that, by virtue of the simple analytical form of (4.6), its evaluation for different ϕ_1 values is immediate. As expected, when ϕ_1 approaches π a disruptive interference arises between the two Bessel functions. Instead, for phase shifts near to 0 (or 2π), a satisfactory tradeoff between amplitude and uniformity is obtained. Note that these results are also in agreement with the examples in Figure 4.3 of paper [24].

In order to evaluate in a systematic way the optimal phase shift ϕ_1 able to both ensure a uniform and intense spatial distribution of the field intensity, we consider two quantitative synthetic performance indicators. In particular, we consider the average value of the field intensity F_{av} and the relative standard deviation of the amplitude (RSD), defined as:

$$RSD = \frac{std\{|F|\}}{mean\{|F|\}} \tag{4.7}$$

being $std\{\cdot\}$ and $mean\{\cdot\}$ respectively the standard deviation and the mean. Both indicators are evaluated within the ROI. Performance is easily evaluated in case of different distances between the control points. In particular, in Figures 4.3(m)-(o), we plot the RSD parameter versus the reciprocal of F_{av} in case $d = 0.26\lambda_b$, $d = 0.33\lambda_b$ and $d = 0.4\lambda_b$. Note that distances higher than $0.5\lambda_b$ are not suitable as they do not allow an accurate control of the field intensity.

According to the proposed procedure, $\phi_1 \in [0,\pi/3]$ are the optimal phase shifts leading to an appropriate interference while the ones in proximity of π can be discarded. Then, the corresponding field amplitude distributions (shown in Figure 4.3) are the ideal ones to be eventually considered within a field synthesis optimization procedure.

Case study 2: four control points

The scenario under test is depicted in Figures 4.4(a). The control points are located at distances of about $d_{02} = 0.42\lambda_b$ and $d_{13} = 0.32\lambda_b$. Both midpoints are at (0,0) m, while the reference point is the one in $(0,0.21\lambda_b)$. The ROI is represented by the yellow area in Figure 4.4(a).

According to step 3 in Figure 4.2, in order to explore all the possible combinations of phase shifts, M=20 values for each ϕ_i have been uniformly sampled in the interval $[0,2\pi[$. Then, the total number of possible combinations is $M^{L-1} = 8000$.

The RSD parameter versus the reciprocal of F_{av} is plotted in Figure 4.4(e). Each circle represents a pair of values (RSD, $1/F_{av}$) corresponding to one of the 8000 phase shifts combinations. As in case of two control points, convenient combinations exist which corresponds to the circles in the region close to the origin of the coordinates system. We consider the region such that $RSD \leq 0.15$ and $1/F_{av} \leq 3.8$. Then, the number of convenient combinations to be eventually considered for the problem at hand is drastically reduced to 216.

A combination ensuring a good tradeoff is the combination (0,0,0) and the corresponding auxiliary field distribution is shown in Figure 4.4(b). Figure 4.4(c) shows instead the auxiliary field distribution corresponding to a phase shifts combination giving a minimum RSD. Finally, Figure 4.4(d) shows the auxiliary field distribution corresponding to a phase shifts combination giving a maximum RSD.

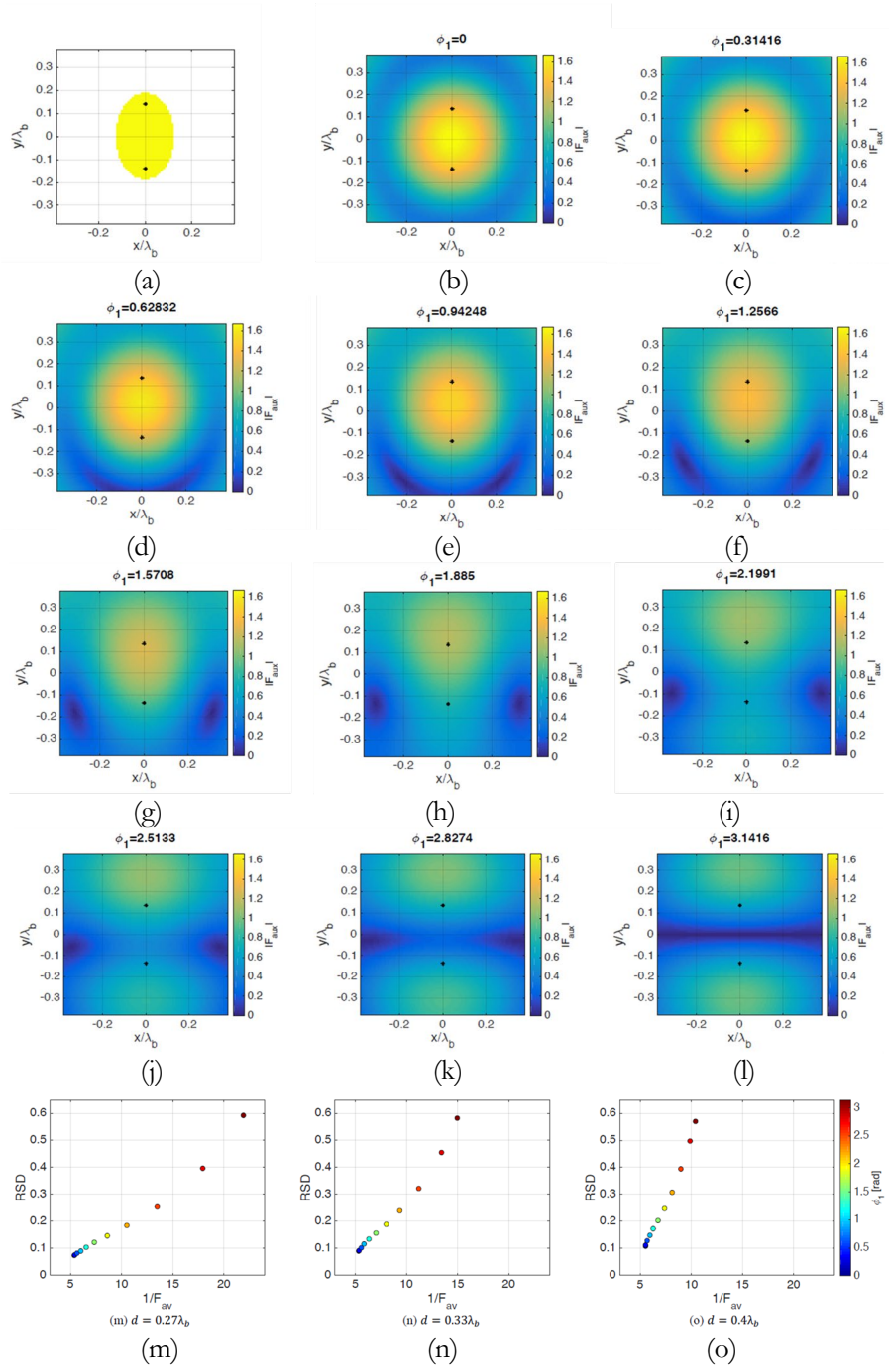

Figure 4.3: Analysis of the auxiliary field model. CASE STUDY 1. (a) Scenario under test. The ROI is the yellow area, while the control points are superimposed as black points at distance $\boldsymbol{d = 0.27\lambda_b}$. (b)-(l) Spatial amplitude distributions of the auxiliary field model for different values of phase shifts in $\boldsymbol{[0, \pi]}$ for $\boldsymbol{d = 0.27\lambda_b}$. RSD versus the reciprocal of $\boldsymbol{F_{av}}$ for (m) $\boldsymbol{d = 0.27\lambda_b}$, (n) $\boldsymbol{d = 0.33\lambda_b}$ and (o) $\boldsymbol{d = 0.4\lambda_b}$. Each circle represents a pair of values (RSD, $\boldsymbol{1/F_{av}}$) corresponding to a given phase shift in the interval $\boldsymbol{[0, \pi]}$.

In the following Section, the effectiveness of the convenient phase shifts

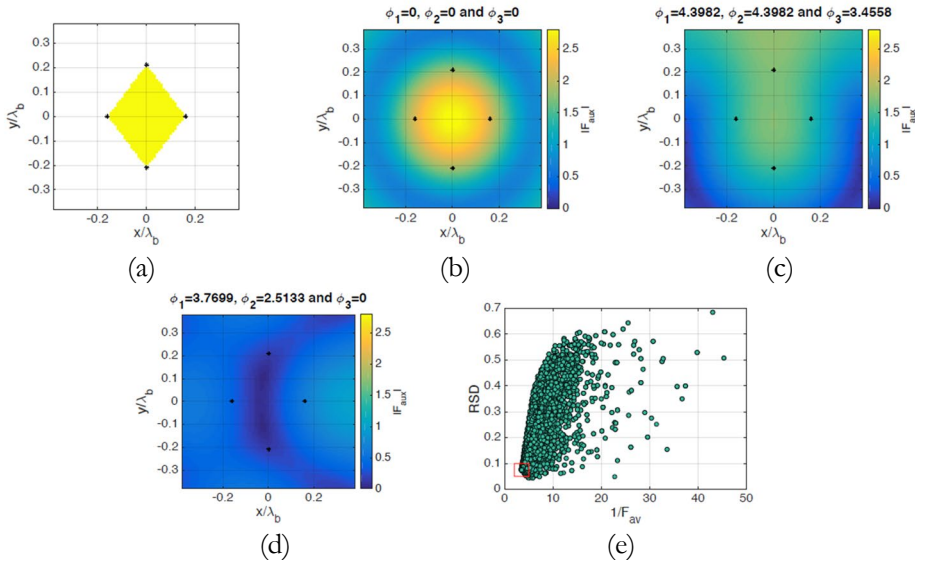

Figure 4.4: Analysis of the auxiliary field model. CASE STUDY 2. *(*a) Scenario under test. The ROI is the yellow area, while the control points are superimposed as black points at distances $\mathbf{d_{01} = 0.42\lambda_b}$ and $\mathbf{d_{23} = 0.32\lambda_b}$. (b) Spatial amplitude distribution of the auxiliary field model in case of good tradeoff between RSD and maximum auxiliary field intensity in the ROI. (c) Spatial amplitude distribution of the auxiliary field model in case of minimum RSD. (d) Spatial amplitude distribution of the auxiliary field model in case of maximum RSD. (e) RSD versus the reciprocal of $\mathbf{F_{av}}$. Each green circle represents a pair of values (RSD, $\mathbf{1/F_{av}}$) corresponding to a given combination of phase shifts. The red box delimits the region corresponding to the best tradeoff between minimum RSD and maximum $\boldsymbol{F_{av}}$.

suggested in case of two and four control points by the above analysis based on the auxiliary field model (4.6) are tested in the relevant case of MRI shimming.

4.6 Application to MRI Shimming

A transverse slice has been considered and enclosed within a square domain D, discretized as in Section 4.5. In the second phantom, the head has been instead modeled as a homogeneous medium with electrical properties set equal to the average value of the ones of the brain tissues, that is with relative permittivity of 53 and electrical conductivity 0.15.

Figures 4.5(a)-(b) and 4.5(e)-(f) depict respectively the relative permittivity and the electrical conductivity distributions of both scenarios.

In order to simulate an MRI scanner, the birdcage structure has been schematized as a circular antenna array of radius $0.2m$, in accordance with the realistic size of common birdcage coil adopted in clinic and located around the head phantom with 16 antennas evenly spaced (see Figure 4.5(j)). Air has been assumed to be the background medium. For comparison, the coefficients I_{n_0} corresponding to the standard design of the birdcage coil configuration have been considered. Finally, the considered Larmor frequency is 128 MHz, which corresponds to a static field $B_0 = 3T$.

In Figures 4.5(c) and (d) and 4.5(g) and (h), the spatial distributions of the B_1^+ field and the SAR corresponding to the standard coil configuration are shown, respectively, for the two head phantoms, while in Figure 4.5(i) the magnitude and phase of the standard array excitation coefficients [I_{n_0}] are reported.

As first step, a single control point located at (0, 0.029 m) has been considered and the corresponding focusing problem has been solved. In both cases, for the evaluation of the argument of the Bessel function in the field approximation (4.6), the average of both the relative permittivity and electrical conductivity have been considered, i.e. about 53 and 0.15, respectively. The amplitudes and phases of the Bessel function and the actual focused magnetic field are shown in Figure 4.6 for both head phantoms. As it can be seen, the spatial distribution of B_1^+ can be well approximated in the head support by the Bessel function of zero order, which means that consideration of just the first term of expansion (4.5) is suitable for understanding expected behaviors in term of $\{\phi_i\}$ (and hence $\{\Delta\phi_i\}$). Notably, the auxiliary model (4.6) can still be used notwithstanding the inhomogeneity of the scenario.

Case study 1: two control points

The control points have been located as in Figure 4.3(a) at $d = 0.27\lambda_m$, where λ_m is the wavelength refers to the mean of the brain electrical properties. The chosen ROI is represented by the yellow ellipse in Figure 4.47(a) and .8(a), respectively for the homogeneous and realistic head phantoms.

In order to check the usefulness of the analysis reported in Section 4.5, all the M=20 values of the phase shift $\Delta\phi_1$ have been considered in the solution of problem (4.4). In case of homogeneous head phantoms, the spatial distributions of the B_1^+ field corresponding to the first 11 $\Delta\phi_1$ values are shown in Figures 4.7(b)-(l) and 4.8(b)-(l). According to Section 4.5, just a few $\Delta\phi_1$ values, evaluated as $\phi_1 - \angle F_{aux}(\underline{r}_{t_0}, \phi_1)$, allow to ensure both a uniform and maximum spatial distribution of the field intensity.

To better handle the underlying trade-off, the RSD parameters versus the reciprocals of B_{av}, i.e. the average value of the B_1^+ intensity, are shown in Figures 4.7(m) and 8(m)[5]. Notably, the same qualitative behavior as in Figure 4.3(m) is obtained. Then, the proposed off-line analysis of the auxiliary model can be assumed to effectively predict the convenient and the non-convenient field interferences, even if the biological scenario under test is significantly heterogeneous.

As expected, this procedure gives significant advantages in terms of computational complexity, as just 4 CP problems need to be solved by exploiting the outcomes of the auxiliary model analysis, whereas the

[5] In such graphs, the last 11 explementary angles within $]\pi, 2\pi[$ are also shown as they can have slightly different performance due to the heterogeneity of the scenario under test.

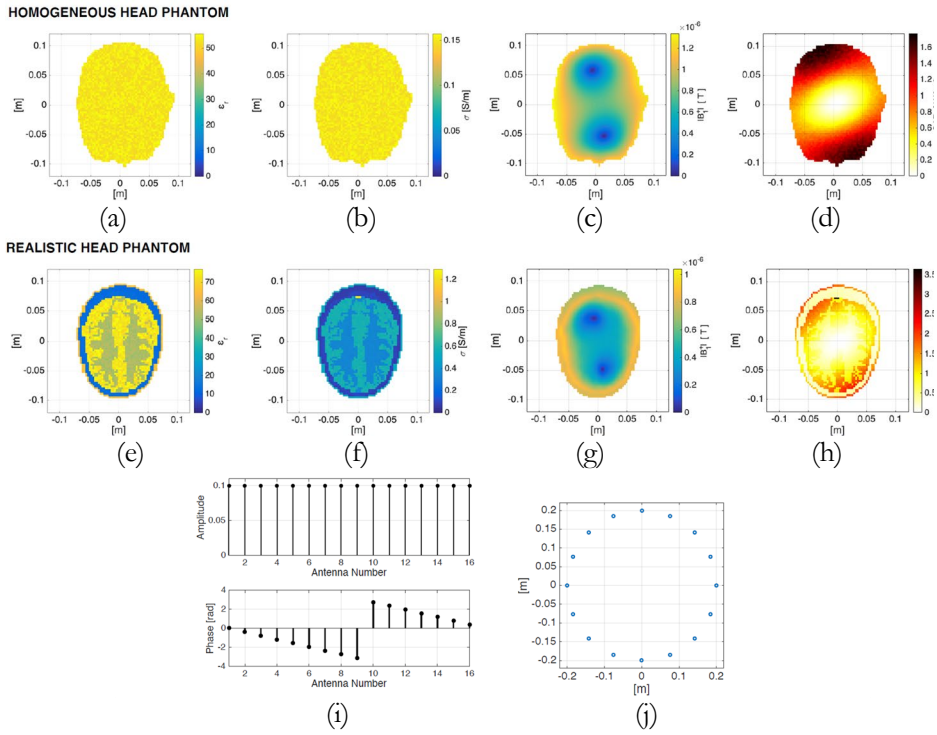

Figure 4.5: MRI shimming against 2D head phantoms.: relative permittivity (a),(e) and electrical conductivity (b),(f) maps. Spatial distributions of the amplitude of the magnetic field $\boldsymbol{B_1^+}$ [T] (c),(g) and SAR [W/kg] (d),(h) corresponding to a standard coil configuration. Amplitude and phase (i) of the standard excitation coefficients. (j) Positions of the antennas of the circular array schematizing the birdcage coil.

enumerative solution of problem (4.4) requires the solution of 20 CP problems. It is important to note that the time saving is anyway much larger than the approximatively one order of magnitude, from 20 to 4 CP problems. In fact, some of the original 20 optimization problems and specifically, those corresponding to the non-convenient $\Delta\phi_1$ values are severely ill-conditioned, so that their solution can be very slow. Obviously, computational advantages are more and more pronounced as M and L increase (see next case) and in 3D geometry.

Please note that the RSD of ${B_1}^+$ corresponding to the standard choice of the excitations (see [6]) is 0.33, while by means of the proposed shimming

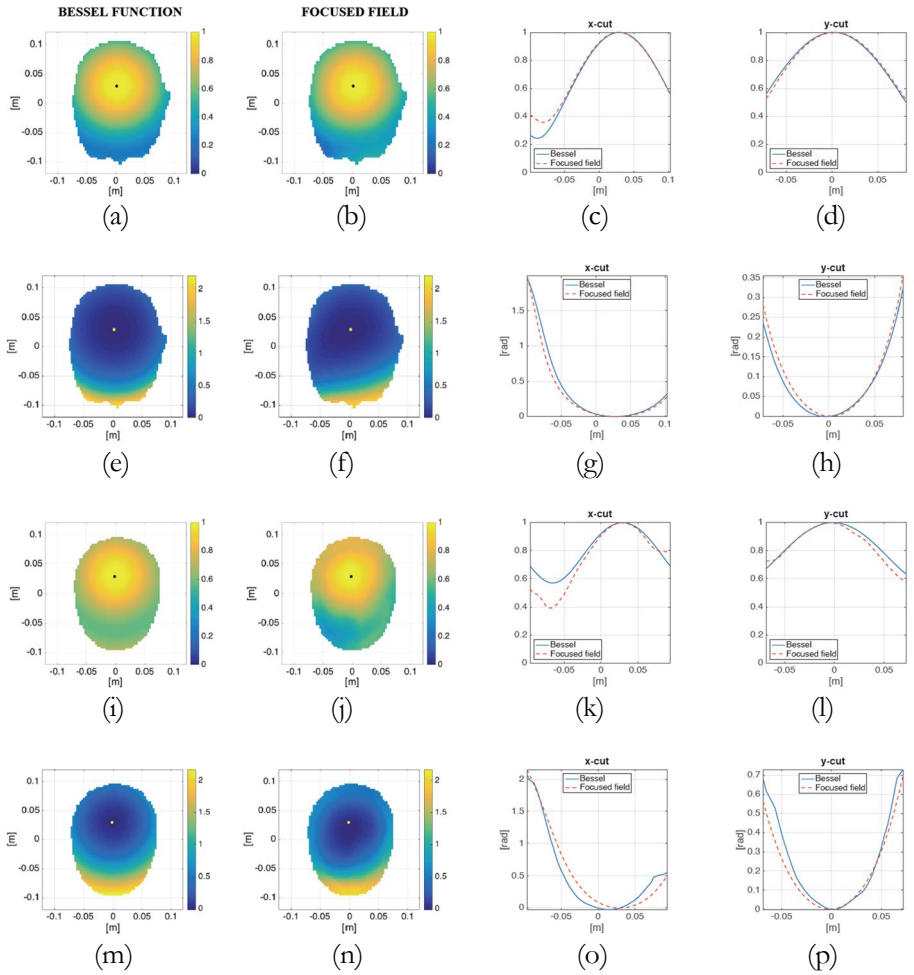

Figure 4.6: MRI shimming against 2D head phantoms. (a)-(h) Homogeneous and (i)-(p) realistic head phantoms. Amplitudes distributions of (a),(i) the Bessel function of zero order and (b),(j) the field focused via problem (5) in case of a single control point located in (0, 0.029 m). Corresponding cut views along (c),(k) x-axis at y=0.029 and (d),(l) y-axis at x=0 (zoomed in on the brain support). Phase distributions of (e),(m) the Bessel function of zero order and (f),(n) the field focused via problem (5). Corresponding cut views along (g),(o) x-axis at y=0.029 and (h),(p) y-axis at x=0 (zoomed in on the brain support). The continuous lines correspond to the Bessel function of zero order, while the dashed lines correspond to the focused field.

procedure, the optimal phase shift can ensure an RSD much lower than 0.1. This means that a more uniform B_1^+ field has been now obtained respect to the standard distribution. This final RSD is the same as the one obtained by performing an enumerative optimization (results in[5] of Publication List).

The optimal phase shift for the considered choice of control points correspond to $\Delta\phi_1 \sim 0$ (see Figures 4.7 and 8) as it also ensures the best field amplitude distribution. Figures 4.7(n) and 8(n) give the corresponding optimal amplitudes and phase of the complex excitations I_n for both the homogenous

and the realistic head phantoms. Note that the procedure also allows a

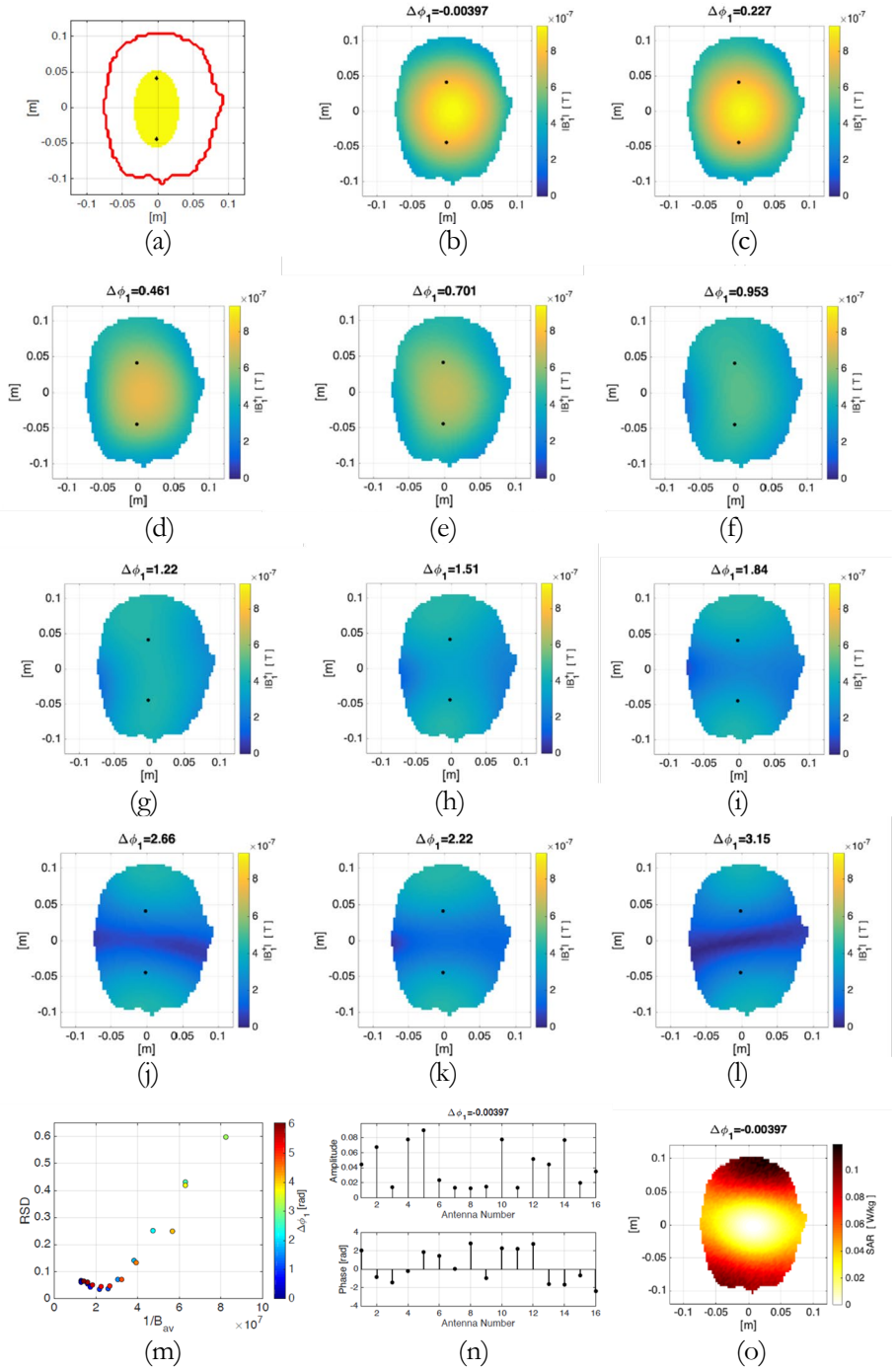

Figure 4.7: MRI shimming against 2D head phantoms. CASE STUDY 1: Homogeneous head phantom. The ROI is the yellow area (a), while the control points are superimposed as black points. (b)-(l) Spatial amplitude distributions of the magnetic field $\boldsymbol{B_1^+}$ [T] for different value of phase shifts in $\boldsymbol{[0,\pi]}$. (m) RSD versus the reciprocal of $\boldsymbol{B_{av}}$ [T]. Each circle represents a pair of values (RSD, $\boldsymbol{1/B_{av}}$) corresponding to a given phase shift. The different colors correspond to a value of $\boldsymbol{\Delta\phi_1}$. (n) Amplitude and phase of the optimal excitation coefficients and (o) SAR [W/kg] spatial distribution corresponding to the optimal $\boldsymbol{\Delta\phi_1}$.

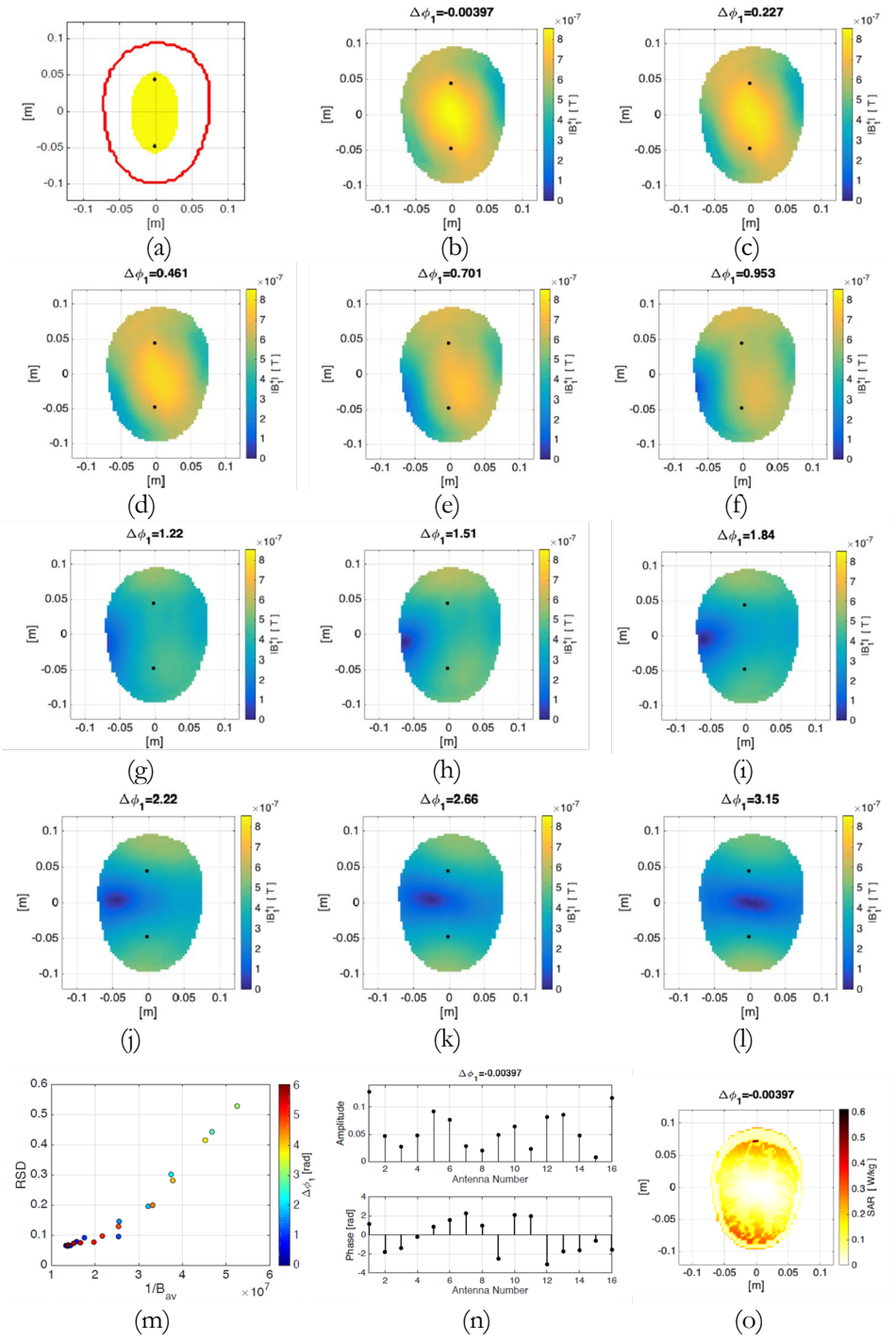

Figure 4.8: MRI shimming against 2D head phantoms. CASE STUDY 1: Realistic head phantom. The ROI is the yellow area (a), while the control points are superimposed as black points. (b)-(l) Spatial amplitude distributions of the magnetic field $\boldsymbol{B_1^+}$ [T] for different value of phase shifts in $\boldsymbol{[0,\pi]}$. (m) RSD versus the reciprocal of $\boldsymbol{B_{av}}$ [T]. Each circle represents a pair of values (RSD, $\boldsymbol{1/B_{av}}$) corresponding to a given phase shift. The different colors correspond to a value of $\boldsymbol{\Delta\phi_1}$. (n) Amplitude and phase of the optimal excitation coefficients and (o) SAR [W/kg] spatial distribution corresponding to the optimal $\boldsymbol{\Delta\phi_1}$.

satisfactory control of SAR levels into the ROI, as shown in Figures 4.7(o) and

8(o).

Case study 2: four control points

The control points have been located as in Figure 4.4(a) at a distance of $d_{02} = 0.42\lambda_m$ and $d_{13} = 0.32\lambda_m$ (see Figures 4.9(a) and 10(a)). Both midpoints are at (0,0) m. As a consequence, the already available analysis of subsection 4.5 can be applied. If all the possible combinations were considered for problem (4.4), with M=20 values for each ϕ_i, 8000 convex problems should be solved, which means a very expensive and time-consuming procedure. However, results in Subsection have shown that some combinations are not convenient for the application at hand. Then, in the following, we have considered only those combinations that ensure a good compromise between uniform spatial distribution and maximum of the field, that are the 216 combinations in the region $RSD \leq 0.15$ and $1/F_{av} \leq 3.8$ in Figure 4.4(e).

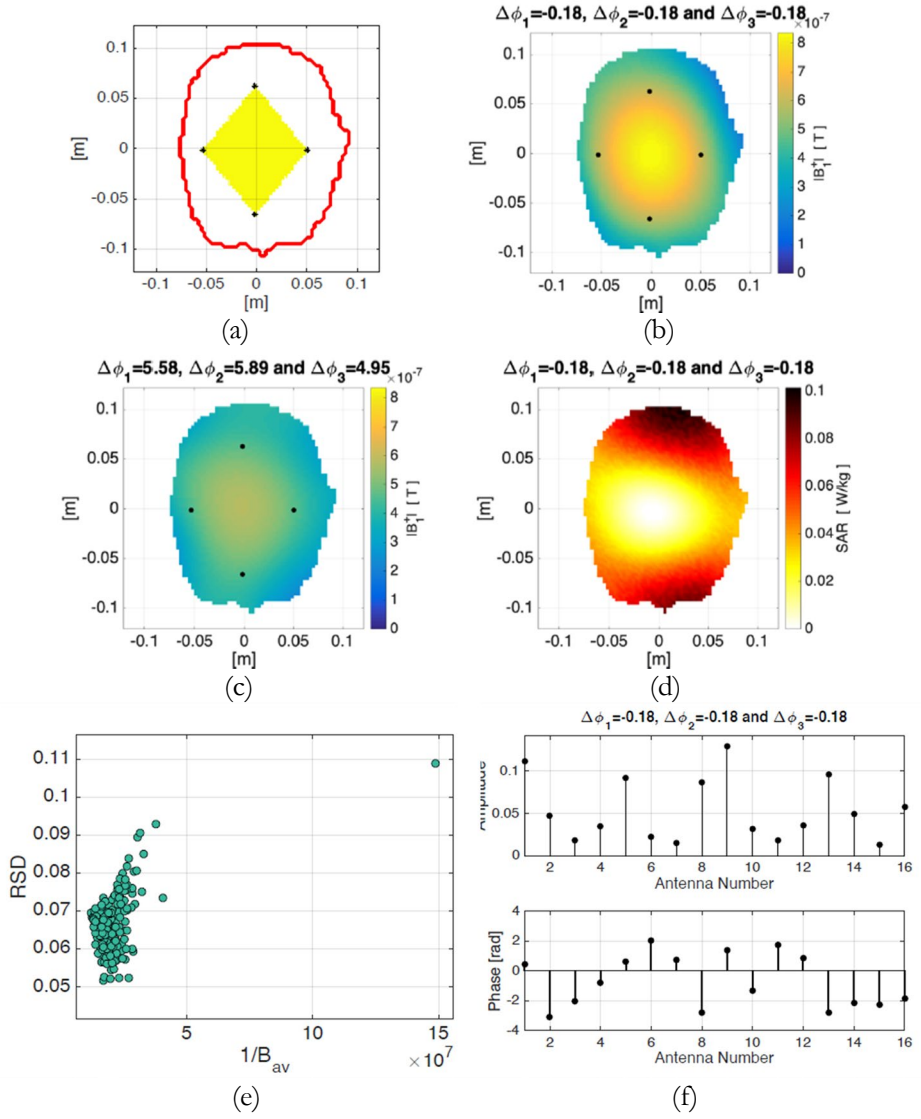

Figure 4.9: MRI shimming against 2D head phantoms. CASE STUDY 2: Homogeneous head phantom. The ROI is the yellow area (a), while the control points are superimposed as black points. (b) Spatial amplitude distribution of the magnetic field $\boldsymbol{B_1^+}$distributions [T] in case of good tradeoff between RSD and maximum field intensity in the ROI. (c) Spatial distribution of the field intensity distributions in case of minimum RSD. (d) SAR [W/kg] spatial distribution corresponding to (b). (e) RSD versus the reciprocal of $\boldsymbol{B_{av}}$ [T]. Each green circle represents a pair of values (RSD, $\boldsymbol{1/B_{av}}$) corresponding to a given combination of phase shifts. (f) Amplitude and phase of the optimal excitation coefficients corresponding to (b).

The RSD parameters versus the reciprocals of B_{av} is shown in Figures 4.9(e) and 10(e). The optimal phase shift combinations are $\Delta\phi_1 = -0.18$, $\Delta\phi_2 = -0.18$ and $\Delta\phi_3 = -0.18$ and $\Delta\phi_1 = -0.263$, $\Delta\phi_2 = 5.71$ and

$\Delta\phi_3 = -0.263$ respectively for the homogeneous and realistic phantoms. Indeed, they ensure the best field distributions. The optimal field distributions are shown in Figures 4.9(b) and 10(b), while the ones corresponding to the minimum RSD are reported in Figures 4.9(c) and 10(c). Note that the RSD of B_1^+ evaluated for the standard choice of excitations [20] is 0.34, while, by means of the proposed shimming procedure, the RSD is lower than 0.08. This final RSD is the same as to the one obtained by performing an enumerative optimization as in [24], so that also in this case the achieved time saving does not imply a worsening of performances.

Figures 4.9(f) and 10(f) give the corresponding optimal amplitudes and phases of the complex excitations I_n of the N conductors, while the reached SAR levels into the brain are shown in Figures 4.9(d) and 10(d).

The above results, and other cases not shown herein for the sake of brevity, demonstrate the feasibility and the accuracy of the proposed auxiliary model in predicting the field interferences within the ROI and the optimal phase shifts combinations to be used in the solution of the original problem (4.4). Moreover, the off-line analysis of the auxiliary model (4.6) has allowed to obtain the optimal I_n without the solution of a very high number of CP problems and, thus, with a reduced computational burden related to the *multi-*

	# CP problems		Computational time	
L	2	4	2	4
proposed approach	4	216	~3 min	~5 h
enumerative approach	20	8000	~26 min	~570 h

Table 4: Advantages in term of computational burder: number of CP problems to be solved and computational time.

control points based approaches. As a matter of fact, in case of four control points

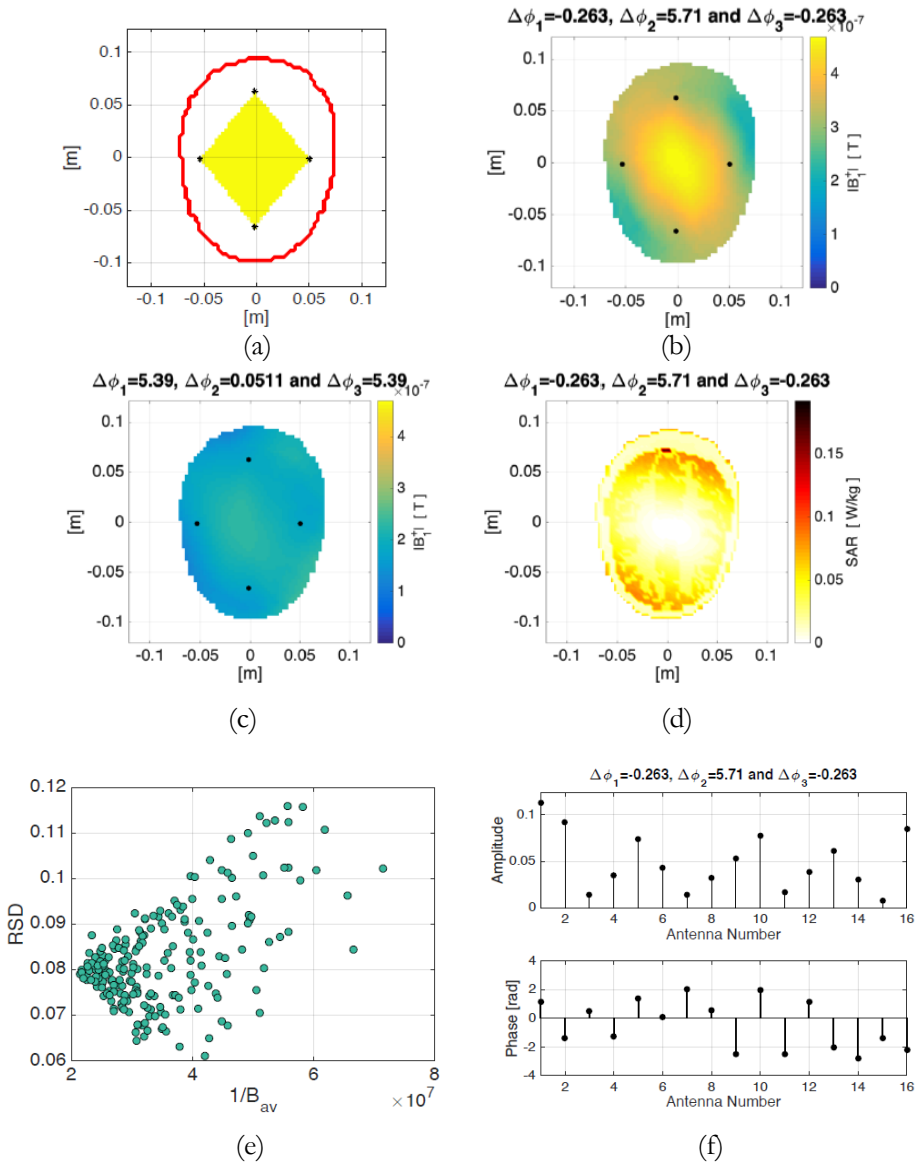

Figure 4.10: MRI shimming against 2D head phantoms. CASE STUDY 2: Realistic head phantom. The ROI is the yellow area (a), while the control points are superimposed as black points. (b) Spatial amplitude distribution of the magnetic field $\boldsymbol{B_1^+}$ distributions [T] in case of good tradeoff between RSD and maximum field intensity in the ROI. (c) Spatial distribution of the field intensity distributions in case of minimum RSD. (d) SAR [W/kg] spatial distribution corresponding to (b). (e) RSD versus the reciprocal of $\boldsymbol{B_{av}}$ [T]. Each green circle represents a pair of values (RSD, $\boldsymbol{1/B_{av}}$) corresponding to a given combination of phase shifts. (f) Amplitude and phase of the optimal excitation coefficients corresponding to (b).

we have a reduction factor of about 40 of the number of CP problems, resulting in an even larger factor in terms of overall computational time. In order to emphasize such reduction, two metrics are adopted and reported in Table 4, that are the numbers of involved CP problems and the computational time for

the two cases wherein the proposed auxiliary model or the standard enumerative strategy in [23] [24] are adopted, respectively.

In summary, the numerical analysis against a realistic head phantom has outlined that the proposed auxiliary model can be effective also in case of non-homogenous medium. Moreover, consideration of a set of optimal phase shifts combinations based on the proposed auxiliary model, rather than selecting a unique optimal phase shift combination, has to be preferred especially in case of a number of control points higher than 2. In fact, such a choice allows to compensate possible small variations of the field distribution due to the heterogeneous scenario under test, and to better tailor the results to the application at hand.

5 Conclusion and possible future development

In this Thesis, new methodologies for electromagnetic recovery and synthesis problems applied to Magnetic Resonance Imaging have been presented.

The issue of recovering EPs from a given electric or magnetic intensities of an electromagnetic field is crucial in many biomedical applications (i.e. dosimetry, hyperthermia treatment, diagnosis and so on). The most used strategies require the solution of an inverse scattering problem. To address such a kind of problem, it is important to develop proper inversion strategies, able to tackle in a reliable way the underlying inverse scattering problem. In this respect, in this thesis new inversion methods, based on learning strategies, for the characterization of the dielectric properties of tissues have been developed.

On the other hand, the optimal synthesis of array antennas warranted attention in fields that were concerned with human health and safety, and also in RF Shimming. In this case, one needs to develop a shaping strategy which can ensure some uniformity of the field intensity within the anatomical region to be investigated, while keeping under control the SAR level. In this respect, a new field shaping strategy has been proposed for active RF shimming, which exploits some control points in the ROI and assume as degree of freedom the phase shifts among the field in such points. Moreover, this procedure has been further optimized through the development and the application of an auxiliary field model for the smart choice of the more useful fields interferences to be exploited in the shaping problem.

More in detail, the contributions of the Thesis can be summarized as it follows.

1) the problem of retrieving the EPs starting from the measurements of the RF field collected inside an MRI scanner has been treated as an inverse scattering problem (ISP). Generally, ISPs can be addressed using either physics-based iterative techniques or learning-based approaches. The first category,

which is the mostly used, is typically computationally expensive due to its iterative nature. On the other hand, learning approaches provide a real-time solution, although incorporating domain knowledge is difficult. In this respect, in this thesis two different approaches able to address this issue have been presented. The first proposed technique exploits the Supervised Descent Method (SDM), the second one instead is based on a cascade of multi-layer CNNs to perform the model update. Unlike most of the learning approaches that lack physical information provided by the forward model, the proposed strategies can be classified as physics-assisted learning techniques. Both techniques aim at making the EPs reconstruction process as reliable as possible, alleviating the problem of 'local minima' as well as by reducing the computational time need for all the process. However, these methods could have issues with generalization, therefore the training datasets need to be carefully designed according to the task at hand.

2) the array antenna synthesis problem for RF Shimming has been addressed as a field amplitude shaping, which consists in determining the optimal set of complex excitations of an arbitrary fixed-geometry arrays generating the desired field distribution. By taking advantage from `mt-FOCO', in the Thesis, a novel synthesis procedure for active RF shimming has been proposed, able to take contemporaneously into account all constraints regarding polarization, homogeneity and strength of the B1 Field and to enforce SAR limits into the desired treated region. Furthermore, a simple auxiliary and physics inspired model, which allows a relatively simple physical understanding of convenient and non-convenient fields interferences to be exploited in the shaping problem, and hence a drastic reduction of the computational burden related to its solution via optimization procedure has been proposed. However, this model does not exploit all the available degrees of freedom, f.i. the amplitude differences between the Bessel beams.

Both activities have been particularized and assessed for the case of a realistic 2D brain models.

Moreover, they allow to devise a series of possible developments.

First, in order to improve the learning capabilities of the proposed 3,CNNs-EPT, a larger training dataset with more heterogeneous data can be used. However, this could have the disadvantage of increasing the cost and time required in the training phase. A further step forward will be to validate the procedure in case of a 3D scenario and in case of realistic data. CNNs are not the only possible architecture that can be used to resolve ISPs. RNNs are other common structures often used. The real advantage of these kind of networks is that they have a memory state, which allows it to be used in iterative procedures. In this regard, a future work involves the use of an RNN that mimics the iterative process underlying the proposed 3,CNNs-EPT.

As far as the second contributions, the physics inspired model, proposed in Chapter 4, allows to understand the possible spatial field distributions by analyzing the interferences between canonical solutions for the induced total field in the ROI, that are zero order Bessel functions. Such analysis allows to discard the non-convenient interferences depending on the application at hand. The usefulness of the proposed auxiliary model has been tested in the case of MRI shimming, but it also relevant in several applications. In fact, future work will be devoted at testing the procedure in applications, such as hyperthermia treatment planning and array synthesis for telecommunications, as well as to cases where the overall field intensity rather than the amplitude of a single component is of interest. Furthermore, the extension of the rationale underlying the proposed auxiliary model will be addressed in the more challenging 3D vectorial scenario, wherein its features would become even more attractive. Another possible investigation that needs attention is related to the fact that adopted multi control points-based approaches do not exploit all the available degrees of freedom, as they only consider different phase shifts but assume the same amplitudes among the single field patterns. In this respect, the idea of combining focused patterns by means of complex coefficients is in progress. This means that amplitude differences are also admitted in the linear combination. In such a way all the available degrees of freedom are exploited. This circumstance can play a key role for field intensity shaping, especially in

case of lossy and highly heterogeneous scenarios as the ones considered in the Thesis

Appendix A

This Appendix is aimed at giving some electromagnetic concepts and specially some basics about the inverse scattering problem and the related most difficult challenges.

A.1 Inverse scattering problems: basics

The e*lectromagnetic scattering problem* is a phenomenon that occurs when an electromagnetic field, propagating within a certain region of space, encounters obstacles generating a diffuse field [14] as we can see in Figure A.1:

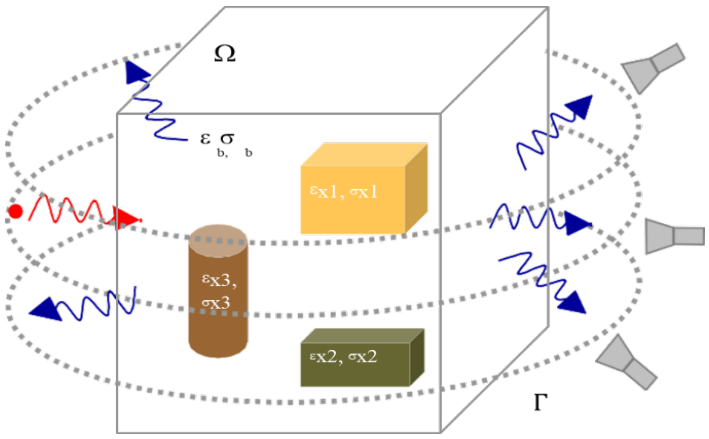

Figure A.1: Sketch of the scattering phenomenon

Therefore, the field radiated by the sources propagates in space, encounters obstacles and undergoes perturbations. The field that will be created in the region of investigation will therefore be given by the sum of two contributions, the first is an unperturbed field given by the superposition of the incident field present in the region of space in which we have no obstacles, the second is a field perturbed, which takes the name of field scattered, due to the presence of these obstacles. The scattered field will depend on the object itself which is its source. This is because when the incident field meets the obstacles it generates currents on them, called *induced currents*, which become sources of another field which is the *scattered field*, whose properties strictly depend on the electromagnetic characteristics of the scatterers.

This electromagnetic scattering problem has two sub-problems, in fact an *inverse problem* [14] presupposes the existence of another problem (which is called *direct problem*) to which the inverse problem is closely related. Therefore, it can be said that two problems are one the inverse of the other when the formulation of one necessarily involves the other.

The direct problem, from a physical process, can be described as follows: *given the model k and the effect y, trace the cause x;* conversely the inverse problem consists in: *assigning the cause x and the effect y, going back and calculating the model k.*

So, if you want to predict the effect of a known cause then you can say that you want to solve a direct problem. Conversely, going back to the cause from the knowledge of the effect, or determining the value of certain physical parameters of the cause, are defined as inverse problems. In principle, by sending known incident fields and by measuring the fields scattered by a generic obstacle(s) present in the region of interest (ROI), it is possible to obtain electromagnetic information and not on this obstacle. The purpose of the inverse problem is, in fact, to estimate the electromagnetic properties (electrical conductivity σ, magnetic permeability μ and dielectric permittivity ε) of a complex material starting from the measurements of the scattered field by it.

In the literature, the inverse problem is the most fascinated one because successful solution approaches to such kind of approaches can be helpful in very many different applications such as biomedical imaging, subsurface prospecting and non-destructive testing [9] [10] Furthermore, due to its non-linearity and ill-posedness, it is very challenging, and a lot of work has been done from many researchers and scientists in developing more and more efficient numerical methods and computational techniques.

The mathematical formulation of the inverse scattering problem is given in the Subsection which follows.

A.2 Problem statement

Let us consider the two-dimensional scalar (TM polarized fields) inverse scattering problem, with a bounded, simply connected, inhomogeneous object domain D in an unbounded homogeneous background medium $(\varepsilon_b, \sigma_b, \mu_0)$. The investigated domain D, delimited by the Γ curve, embeds the transverse

section Σ of the scatterer under examination $(\varepsilon_s, \sigma_s, \mu_0)$. Let the z axis be the direction of invariance of the object(s).

We refer to the so-called multi-view multi-static configuration where for each antenna that acts as a transmitter, all the others act as receivers, and all antennas alternately act as a transmitter.

The equations governing the scattering phenomenon for the geometry at hand for the generic v-th incident field can be expressed in an integral form as it follows[8]

$$u_{tot}(\underline{r}) = u_{inc}(\underline{r}) + k_b^2 \int_D G(\underline{r}, \underline{r}')W(\underline{r}')d\underline{r}' \triangleq$$

$$\triangleq u_{inc} + A_D[W(\underline{r}')] \qquad \text{con } \underline{r} \in \text{D (A. 1)}$$

$$u_s(\underline{r}) = u_{tot}(\underline{r}) - u_{inc}(\underline{r}) =$$

$$= k_b^2 \int_D G(\underline{r}, \underline{r}')W(\underline{r}')d\underline{r}' \triangleq A_\Gamma[W(\underline{r}')] \text{ con } \underline{r} \in \Gamma \text{ (A. 2)}$$

where:

- $u_s(\underline{r})$ is the scattered electric field outside the ROI;
- $u_{tot}(\underline{r})$is the total electric field in the whole space sum of the incident field u_{inc} i.e. the field in the absence of the scatterer, and u_s is the scattered field;
- $G(\underline{r}, \underline{r}')$ is the electric current to electric field Green's function according to [58]
- A_D e A_Γ are two integral operator which allow to obtain the scattered electric field respectively in D and in Γ;
- $k_b = \omega\sqrt{(\varepsilon_{eqb}\,\mu_0)}$ is the background wave number.

Note that similar equations can be derived for the magnetic case.

Furthermore, $W(\underline{r}') = \chi(r)u_{tot}(\underline{r}')$ is the contrast source in which $\chi(r)$ is the so-called contrast function, which is strictly related to the scatterer properties, at the angular frequency $\omega = 2\pi f$, and is defined as:

$$\chi(\underline{r}) = \frac{\varepsilon_{eqs}(\underline{r})}{\varepsilon_{eqb}} - 1 \qquad (A.3)$$

where the subscript "eq" indicates that we refer to equivalent complex permittivity (i.e. including conductivity losses). Expliciting these losses the equations will be the following form:

$$\chi(\underline{r}) = \frac{\varepsilon(\underline{r}) - \frac{j\sigma_s(\underline{r})}{\omega\varepsilon_0}}{\varepsilon_b - \frac{j\sigma_b}{\omega\varepsilon_0}} \qquad (A.4)$$

The two equations are named *state equation* and *data equation*.

The inverse problem, as it was formulated is ill-posed due to the properties of the radiation operator A_Γ ; while the non-linearity is an intrinsic problem in the formulation of the problem, in particular it is inherent in the *state equation*, due to the fact that both the contrast function and the induced currents/total field are unknown of the problem.

A.3 Ill-posedness and Non-linearity

The mathematical nature of the direct and inverse problems is profoundly different: the direct problem has certain good properties that correspond to the definition of a *well-posed* and *linear problem*, while the inverse scattering problem is usually *non-linear* and *ill-posed*. These two completely opposite natures imply an analysis with different degrees of difficulty.

Ill-posedness

A problem is said to be *well-posed* according to Hadamard [47] if:

- a solution exists;
- the solution is unique;
- the solution depends continuously on the data of the problem.

If even one of the above conditions is violated, the problem is said to be *ill-posed*. It makes no sense to look for a solution of an ill-posed problem (as it stands). In fact, if a solution does not exist, it makes no sense to look for it, and if the retrieved solution is not unique, it cannot be considered reliable.

Furthermore, in the direct problem, since sufficient information is provided to be able to a well-defined and stable procedure that leads to a single

solution of the problem, the crucial aspect lies in determining the solution in a computationally efficient way.

On the other hand, in the inverse problem, it resides in the identification of methods capable of providing a solution of the problem which is, as in the previous case, stable, even if approximate. The most demanding condition, in fact, is the stability. In this regard, a further concept closely linked is the *ill-conditioning*. A problem is said to be *ill-conditioned* when small variations on data can produce large variations in the solution of the problem. Because of the inherent instability, the solution of an ill-conditioned problem may not have a physical meaning in case of errors on data, that are simply unavoidable when a measurement process is in order.

It is worth to note that whenever the problem is ill-posed and/or ill-conditioned, one needs some regularization of the problem. Such a regularization occurs by funding a generalized solution to the problem that is usually defined as the optimum of some ad-hoc introduced cost functional.

In a wide variety of application domains, one of the most important tasks is to identify problem-solving strategies that make it possible to properly address the issue at hand.

The general approach for regularizing an ill-posed problem is to set an appropriate constraint on the solution. During the years authors have introduced several regularization techniques. The widely adopted are the techniques that aim to find the minimum energy solution [83] [84] those that aim at edges preserving and non-smooth solutions [85] and those that exploit the concept of sparsity in signals [86]

As far as the first category, a possible and widely adopted regularization techniques is the Tikhonov one [84] which introduces an additive term properly weighted to the functional to be minimized, which leads the procedure towards the minimum energy solution:

$$\phi(x) = \phi(x) + \alpha|x|^2 \qquad (A.5)$$

wherein α is the regularization parameters or Tikhonov parameter.

In case of iterative methods, such a regularization is performed at each iteration, and the most trivial task is the choice of the weights which depends on the strength of the regularization.

Most common, is also the adoption of the multiplicative regularization, in which the functional to be minimizing is regularized by means of a multiplicative factor, as follows:

$$\phi(x) = \phi(x)M(x) \qquad (A.6)$$

wherein $M(x)$ is calculated as the L2-norm total variation of the unknown contrast.

Another possible regularization strategy is the regularization by compressive sensing (CS) [86] . The starting point of CS-based techniques is to consider that many physical signals are intrinsically or extrinsically sparse and can be represented by few nonzero expansion coefficients. In this respect, these techniques aim for an approximation solution x of a linear system $y = Ax$ with the fewest nonzero terms. If the acquisition technique (i.e., input/output transformation matrix A) meets working conditions, a high-dimensional signal can be obtained from a small set of measurements using deterministic/Bayesian search strategies.

It is empirically shown that, according to the Compressive Sensing theory, the solution can be obtained by solving the following convex optimization problem:

$$\min\|x\|_{l1} \qquad subject\ to \qquad \|y - Ax\|_{l2} \qquad (A.7)$$

In fact, if the vector x is sufficiently sparse or has a certain number of zeros whose location is unknown, it is shown that for this particular situation, the minimization of the norm l_1 is more suitable for the solution of an indeterminate system of equations.

Due to the difficulty in tackling the ill-posedness and non-linearity of the inverse scattering problem different solution methods have been proposed in the literature. A common feature for any inversion approach is the requirement to be fast, to have a low computational burden and to provide reliable reconstructions with as minor as possible priori information on the physical or geometrical properties of the unknown scenario.

Non-linearity

As far as the non-linearity of the inverse scattering problem, it is related to the dependence of W or u_{tot} on the unknown contrast function χ [14] [46] A generalized solution of inverse scattering is usually solved by seeking the global minimum of a suitable functional which takes into account both state equation and data equation. As the initial problem is non-linear, the cost functional to be (globally) minimized is non-quadratic, so that it may have many local minima (Figure A.2) which are 'false solutions' of the problem [48]

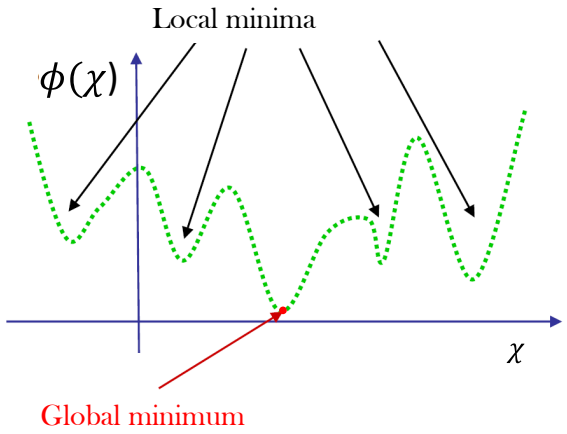

Figure A.2: Sketch of a non-quadratic cost functional

The more the problem differs from the linear one, the higher the possibility of incurring in a local minimum. A possible key to avoid the occurrence of false solutions is to have a sufficiently large ratio amongst the number of independent information and number of unknowns. Unfortunately, there are only a few degrees of freedom that can be exploited [48] , hence the number of independent data is limited.

In this respect, to quantify the Degree of Non-Linearity (DNL) it is reasonable to think in terms of the norm of the operator χA_D. In fact, if this norm is lower than 1, the inverse operator formally solving eq. (A.1) can be expanded into a Neumann series:

$$(1 - A_D\chi)^{-1} = [I + A_D\chi + (A_D\chi)^2 + \cdots + (A_D\chi)^n + ..] \quad (A.8)$$

By evaluating the norm of χA_D one can also understand what series terms must to be adopted in order to achieve a given approximation accuracy. Moreover, one can understand that the overall DNL, and hence the complexity and difficulty of the inverse scattering problem at hand, increases with the norm of the operator χA_D.

The solution methods proposed in literature tackling the non-linearity, can be grouped into three main classes:

- *non-linear optimization methods,* through which the solution is obtained iteratively without any approximation [43] [44] [45] and aims at retrieving both geometrical and electromagnetic properties of the targets;
- *qualitative methods*, which do not identify the electromagnetic characteristics of the scatterer, but limit themselves to identifying its "support", therefore its position, shape and size [24] [72] ;
- *approximated methods*, which solve the problem by adopting specific approximations in the mathematical model and are valid only under certain assumptions [47] .

The choice of a method rather than another one depends strictly on the problem one must dealt with. In particular, it depends on the final goal (i.e. to detect a target into a homogeneous background, to retrieve the electromagnetic properties of an object and so on) and also from the information at hand (position, dimension and so on).

Non-linear optimization methods

They aim at retrieving the contrast function χ by directly solving the non-linear equation A.1 (see Section A.2). Typically, such a task is pursued by means of optimization procedures, through the minimization of a cost functional. One possible solution is represented by global optimization approaches (i.e. contrast source inversion method[43] [44] [45]), which can reach the global minimum of the cost functional but such kind of approach is not suitable in case of a very

large number of unknows, as usually occurs in medical imaging. Another problem is related to the fact that the solution of these methods is closely linked to the choice of starting point for the procedure. Due to the non-linearity of the problem, the minimization procedure can be trapped in local minimum (which are the false solutions), and this would mean choosing a local solution that could be very far from the global one. This becomes more effective if the starting guess is located in a basin of attraction different from that in which the actual solution is found.

These types of methods also fall into the category of quantitative methods because they aim to reconstruct the morphological and electromagnetic properties of the scatterer objects.

Qualitative methods

Qualitative methods, unlike the methods previously described, allow to retrieve only some parameters, such as the shape and location of possible unknown object and so they are useful in those applications in which one is not interested in the electromagnetic characteristics of the target. All the qualitative approaches have the advantage to solve an auxiliary linear optimization procedure and for this reason, they are more easy to implement and more computationally efficient compare to the quantitative ones.

Furthermore, all 'qualitative' information gained by one of qualitative method can be exploited, in order to get a preliminary understanding of shape and/or of other characteristics. Such an understanding can be used to get a good starting point, or even to reduce the space of search for quantitative procedures. Examples of qualitative approaches are the Time reversal based methods[24], [72] and the Linear Sampling Methods[87].

Approximated methods

This category includes all methods in which some approximations are adopted with the aim of reducing the degree of non-linearity of the problem. Among the methods of linearization by approximation, the Born method [47] is certainly one of the best known. The Born approximation, in particular of the first order, is applicable to objects whose dimension is sufficiently small respect to the wavelength λ and whose electrical properties are very similar to

those of hosted medium. From an analytical point of view, this means approximating the total internal field with the incident field, denying the presence of the scatterer.

Objects with these characteristics are called "weak scatterers". The use of these kind of scatterers allows to turn the problem into a linear (but ill-posed) problem easier to solve. On the other hand, approximated methods can be applied only in some conditions and require strong a priori information of the investigated scenario.

Appendix B

This Appendix is aimed at giving some concepts and specially some basics about the artificial neural network.

B.1 Artificial neural networks: basics

Artificial neural networks are information-processing systems whose function is modelled like that of biological nervous systems. A neural network is composed of numerous basic processing units interconnected in various ways. Some of these units receive information from the environment, while others emit replies to the environment, and yet others communicate exclusively with other network units. The first group is classified as input units, the second as output units, and the third as hidden units [10]. Each of these units is designed to simulate a neuron or a group of neurons; hence, they are incorrectly classified as neurons within biological neural networks. In addition, each of these units conducts a relatively straightforward operation, consisting of activating itself if the overall quantity of signal it receives exceeds its activation threshold. If a unit becomes active, it produces a signal that travels over its associated units' communication channels [88] [89] Each connecting point then functions as a filter, changing the incoming signal into either an excitatory or an inhibitory signal. The connection points mimick the biological synapses from which they also derive their name. In fact, their primary function is to "weigh" the intensity of the transmitted signals, hence their designation as synaptic weights or, more generally, as lost synaptic weights.

The scheme of a simple neural network is depicted in Figure B.1. As can be seen from the Figure C.1, each node can receive signals from several other nodes, each of which is weighted by the appropriate synaptic connection.

McCulloch and Pitts were the first researchers to study such a kind of possibility, and the first who also proved that a group of these networked components is able of carrying out any general arithmetic and logical operation. When an external stimulus is applied to the input neurons of the neural network, the signals travel in parallel along the interconnections through the internal nodes to the output nodes, whose activation represents the response of the neural network. Additionally, each node only processes local

information, which means that it is only active in accordance with the data it gets through its input connections and is unaware of the operations carried out by other nodes to which it does not connected. The layout of the connections and the values of the artificial synapses (weights) substantially control the behaviour and reaction of the network, while each node is supplied with auxiliary memory boxes. For this, the short-term memory of the network is defined as the momentary activation state of the network nodes in response to an incoming stimulus. The long-term memory of the network is represented by the synapse. It should also be noted that a neural network learns to provide the right responses based on the input it receives by changing the weight values in accordance with diffenent learning rules. Usually the learning phase of the network is gradual and requires a huge number of examples.

Artificial neural networks are useful in many research fields and for several applications, including inverse problem [14] [19] The reason for their massive use can be found in the advantages that the use of these networks entails among them [88] [89] :

• **Robustness**, which refers to a neural network's resistance to noise and ability to provide us the right response even when noise is added to the input.

• **Flexibility**, because a neural network learns the unique qualities of an application domain via experience, it may be employed for a variety of tasks.

• **Generalization**, the ability of a neural network trained on a small set of examples to respond appropriately to inputs that have never been seen before.

B.2 Tunable network hyperparameters

There are several parameters that come into play in training a neural network, among these the most important are[88] [89] :

Objective function

In general, an artificial intelligence system transforms the input data into output data through an **objective function** F, regulated by a set of parameters θ:

$$y = F(x, \theta) \qquad (B.1)$$

Learning consists in finding the optimal parameters θ' for which, by applying the objective function to a set of input values, the output data will be equal to those expected, net of a certain error ε

$$y + \varepsilon = F(x, \theta') \qquad (B.2)$$

Epoch, batch size e iterations

During the training phase, the patterns contained in the training dataset are provided, so that the model can adapt its parameters to find the optimal objective function. However, a single step is not enough to obtain an optimal result, but it is necessary to carry out several processing cycles of the dataset and adaptation of the parameters.

Furthermore, due to the limits of memory and the computing power available for these processes, it is usually not possible to process the entire training set "one shot". For this reason, there are some parameters that come into play in defining how the processing of the dataset must take place during the training phase. When the entire training set has been subjected to the model, then we have an **epoch**. The training phase usually ends after several epochs (tens of thousands can be needed). But not always, by increasing the epoch, the model improves.

The training dataset may be too large to be processed all at once (think of a training set consisting of tens of thousands of images). Then you can divide the training set into uniform subgroups, called **batches**.

The number of samples contained in each batch is called the **batch size**. Hence the iteration definition which corresponds to the number of batches needed to complete an epoch.

If the batch size is too large, there could be a problem of running out of memory or a more pronounced tendency to overfitting.

Loss function

The loss function (or cost function) is a function that evaluates the performance of a model. It represents a loss and therefore the goal of good learning is the minimization of the loss function: the lower the loss, the better the model (unless the model is overfitted, as we will see).

The loss is calculated on the training and validation pattern datasets and therefore is limited to assessing how well the training is done with these.
It is a numerical value that represents a sum of the errors made for each example of the training or validation set.

Learning rate

The learning rate is a hyperparameter that determines how much to change the model each time the model weights are updated in response to the predicted error. It can be difficult to choose the learning rate since a number that is too small could lead to a long training process, but a value that is too big could lead to learning a suboptimal set of weights too fast or to an unstable training process.
Among all the network parameters to be tuned, the learning rate is the most crucial one.

B.3 Convolutional neural network

A convolutional neural network (CNN or ConvNet) is a network architecture for deep lerning (machine learning technique) [88] [89] that learns directly from data, eliminating the need to manually extract features. CNNs have an optimal architecture to identify and learn the most representative features in given images and indeed, they are used in various application areas such as [49] :

• **Biomedical Imaging**, CNNs are in fact able to analyse medical tests to visually detect the presence of tumor cells in the images.

• **Audio processing**, CNNs are in fact able to detect keywords and this can be used in any device with a microphone in order to detect when a certain word is spoken.

• **Detection of stop signs**, autonomous driving uses CNNs to accurately detect the presence of a signal or other objects and make decisions based on the output.

A CNN is a feed-forward neural network (see Figure C.1), inspired by the organization of the visual cortex. A CNN is a network made up of several layers and each of these is specialized in carrying out a certain task. The operation of a convolutional neural network in general is similar to that of other feed-forward networks in which there is an input layer, one or several hidden layers, which perform the calculations using the activation function (f.i. Rectified Linear Unit, RELU) and finally an output layer that performs the actual task. Like other standard artificial neural networks, CNNs are typically trained with back propagation and gradient descent. The first algorithm refers to the practice of iteratively calculating the gradient of the objective function with respect to the network's weights by the chain rule. This gradient is calculated for one layer at a time, starting from the last layer and going back to

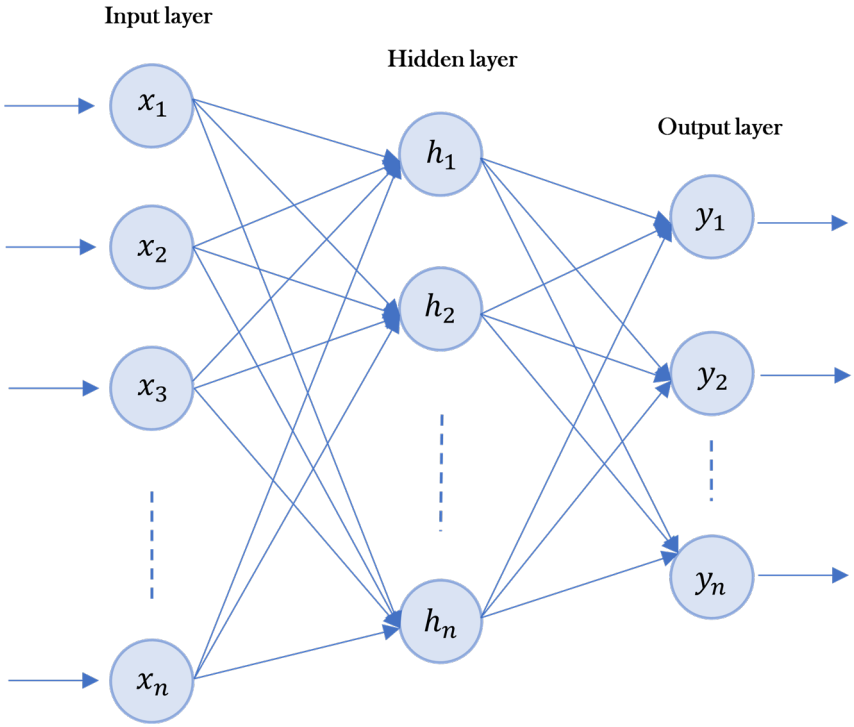

Figure B.1: General scheme of an artificial neural network, reporting the interconnections among the nodes belonging to the different layers.

the first. Gradient descent is an optimization algorithm that allows identifying the weights that minimize the objective function.

The novelty introduced by CNN with respect to other neural networks is the presence of convolutional levels. These levels play a key role in the CNN architecture, as they extract, through the use of special filters, the features of the images to be analysed. Then, a CNN, unlike normal feed-forward networks which work more on general image information, works based on salient features of the image itself. In general, depending on the employed filter, it is possible to detect various details on the source images, including the outlines of the figures, vertical or horizontal lines, and so forth. As a result, CNNs are able to process more accurate data than traditional feed-forward networks, which allows them to function more reliably. .Therefore, a CNN network can be seen as blocks chain, the order of which is represented as follows:

Input->Conv->ReLU->Pool->Conv->ReLU->Pool->ReLU->Conv->ReLU->Pool->FullyConnected.

The **Input layer** consists of a sequence of neurons able to receive information based on the data to be treated. This is followed by the **Convolutional Level**, which is the main level of the network. Convolution subjects the input images to a series of convolutional filters, each of which activates certain features from the images. The filters, that can be used, are more than one. The greater the number of filters applied the greater the complexity of the features that can be identified. Practically in the convolutional layer a filter (mask) is made to slide along the whole dimension of the inputs (slide over). Then the so-called Hadamard Product is executed where essentially the scalar product between the inputs and the various filters is executed. Finally, the subsampling follows, where the features of the previous layer are taken and combined in such a way to have more complex features. **Padding** is also important, as using a large number of convolutional layers risks losing the resizing of the image. To avoid this, it is needed to outline the image with one or more layers of zeros to preserve its size. Within the convolutional level, immediately after the subsampling phase, there is the **Activation layer**. In this layer, through an activation function (f.i. a linear activation function, ReLU,), the goal is to cancel the non-useful values. The ReLU function is the most

common and it allows to train more quickly and effectively by mapping the negative values to zero and keeping the positive values. This layer is crucial because only activated features are passed to the next layer. Finally, at the end of the Convolutional level, the image will be scanned piece by piece, obtaining a smaller matrix of values that represents "the characterized image". The Convolutional level is then followed by a **Pooling layer**, generally Max Pooling. This level allows to identify if the study feature is present in the previous level and makes the image coarser. In other words, the max pooling layer is a method for reducing the size of an image, dividing it into blocks and keeping only the one with the highest value. Doing so reduces the problem of overfitting and only the areas with greater activation are maintained. Another widely used layer is the **Batch normalization layer.**

These regularization layers normalize the activation maps by subtracting the mean and dividing them by the standard deviation for each of the training batches. In addition to reducing overfitting, the use of batch normalization also speeds up the training and makes the network less dependent on the initial parameter initialization.

Appendix C

This Appendix is aimed at giving more mathematical details for the auxiliary model in Section 4.4. In this respect, one can analytically determine a value of ϕ_1 such that the auxiliary fields have the same amplitude at the external points and at midway, as it will briefly discussed in the following.

Consider two control points $\underline{r}_{t_0}$ and $\underline{r}_{t_1}$ located at distance d in a lossless and homogeneous ROI, characterized by a wave number k_m. Then, the auxiliary model (4.6) can be simplified as follows:

$$F_{aux}(\underline{r}) = J_0(k_m|\underline{r} - \underline{r}_{t_0}|) + J_0(k_m|\underline{r} - \underline{r}_{t_1}|)e^{j\phi_1} \quad \text{(C.1)}$$

In such a simple case, one can analytically determine the values of ϕ_1 such that the field amplitudes are the same at $\underline{r}_{t_0}$, $\underline{r}_{t_1}$ and at midway. Indeed, by evaluating the amplitudes of $F_{aux}(\underline{r})$ at these points, that are:

$$|F_{aux}(\underline{r}_{t_0})| = |1 + J_0(k_m d)e^{j\phi_1}| \quad \text{(C.2.a)}$$

$$|F_{aux}(\underline{r}_{t_1})| = |J_0(k_m d) + e^{j\phi_1}| \quad \text{(C.2.b)}$$

$$\left|F_{aux}\left(\frac{\underline{r}_{t_1}+\underline{r}_{t_2}}{2}\right)\right| = \left|J_0\left(\frac{k_m d}{2}\right) + J_0\left(\frac{k_m d}{2}\right)e^{j\phi_1}\right| \quad \text{(C.2.c)}$$

and by imposing the three right hand members to be equal to each other, one can derive for the case of a lossless medium the ϕ_1 values such to obtain a uniform field in the ROI, i.e.:

$$\phi_1 = \arccos\left\{\frac{1+[J_0(k_m d)]^2 - 2\left[J_0\left(\frac{k_m d}{2}\right)\right]^2}{2\left[J_0\left(\frac{k_m d}{2}\right)\right]^2 - 2J_0(k_m d)}\right\} \quad \text{(C.3)}$$

References

[1] Weissleder, R., & Nahrendorf, M. (2015). Advancing biomedical imaging. Proceedings of the National Academy of Sciences, 112(47), 14424-

[2] Barrie Smith N Webb A. *Introduction to Medical Imaging : Physics Engineering and Clinical Applications*. Cambridge: Cambridge University Press; 2010.

[3] Gulani, V., & Seiberlich, N. (2020). Quantitative MRI: Rationale and Challenges.

[4] Leijsen R., Brink W., van den Berg C., Webb A., Remis R. Electrical Properties Tomography: A Methodological Review. Diagnostics (Basel). 2021;11(2):176. Published 2021 Jan 26. doi:10.3390/diagnostics11020176;

[5] Zhang X., Liu J. and He B., "Magnetic-Resonance-Based Electrical Properties Tomography: A Review," in IEEE Reviews in Biomedical Engineering, vol. 7, pp. 87-96, 2014, doi: 10.1109/RBME.2013.2297206.

[6] Attardo, E. A., Isernia, T., & Vecchi, G. (2011). Field synthesis in inhomogeneous media: Joint control of polarization, uniformity and SAR in MRI B 1-field. Progress In Electromagnetics Research, 118, 355-377.

[7] Padormo, F., Beqiri, A., Hajnal, J. V., & Malik, S. J. (2016). Parallel transmission for ultrahigh-field imaging. NMR in Biomedicine, 29(9), 1145-1161.

[8] Balidemaj, E., van den Berg, C. A., van Lier, A. L., Nederveen, A. J., Stalpers, L. J., Crezee, H., & Remis, R. F. (2017). B1-based SAR reconstruction using contrast source inversion–electric properties tomography (CSI-EPT). Medical & Biological Engineering & Computing, 55(2), 225-233.

[9] Persico, R. (2014). *Introduction to ground penetrating radar: inverse scattering and data processing*. John Wiley & Sons.

[10] Nikolova, N. K. (2011). Microwave imaging for breast cancer. *IEEE microwave magazine*, *12*(7), 78-94.

[11] Kim S.Y., Shin J., Kim D.H., Kim E.K., Moon H.J., Yoon J.H., You J.K., Kim M.J. "Correlation between electrical conductivity and apparent diffusion coefficient in breast cancer: effect of necrosis on magnetic resonance imaging". Eur Radiol., vol. 28, pp:3204-3214, 2018.

[12] Brace, C. L. (2009). Radiofrequency and microwave ablation of the liver, lung, kidney, and bone: what are the differences?. Current problems in diagnostic radiology, 38(3), 135-143.

[13] Bellizzi, G. G., Drizdal, T., van Rhoon, G. C., Crocco, L., Isernia, T., & Paulides, M. M. (2018). The potential of constrained SAR focusing for hyperthermia treatment planning: Analysis for the head & neck region. Physics in Medicine & Biology, 64(1), 015013.

[14] Chen, X. (2018). Computational methods for electromagnetic inverse scattering. John Wiley & Sons.

[15] Zumbo, S., Bevacqua, M. T., Battaglia, G. M., & Isernia, T. (2022, March). Application of Field Intensity Shaping Paradigm in a Biological Scenario for MRI Shimming. In 2022 16th European Conference on Antennas and Propagation (EuCAP) (pp. 1-3). IEEE.

[16] Dessouky, M. I., Sharshar, H., & Albagory, Y. (2007). Design of high altitude platforms cellular communications. Progress In Electromagnetics Research, 67, 251-261.

[17] Morabito, Andrea & Antonia, laganà & Di Donato, Loreto. (2016). Satellite multibeam coverage of earth: innovative solutions and optimal synthesis of aperture fields. Progress In Electromagnetics Research. 156. 135-144. 10.2528/PIER16061505.

[18] Mosalanejad, Mohammad & Brebels, Steven & Soens, Charlotte & Ocket, Ilja & Vandenbosch, Guy. (2017). Millimeter wave cavity backed microstrip antenna array for 79GHz radar applications. Progress In Electromagnetics Research. 158. 89-98. 10.2528/PIER17010407.

[19] Chen, X., Wei, Z., Li, M., & Rocca, P. (2020). A review of deep learning approaches for inverse scattering problems (invited review). Progress In Electromagnetics Research, 167, 67-81

[20] Zumbo, S., Mandija, S., Meliadó, E. F., Van den Berg, C. A. Isernia, T., and Bevacqua M. T., "Application of Supervised Descent Method to MRI Electrical Properties Tomography," 2022 16th European Conference on Antennas and Propagation (EuCAP), 2022, pp. 1-5, doi: 10.23919/EuCAP53622.2022.9768930.

[21] Zumbo, S., Mandija, S., Meliadò, E. F., Stijnman, P., Meerbothe, T., van den Berg, C. A., ... & Bevacqua, M. T. (2022, May). Advances in MRI based Electrical Properties Tomography: a Comparison between Physics-supported Learning Approaches. In 2022 Microwave Mediterranean Symposium (MMS) (pp. 1-5). IEEE.

[22] Woodward, P. and J. Lawson, "The theoretical precision with which an arbitrary radiation-pattern may be obtained from a source of finite size," Journal of the Institution of Electrical Engineers — Part III: Radio and Communication Engineering, vol. 95, no. 37, pp. 363–370, 1948.

[23] Bellizzi, Gennaro & Iero, Domenica & Crocco, Lorenzo & Isernia, T.. (2018). 3-D Field Intensity Shaping: The Scalar Case. IEEE Antennas and Wireless Propagation Letters. PP. 1-1. 10.1109/LAWP.2017.2746801.

[24] Bellizzi, G. G., Bevacqua, M. T., Crocco, L., & Isernia, T. (2018). 3-D field intensity shaping via optimized multi-target time reversal. IEEE Transactions on Antennas and Propagation, 66(8), 4380-4385.

[25] Zumbo, S., Isernia, T., & Bevacqua, M. T. (2022). A Simple Auxiliary Model for Field Amplitude Shaping in Complex Environments, and Application to MRI Shimming. IEEE Open Journal of Antennas and Propagation, 3, 917-931.

[26] OECD (2022), Magnetic resonance imaging (MRI) units (indicator). doi: 10.1787/1a72e7d1-en (Accessed on 02 November 2022).

[27] Bloch, F., 1946. Nuclear induction. J Physical review 70, 460.

[28] Purcell, E.M., Torrey, H.C., Pound, R.V., 1946. Resonance absorption by nuclear magnetic moments in a solid. J Physical review 69, 37.

[29] Wansapura JP, Holland SK, Dunn RS, Ball WS Jr. NMR relaxation times in the human brain at 3.0 tesla. *J Magn Reson Imaging*. 1999;9(4):531-538.

[30] ICNIRP. Guidelines for limiting exposure to electromagnetic fields (100 kHz to 300 GHz). Health Phys 118(00):000–000; 2020. Pre-print. DOI: 10.1097/HP.0000000000001210.

[31] Hartwig, V., Giovannetti, G., Vanello, N., Lombardi, M., Landini, L., & Simi, S. (2009). Biological effects and safety in magnetic resonance imaging: a review. *International journal of environmental research and public health*, *6*(6), 1778–1798. https://doi.org/10.3390/ijerph6061778.

[32] Van den Bergen, B., Van den Berg, C. A., Bartels, L. W., & Lagendijk, J. J. (2007). 7 T body MRI: B_1 shimming with simultaneous SAR reduction. *Physics in medicine and biology*, *52*(17), 5429–5441. https://doi.org/10.1088/0031-9155/52/17/022.

[33] Tha KK, Katscher U, Yamaguchi S, Stehning C, Terasaka S, Fujima N, Kudo K, Kazumata K, Yamamoto T, Cauteren M, Shirato H. "Noninvasive electrical conductivity measurement by MRI: a test of its validity and the electrical conductivity characteristics of glioma". Eur Radiol. 2018; 28:348-355.

[34] Mandija, S., Petrov, P. I., Vink, J. J., Neggers, S. F., & van den Berg, C. A. (2021). Brain tissue conductivity measurements with MR-electrical properties tomography: an in vivo study. Brain topography, 34(1), 56-63.

[35] Brown, B. H. (2003). Electrical impedance tomography (EIT): a review. *Journal of medical engineering & technology*, *27*(3), 97-108.

[36] Ma, L., & Soleimani, M. (2017). Magnetic induction tomography methods and applications: A review. *Measurement Science and Technology*, *28*(7), 072001.

[37] Oh, S. H., Lee, B. I., Woo, E. J., Lee, S. Y., Cho, M. H., Kwon, O., & Seo, J. K. (2003). Conductivity and current density image reconstruction using harmonic Bz algorithm in magnetic resonance electrical impedance tomography. *Physics in Medicine & Biology*, *48*(19), 3101.

[38] Wen, H., Shah, J., & Balaban, R. S. (1998). Hall effect imaging. IEEE transactions on biomedical engineering, 45(1), 119-124.

[39] Ammari, H., Qiu, L., Santosa, F., & Zhang, W. (2017). Determining anisotropic conductivity using diffusion tensor imaging data in magneto-acoustic tomography with magnetic induction. Inverse Problems, 33(12), 125006.

[40] Haacke, E. M., Petropoulos, L. S., Nilges, E. W., & Wu, D. H. (1991). Extraction of conductivity and permittivity using magnetic resonance imaging. Physics in Medicine & Biology, 36(6), 723.

[41] H. Wen, "Non-invasive quantitative mapping of conductivity and dielectric distributions using RF wave propagation effects in high-field MRI," in Proc. SPIE, vol. 5030, San Diego, CA, USA, 2003, pp. 471–477.

[42] Van Lier, A. L., Brunner, D. O., Pruessmann, K. P., Klomp, D. W., Luijten, P. R., Lagendijk, J. J., & van den Berg, C. A. (2012). B1 phase mapping at 7 T and its application for in vivo electrical conductivity mapping. Magnetic Resonance in Medicine, 67(2), 552-561.

[43] Leijsen, R.L.; Brink, W.M.; Van Den Berg, C.A.; Webb, A.G.; Remis, R.F. 3-D Contrast Source Inversion-Electrical Properties Tomography. IEEE Trans. Med. Imaging 2018, 37, 2080–2089.

[44] Leijsen, R.; Fuchs, P.; Brink,W.;Webb, A.; Remis, R. Developments in Electrical-Property Tomography Based on the Contrast-Source Inversion Method. J. Imaging 2019, 5, 25

[45] Van den Berg, P., & Abubakar, A. (2001). Contrast source inversion method: State of art. *Progress in Electromagnetics Research*, *34*, 189-218.

[46] Colton D. and Kress R. 1998 Inverse Acoustic and Electromagnetic Scattering Theory, Springer-Verlag, Berlin, Germany.

[47] Bertero, M., Boccacci, P., & De Mol, C. (2021). Introduction to inverse problems in imaging. CRC press.

[48] Isernia, T., Pascazio, V., & Pierri, R. (2001). On the local minima in a tomographic imaging technique. IEEE Transactions on Geoscience and Remote Sensing, 39(7), 1596-1607.

[49] McCann, M. T., Jin, K. H., & Unser, M. (2017). Convolutional neural networks for inverse problems in imaging: A review. *IEEE Signal Processing Magazine*, *34*(6), 85-95.

[50] Mandija, S.; Meliadò, E.F.; Huttinga, N.R.; Luijten, P.R.; van den Berg, C.A. Opening a New Window on MR-Based Electrical Properties Tomography with Deep Learning. Sci. Rep. 2019, 9, 1–9.

[51] Leijsen, R., van den Berg, C., Webb, A., Remis, R., & Mandija, S. (2019). Combining deep learning and 3D contrast source inversion in MR-based electrical properties tomography. NMR in Biomedicine, e4211.

[52] Darwish A, Ricci M, Zidane F, Vasquez JAT, Casu MR, Lanteri J, Migliaccio C, Vipiana F. Physical Contamination Detection in Food Industry Using Microwave and Machine Learning. *Electronics*. 2022; 11(19):3115. https://doi.org/10.3390/electronics11193115

[53] Guo, R., Jia, Z., Song, X., Li, M., Yang, F., Xu, S., & Abubakar, A. "Pixel-and model-based microwave inversion with supervised descent method for dielectric targets". IEEE Transactions on Antennas and Propagation, vol. 68, no. 12, pp. 8114-812, 2020.

[54] Franceschetti, Giorgio. Campi Elettromagnetici. 2ª ed. Torino: Bollati Boringhieri, 1988. Print. Programma Di Matematica, Fisica, Elettronica.

[55] Fuchs, P. S., Mandija, S., Stijnman, P. R., Brink, W. M., van den Berg, C. A., & Remis, R. F. (2018). First-order induced current density imaging and electrical properties tomography in MRI. *IEEE Transactions on Computational Imaging*, *4*(4), 624-631.

[56] Yarnykh, V. L. (2007). Actual flip-angle imaging in the pulsed steady state: a method for rapid three-dimensional mapping of the transmitted radiofrequency field. Magnetic Resonance in Medicine: An Official Journal of the International Society for Magnetic Resonance in Medicine, 57(1), 192-200.

[57] http://resolver.tudelft.nl/uuid:ffdf0bb5-5b27-43be-8d8956dd929fbd7c

[58] Balidemaj, E., van den Berg, C. A. T., Trinks, J., van Lier, A. L. H. M. W., Nederveen, A. J., Stalpers, L. J. A., Crezee, H., & Remis, R. F. (2015). CSI-EPT: A Contrast Source Inversion Approach for Improved MRI-Based Electric Properties Tomography. IEEE Transactions on Medical Imaging, 34(9), 1788–1796. https://doi.org/10.1109/tmi.2015.2404944

[59] Hauptmann, A., Lucka, F., Betcke, M., Huynh, N., Adler, J., Cox, B., ... & Arridge, S. (2018). Model-based learning for accelerated, limited-view 3-D photoacoustic tomography. *IEEE transactions on medical imaging*, *37*(6), 1382-1393.

[60] Wei, Z. and X. Chen, "Deep-learning schemes for full-wave nonlinear inverse scattering problems,*IEEE Transactions on Geoscience and Remote Sensing*, Vol. 57, No. 4, 1849–1860, 2019.

[61] Ongie, G., Jalal, A., Metzler, C. A., Baraniuk, R. G., Dimakis, A. G., & Willett, R. (2020). Deep learning techniques for inverse problems in imaging. *IEEE Journal on Selected Areas in Information Theory*, *1*(1), 39-56.

[62] Lønning, K., Putzky, P., Sonke, J. J., Reneman, L., Caan, M. W., & Welling, M. (2019). Recurrent inference machines for reconstructing heterogeneous MRI data. *Medical image analysis*, *53*, 64-78.

[63] Zubal, I. G., Harrell, C. R., Smith, E. O., Rattner, Z., Gindi, G., & Hoffer, P. B. (1994). Computerized three-dimensional segmented human anatomy. *Medical physics*, *21*(2), 299-302.

[64] Hasgall P. A., Gennaro F. D., Baumgartner C., Neufeld E., Gosselin M., Payne D., Klingenbock A., and Kuster N., IT'IS Database for thermal and electromagnetic parameters of biological tissues, Version 3.0, 2015.

[65] Angeletti, P., & Cubillos, J. L. (2021). Traffic balancing multibeam antennas for communication satellites. IEEE Transactions on Antennas and Propagation, 69(12), 8291-8303.

[66] Mosalanejad, M., S. Brebels, C. Soens, I. Ocket, and G. A. E. Vandenbosch, "Millimeter wave cavity backed microstrip antenna array for 79 GHz radar applications," Progress In Electromagnetics Research, Vol. 158, 89–98, 2017.

[67] Ayestarán, R. G., León, G., Pino, M. R., & Nepa, P. (2019). Wireless power transfer through simultaneous near-field focusing and far-field synthesis. IEEE Transactions on Antennas and Propagation, 67(8), 5623-5633.

[68] Nepa, P.; Buffi, "A. Near-Field-Focused Microwave Antennas: Near-field shaping and implementation", *IEEE Antennas Propag. Mag.* 59, 42–53, 2017.

[69] Costanzo, S., & Di Massa, G. (2017, March). Near-field focusing technique for enhanced through-the-wall radar. In 2017 11th European Conference on Antennas and Propagation (EUCAP) (pp. 1716-1717). IEEE.

[70] Paulides, M. M., Verduijn, G. M., & Van Holthe, N. (2016). Status quo and directions in deep head and neck hyperthermia. Radiation Oncology, 11(1), 1-14.

[71] Mao, W., M. B. Simth, and C. M. Collins, "Exploring the limits of RF shimming for high field MRI of the human head," *Magn. Res. in Med.*, vol. 56, 918-922, 2006.

[72] Thomas, J. L., Wu, F., & Fink, M. (1996). Time reversal focusing applied to lithotripsy. Ultrasonic imaging, 18(2), 106-121.

[73] Bernstein M.A., Huston J. 3rd, Ward H.A. (2006). Imaging artifacts at 3.0T. *J Magn Reson Imaging*; 24(4):735-46. doi: 10.1002/jmri.20698. PMID: 16958057])

[74] Haemer, G., Vaidya, M., Collins, C., Sodickson, D., Wiggins, G., & Lattanzi, R. (2018). Approaching ultimate intrinsic specific absorption rate in radiofrequency shimming using high-permittivity materials at 7 Tesla. *Magnetic Resonance in Medicine*, 80.

[75] Brink, W. M., Gulani, V., & Webb, A. G. (2015). Clinical applications of dual-channel transmit MRI: A review. *Journal of Magnetic Resonance Imaging*, 42(4), 855-869

[76] Georgakis, I. P., Polimeridis, A. G., & Lattanzi, R. (2020). A formalism to investigate the optimal transmit efficiency in radiofrequency shimming. *NMR in Biomedicine*, 33(11), e4383.

[77] Van den Bergen B, Van den Berg CA, Bartels LW, Lagendijk JJ. 7 T body MRI: B1 shimming with simultaneous SAR reduction. *Phys Med Biol.* 2007 Sep 7;52(17):5429-41. doi: 10.1088/0031-9155/52/17/022. Epub 2007 Aug 21. PMID: 17762096.

[78] Van Gemert, J. H. F., Brink, W. M., Webb, A. G., & Remis, R. F. (2017, September). Designing high-permittivity pads for dielectric shimming in MRI using model order reduction and Gauss-Newton optimization. In *2017 International Conference on Electromagnetics in Advanced Applications (ICEAA)* (pp. 417-420). IEEE

[79] Brink, W. M., Remis, R. F., Webb, A. G. "A theoretical approach based on electromagnetic scattering for analysing dielectric shimming in high-field MRI", Magnetic resonance in medicine, vol. 75, n. 5, pp. 2185-2194, 2016.

[80] Schmidt, R., Webb, A.G. Improvements in RF Shimming in High Field MRI Using High Permittivity Materials With Low Order Pre-Fractal Geometries. *IEEE Transactions on Medical Imaging, 35*, 1837-1844, 2016.

[81] Battaglia, G. M., Morabito, A. F., Sorbello, G., & Isernia, T. (2020). Mask-constrained power synthesis of large and arbitrary arraysas a few-samples global optimization. Progress In Electromagnetics Research C, 98, 69-81.

[82] Bellizzi, G. G., Drizdal, T., van Rhoon, G. C., Crocco, L., Isernia, T., & Paulides, M. M. (2018). Advances in multi-target FOCO for hyperthermia treatment planning: a robustness assessment.

[83] Mojabi, P., & LoVetri, J. (2009). Overview and classification of some regularization techniques for the Gauss-Newton inversion method applied to inverse scattering problems. IEEE Transactions on Antennas and Propagation, 57(9), 2658-2665.

[84] Tikhonov, A. N. (1963). On the solution of ill-posed problems and the method of regularization. In Doklady akademii nauk (Vol. 151, No. 3, pp. 501-504). Russian Academy of Sciences.

[85] Abubakar, A., Van den Berg, P. M., & Mallorqui, J. J. (2002). Imaging of biomedical data using a multiplicative regularized contrast source

inversion method. IEEE Transactions on Microwave Theory and Techniques, 50(7), 1761-1771.

[86] Massa, A., Rocca, P., & Oliveri, G. (2015). Compressive sensing in electromagnetics-a review. IEEE Antennas and Propagation Magazine, 57(1), 224-238.

[87] Colton, David & Haddar, Houssem & Piana, Michele. (2003). The linear sampling method in inverse electromagnetic scattering theory. Inverse Problems. 19. S105. 10.1088/0266-5611/19/6/057.

[88] Floreano, D., & Mattiussi, C. (2002). *Manuale sulle reti neurali* (No. BOOK). Il mulino.

[89] Cascini, G.L., Donato, V., Tamburrini, O. (2010). Introduzione alle reti neurali. In: Elementi di informatica in diagnostica per immagini. Springer, Milano. https://doi.org/10.1007/978-88-470-1667-5_18

Publications List

[1] M. T. Bevacqua, T. Isernia, F. G. Praticò, S. Zumbo. "A method for bottom-up cracks healing via selective and deep microwave heating", Automation in construction, Volume 121, January 2021, 103426.

[2] Martina T. Bevacqua, Tommaso Isernia, Filippo G. Praticò, Sabrina Zumbo, National Patent for industrial invention, "Ringiovanimento di strutture e infrastrutture tramite riscaldamento selettivo a microonde", http://hdl.handle.net/20.500.12318/46905.

[3] S. Zumbo, T. Isernia and M. T. Bevacqua, "A Simple Auxiliary Model for Field Amplitude Shaping in Complex Environments, and Application to MRI Shimming," in IEEE Open Journal of Antennas and Propagation, vol. 3, pp. 917-931, 2022, doi: 10.1109/OJAP.2022.3195667.

[4] F.G. Praticò, S. Zumbo, M.T. Bevacqua, T. Isernia, Microwave deep healing of road pavements: preliminary numerical results, Eleventh International Conference on the Bearing Capacity of Roads,Railways and Air fields,Volume3–ISBN978-1-032-12052-2O, DOI:10.1201/9781003222910-20.

[5] S. Zumbo, M. T. Bevacqua and T. Isernia, "MRI Shimming via Field Intensity Shaping," 2021 XXXIVth General Assembly and Scientific Symposium of the International Union of Radio Science (URSI GASS), 2021, pp. 1-5, doi: 10.23919/URSIGASS51995.2021.9560209.

[6] S. Zumbo, M. T. Bevacqua, and T. Isernia. "Field intensity shaping paradigm for shimming and SAR control in an MRI system", 49° National Congress GIDRM on Magnetic Resonance.

[7] S. Zumbo, M. T. Bevacqua, G. M. Battaglia and T. Isernia, "Application of Field Intensity Shaping Paradigm in a Biological Scenario for MRI Shimming," 2022 16th European Conference on Antennas and Propagation (EuCAP), 2022, pp. 1-3, doi: 10.23919/EuCAP53622.2022.9769026.

[8] S. Zumbo, S. Mandija, F. Meliadó, C. A. T. van den Berg, T. Isernia and M. T. Bevacqua, "Application of Supervised Descent Method to MRI

Electrical Properties Tomography," 2022 16th European Conference on Antennas and Propagation (EuCAP), 2022, pp. 1-5, doi: 10.23919/EuCAP53622.2022.9768930.

[9] M. T. Bevacqua, S. Zumbo and T. Isernia, "Some Improvements to Field Intensity Shaping for Biomedical Applications: Preliminary results," 2022 3rd URSI Atlantic and Asia Pacific Radio Science Meeting (AT-AP-RASC), 2022, pp. 1-4, doi: 10.23919/AT-AP-RASC54737.2022.9814396.

[10] S. Zumbo et al., "Advances in MRI based Electrical Properties Tomography: a Comparison between Physics-supported Learning Approaches," 2022 Microwave Mediterranean Symposium (MMS), 2022, pp. 1-5, doi: 10.1109/MMS55062.2022.9825562.

[11] S. Zumbo, M. T. Bevacqua, F. Meliadò, P. Stijnman, T. Meerbothe, CAT Van den Berg, Tommaso Isernia, S. Mandija. "Iterative MR-Electrical Properties Tomography using physics-based deep learning", 2022, ISMRM London.

[12] S. Zumbo, M. T. Bevacqua, T. Isernia, "Some Advances in Magnetic Resonance Imaging: Radiofrequency Shimming and Electrical Properties Tomography", 2022, ICEMB Cagliari.

[13] S. Zumbo, S. Mandija, F. Meliadò, P. Stijnman, T. Meerbothe, CAT Van den Berg, Tommaso Isernia, M. T. Bevacqua, "A new physics-based learning approach to solve inverse scattering problems for MRI-EPT", 2022, QMR Lucca.

[14] S. Zumbo, S. Mandija, M.T. Bevacqua, "MRI based Electrical Properties Tomography via an iterative physics-assisted learning method", 2022 RiNEM Catania.

[15] S. Zumbo, T. Isernia , M.T. Bevacqua, "A simple auxiliary model for field amplitude shaping", 2022 RiNEM Catania;